Synthesis, Assembly, and Integration of Semiconductor Nanowires

Elena P. Pandres

A dissertation

submitted in partial fulfillment of the

requirements for the degree of

Doctor of Philosophy

University of Washington

2020

Reading Committee:

Vincent C. Holmberg, Chair

Lilo D. Pozzo

Daniel T. Schwartz

Peter J. Pauzauskie

Program Authorized to Offer Degree:

Chemical Engineering

University of Washington

Abstract

Synthesis, Assembly, and Integration of Semiconductor Nanowires

Elena P. Pandres

Chair of the Supervisory Committee:

Vincent C. Holmberg

Department of Chemical Engineering

Semiconductor nanowires are a class of highly anisotropic crystalline materials with nanoscale diameters and lengths that range from micrometers to millimeters. The electronic, optical, and mechanical properties of semiconductor nanowires can be considerably different than their bulk counterparts, making them attractive for a range of applications including sensors, energy storage, and quantum information systems. Solution-based synthesis is a promising strategy to produce semiconductor nanowires in a scalable, cost-effective matter. However, many solution-based methods are limited in their ability to produce nanowires with increasingly complex compositions—including doped, alloyed, and heterostructured architectures—as well as to rapidly screen synthetic parameters for combinatorial discovery and optimization. In addition, chemistries and growth dynamics can be difficult to track with nanowire syntheses that require high temperature and extreme pressure equipment. Moreover, the widespread integration of

semiconductor nanowires into devices will also require new methods of assembly as well as careful consideration of surface chemistry. After an introduction to current methods of semiconductor nanowire synthesis, existing tactics for nanowire assembly, and strategies to improve the energy density of lithium ion batteries with group IV nanomaterials, this dissertation will cover three main topics related to (i) new synthetic methods for nanowire growth, (ii) a novel light-based nanowire assembly process, and (iii) the integration of nanowires into high-energy-density composite electrodes for lithium ion batteries.

Herein, we demonstrate a new continuous-flow, laser-driven, nanowire growth process that exploits the light absorption of colloidal metal nanocrystals to drive semiconductor nanowire growth in an optically accessible reactor on the benchtop, potentially opening the door for both rapid screening of synthetic parameters as well as *in situ* studies of nanowire growth dynamics. Investigations of solution-based nanowire growth using this system establish that laser-driven syntheses can achieve rapid, on-demand growth of semiconductor nanowires.

Importantly, the integration of nanowires into future device architectures will require a wide range of assembly strategies. While current solution-based nanowire assembly processes struggle to create deterministic heterojunctions, here, we demonstrate a novel example of nanowire assembly in a high-Prandtl-number organic solvent system, using an optical trap to orient, align, and "solder" metal-seeded semiconductor nanowires into periodic axial heterostructures.

Finally, we investigate the role of surface functionalization on the integration of group-IV nanowires into high-capacity alloying electrodes for lithium ion batteries. We demonstrate that interfacial chemistry affects electrochemical access to different phases of lithiated germanium, and by carefully controlling the nanowire surface chemistry, we eliminate the need for the

fluorinated electrolyte additives typically required for the stable cycling of group-IV-based, lithium-ion battery electrodes. In addition, we demonstrate that by balancing precursor decomposition kinetics, alloyed silicon-germanium (SiGe) nanowires can be synthesized through supercritical-fluid-based processes, potentially improving the rate capability of high-capacity silicon-based electrode materials produced via scalable processes. We anticipate that the information gained from these solution-based synthetic methods, assembly techniques, and surface chemistry studies will inform synthetic compositional control, elucidate relationships between solution-based reaction parameters and emergent properties, and advance the integration of solution-grown semiconductor nanowires into next-generation devices.

TABLE OF CONTENTS

LIST OF FIGURES

ACKNOWLEDGEMENTS

This dissertation would not exist without the support of the many bright, passionate, and inspiring people in my life. First, I want to thank my advisor, Professor Vincent Holmberg, who has been a constant source of insight and enthusiasm over the last few years. Thank you for allowing be to be a part of setting up your lab and for the countless hours that you invested in me through hands-on lab training and research discussions. Your encouragement of creativity and autonomy helped me grow as a researcher, engineer, and person, for which I am incredibly thankful. I am also grateful to my committee members—Professor Lilo Pozzo, Professor Daniel Schwartz, and Professor Peter Pauzauskie—who all provided invaluable feedback, perspectives, and opportunities that shaped my graduate school experience in profound ways. I also want to thank Professor Elizabeth Nance for founding Women in Chemical Engineering and for her constant efforts to create an inclusive community.

I want to thank my lab mates for their camaraderie in the trenches of scientific research. In particular, I want to thank Grant Williamson for his inspirational persistence and for sharing his electrochemistry knowledge. I am also extremely appreciative of Ge Gu and his hard work in support of recent projects. Thank you to current and former lab mates, including Soohyung Lee, Nicole Thompson, Brittany Bishop, Guesang Kevin Lee, Yao-Yu Li, Chih-Wei Hsu, and Sabiha Rustam, for scientific and moral support.

I also feel fortunate to have worked with such industrious collaborators, many of whom I also consider friends. I want to thank Professor Cody Schlenker's lab, and Jarred Olson specifically, for sharing his knowledge of electrode fabrication and battery testing. I am also grateful to Professor Peter Pauzauskie's lab, and Matthew Crane specifically, for his wizardry with

optics as well as fruitful research chats. Thanks also goes to Professor Lilo Pozzo's lab, particularly Yi-Ting Lee and David Li, both of whom were instrumental to the experiments performed at the Advanced Photon Source. I also want to thank the students and postdocs in the MEM-C IRG-1 and my fellow founding TAs of the EMDS lab for creating an engaging and dynamic research culture.

I am extremely grateful for my friends, all of whom have inspired me through their character, drive, and passions. In particular, I want to thank Elisa Harrison, Willy Voje, Susan Liu, Ed Michor, Barry Badeau, Kyle Caldwell, Trevor Braun, Matt Murbach, Mark and Kathy Borysiak, and Sam Leick for instantly making Seattle feel like home and for imparting impactful pieces of advice over the years. I am also incredibly grateful to have navigated graduate school and the dissertation writing process alongside Emily Ruskowitz, who was always willing to lend an ear (and a cup of tea) during both tedious and tumultuous times. I also want to thank the graduate students who joined the department after me, who brought fresh energy and continue to build an inclusive and fun community, including Brian Gerwe, Jon Witt, Victor Hu, Sarah Alamdari, Luke Gibson, Kelly Carpenter, Caitlin Parke, Julia King, Erica Eggleton, and many more. Thank you, Lexi Walls and Ericka Garufi, for being tremendously supportive friends/roommates and for always being willing to indulge in a hike or an ice cream date. I want to thank Matt (again!) for being an outstanding partner both in and out of the lab, sparking countless laughing fits, and being endlessly supportive through all avenues of growth. Thank you, Bean and David Bowie (my two cats), for constant cuteness, cuddles, and amusement.

Finally, I am indebted to my family, who instilled a sense of curiosity in me and provided unconditional love throughout my life. Thank you for encouraging me to pursue my dreams, no matter how many times those dreams may have shifted shape. To my bonus mom, Karen, thank

you for not sending me off to the Alaskan deep-sea fishing boat (though I probably ended up closer to Alaska than you may have intended). To my brother, Russell, thank you for setting an example to make the world a better place, offering down-to-earth perspectives, and injecting a bit of humor to every situation. To my dad, thank you for encouraging persistence and hard work while also emphasizing the importance of work-life balance. To my mom, thank you for encouraging creativity and gumption and for the reminders that every experience is a learning experience. Lastly, I am incredibly grateful to have had my Papa Dave (Dr. Dave Pandres, Jr.) as a research role model and as one of my biggest supporters to pursue a STEM Ph.D.

DEDICATION

For my family and loved ones

Chapter 1. INTRODUCTION

1.1 SEMICONDUCTOR NANOWIRES

Semiconductor nanowires represent a class of single-crystalline materials with small diameters—on the order of tens of nanometers—and lengths reaching micrometers or even millimeters. These anisotropic semiconductor nanomaterials can exhibit considerably different electronic,[1–3] optical,[4–6] and mechanical[7–9] properties than their bulk counterparts. For example, quantum confinement along the radial dimension enables band gap modification of nanowires; by decreasing the diameter, the band gap increases.[10,11] Semiconductor nanowires can also tolerate higher tensile and flexural strain than bulk semiconductors.[7,8] Moreover, due to their long lengths and small diameters, nanowires have a remarkably high surface area. These exemplary properties have resulted in a surge of research surrounding the production and development of nanowires for applications such as sensing,[12–14] energy conversion,[15–19] and energy storage.[20–25]

Although the high surface area of nanowires makes them an attractive class of materials for a wide range of applications, the viability of semiconductor nanowires to become a disruptive technology will greatly benefit from the implementation of scalable nanowire growth processes as well as the careful consideration of how nanowire surfaces interact with the intended environment. Moreover, development of methods to align and assemble semiconductor nanowires will be beneficial for applications that require nanowires in particular orientations and assembled into certain structures.

1.2 SEEDED-GROWTH OF SEMICONDUCTOR NANOWIRES

The production of nanowires typically falls within one of two paradigms: top-down or bottom up. Top-down processes, such as lithography or wet-chemical etching, are commonly used for applications that rely on precise placement and have been widely implemented throughout the semiconductor device fabrication industry.[26] Although these processes are often compatible with existing technologies because they enable precise position of nanoscale materials, they also etch bulk semiconductor materials to manufacture nanoscale materials, which produces waste.[27]

Bottom-up methods offer alternative synthetic routes with distinct advantages. Specifically, semiconductor nanowires grown through bottom-up methods have demonstrated different mechanical properties[8,28] and surface states[26] when compared to their top-down congeners. Bottom-up processes, such as seeded-nanowire growth, have been demonstrated for a vast range of semiconductor compositions through a variety of different experimental setups.[25,29–37] Moreover, bottom-up processes are considered to be additive, rather than subtractive, and generally produce less semiconductor waste than top-down methods. Advances within the last few decades have also improved the production scalability of semiconductor nanowires, making these materials more accessible for a variety of applications.[33,38,39]

1.2.1 *Vapor-based semiconductor nanowire growth*

The first demonstration of seeded filamentary semiconductor crystal growth was termed vapor-liquid-solid (VLS) growth by Wagner and Ellis in 1964;[29] the three phases in the name signify the phases of the semiconductor precursor, the metal seed, and the deposited anisotropic crystalline semiconductor, respectively.[40] In the first demonstration of anisotropic semiconductor growth, Wagner and Ellis used gold seeds to grow silicon “whiskers”. The VLS process was then

extended to grow nanoscale anisotropic semiconductors, or nanowires.[41] The binary phase diagram (Figure 1.1) of gold-germanium is helpful to illustrate the VLS growth process,[42] though the process is transferable to other types of metal-semiconductor material systems.[38,43,44]

The VLS growth process begins on the left side of the binary phase diagram at point 1, with the solid gold seed. As a vapor-phase germanium precursor is introduced into the chemical vapor deposition (CVD) chamber and decomposes, germanium atoms diffuse into the gold seed. As more germanium incorporates into the gold seed, the seed eventually reaches the liquidus line at point 2, whereupon the solid gold-germanium alloy seed becomes an entirely liquified alloy. If the flow of germanium precursor is sustained, then the alloy droplet continues to increase in germanium content. Eventually, the liquified alloy reaches a saturation at point 3, whereupon crystalline germanium precipitates anisotropically. As soon as a solid crystal of silicon precipitates from the liquid alloy droplet, this becomes the lowest energy interface for further crystalline germanium precipitation.

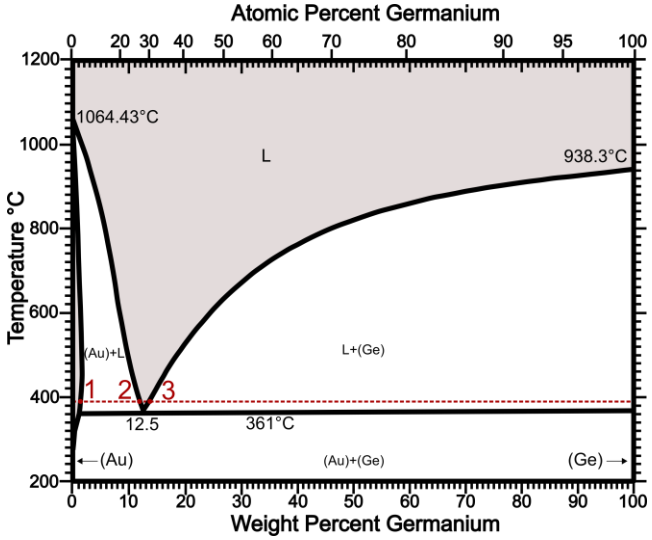

Figure 1.1. Binary-phase diagram of gold and germanium.[42] The dotted red line represents a typical reaction temperature for an isothermal gold-seeded germanium nanowire synthesis at 380ºC. Point 1 is representative of the gold nanocrystal and acts as the starting point for the nanowire growth

process. As germanium atoms diffuse into the gold nanocrystal, we eventually reach point 2, which is representative of the saturated, liquid alloy droplet. As germanium content continues to increase, the Au-Ge alloy droplet reaches point 3, supersaturation, where precipitation of crystalline germanium begins, which facilitates anisotropic semiconductor nanowire growth.

The binary phase diagram depicted here is representative of the bulk gold-germanium system. While equilibrium binary phase diagrams are helpful in selecting feasible metal seed-semiconductor nanowire material systems and reaction temperatures, the high surface energies associated with nanoscale systems can result in modified binary phase diagrams.[45–47] As the size of the alloy droplet is decreased, the semiconductor content increases in the alloy droplet; this phenomenon is due to the Gibbs-Thomson effect and can be visualized as a depression of the liquidus line.[45–47]

The VLS growth process is typically performed in a chemical vapor deposition (CVD) chamber and remains one of the most prevalent methods for semiconductor nanowire growth.[38,48,49] Moreover, VLS nanowire growth can produce complex, axially-[50,51] or radially-heterostructured[52–54] nanowires and can also control specific placement[55] and orientation of nanowires grown vertically from a substrate.[56,57] However, nanowire growth via vapor-phase precursors typically require vacuum-based processes and often result in only a few micrograms of product, making it a difficult process to scale in a cost-effective manner. Without the ability to scale new technologies, a gap persists between lab-scale syntheses and commercial viability.

1.2.2 *Solution-based semiconductor nanowire growth*

Solution-based nanowire growth processes, such as solution-liquid solid (SLS)[33,58–63] and supercritical fluid-liquid-solid (SFLS) growth,[34,39,64,65] can be treated as mechanistic analogues to

VLS, in which semiconductor precursor are supplied in the solution or supercritical fluid phase. Using the solution to transport the semiconductor precursor eliminates the need for expensive vacuum-based techniques. Solution-based growth has the added advantage of using colloidal dispersions of nanocrystals, rather than substrate-based growth, which increases the total reaction volume available. As a result, colloidal, solution-based systems produce a much greater yield of semiconductor nanowires, likely making these processes more cost-effective to scale.[66–68] In particular, SFLS-based growth is an attractive method for high-yield production of nanowires due to its potential to be run continuously.[34,67,69] The temperatures afforded by pressurizing and heating low boiling point solvents to their supercritical fluid phase also broaden the range of accessible temperatures for chemistries compared to solution-based nanowire growth, which relies on high boiling point solvents to access high temperatures at atmospheric pressure. Additionally, the use of low boiling point solvents,[67] such as toluene, benzene, or hexane, make purification processes and surface chemistry reactions considerably easier than SLS-based nanowire growth, which require high boiling point solvents to access high temperatures at atmospheric pressure.[33,37,58,70]

In addition to considering the scalability of semiconductor nanowire production processes, careful consideration of surface chemistry is an important aspect for nearly every application of semiconductor nanowires.[26,71–73] For bulk semiconductors, etching processes are often used to prepare the surface for further chemical functionalization or passivation reactions.[74–76] Although these types of etching process can be used for nanowires,[77] they are not ideal as they add processing steps that include the use of harsh acids. Moreover, the multi-step etching process can cause degradation of the thin nanowires and decrease the stability of the final surface functionalization.[77] In contrast, *in situ* thermally-initiated surface functionalization of semiconductor nanowires, immediately following SFLS-based growth, prior to oxygen exposure, has resulted in stable

organic-monolayer passivated nanowires that are resistant to oxidative and corrosive environments.[77,78]

1.2.3 *Guiding principles for seeded-semiconductor nanowire growth*

Semiconductor nanowire growth involves a dynamic range of phenomena such as heat and mass transport, precursor decomposition and crystal nucleation kinetics, and thermodynamics which can influence the nanowire growth direction,[79–81] growth rate,[54,82–84] composition,[70,85–87] and phase.[88–92] Semiconductor nanowires typically grow in a manner that minimizes the total free energy of the system. As a result, the growth dynamics are highly dependent on the nanocrystal seed.[43,79,93–98] The triple-phase boundary—located at the interface of the metal seed, the nanowire, and the surrounding fluid medium (Figure 1.2)—influences many aspects of nanowire growth. In addition, the triple-phase boundary is different for each metal-semiconductor material system due to the different surface energies associated with each material system.

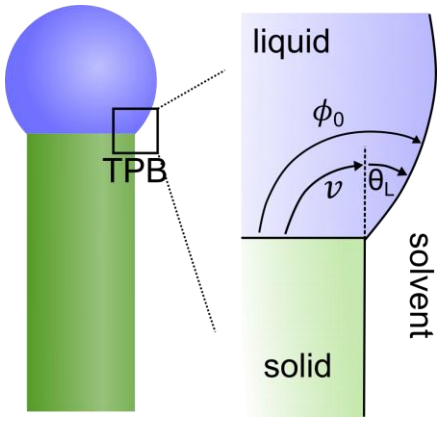

Figure 1.2. A diagram of the triple phase boundary located at the tip of the semiconductor nanowire. The triple phase boundary is the junction of the metal seed, the semiconductor nanowire and the fluid-phase precursor.

The dynamics at the triple phase boundary are largely governed by the surface tensions at the solid-solvent (σ_{SG}), the solid-liquid (σ_{SL}), and the liquid-solvent (σ_{LG}) interfaces. The equilibrium contact angle (ϕ_0) is defined by Young's equation:[93,99]

$$cos\phi_0 = \frac{\sigma_{SG}-\sigma_{SL}}{\sigma_{LG}} \quad (1.1)$$

In addition to the equilibrium contact angle, the contact angle between the liquid droplet and the and the nanowire (θ_L) is defined by:

$$\theta_L = \phi_0 - v \quad (1.2)$$

Importantly, the contact angle (ϕ) between the growth surface at the tip of the nanowire and the liquid alloy droplet can fluctuate during nanowire growth. To maintain nanowire growth, the alloy seed must follow the condition that $v + \theta_L > \phi_0$; simply, the contact angle must not drop below the equilibrium contact angle, which is dictated by the relative surface tensions.[93] After additional crystallographic layers have been precipitated from the alloy droplet, the droplet must also be able to de-wet from the side of the nanowire in order to allow for continuous nanowire growth. Notably, in III-V semiconductor nanowires, the fluctuation of the contact angle enables frequent formation of planar twin defects in order to minimize the precipitation of high surface energy facets.[4,65,93,100] For some systems, such as bismuth-seeded group III-V nanowires, the equilibrium contact angle is large enough to facilitate planar twin defects without fluctuation of the contact angle.[93] To engineer the contact angle at the triple phase boundary, the surface tension at the triple-phase boundary has been controlled through droplet composition, electric fields, and surface chemistries, resulting in directed nanowire growth.[80,81,101,102]

Semiconductor nanowires can also be grown from solid seeds through VSS, SSS, and SFSS processes.[88,103,104] By using a *solid* seed to facilitate semiconductor nanowire growth, the contact angle at the triple phase boundary can be fixed. Minimizing fluctuations of the contact angle

through solid-phase seeding has enabled growth of nanowires with much lower defect densities compared to the same semiconductor nanowire system grown from a liquid alloy droplet.[88,105] Similarly, while some semiconductor nanowires grown from liquid seeds often have a mixture of crystallographic phases (such as wurtzite and zinc blend), using a solid seed to direct nanowire growth produced nearly phase pure semiconductor nanowires, favoring the wurtzite phase with a lower nucleation barrier.[88] Also, the solid seeds are less likely to coalesce during wire growth, resulting in a narrower nanowire diameter distribution.[104,106,107] While solid-phase seeding maintains certain advantages, the growth rates are often much slower, presumably due to low solubility or diffusivity of the semiconductor atoms in the solid seed.[32,104]

Solution-based nanowire syntheses are also strongly influenced by precursor decomposition kinetics.[37,65,67,69,92] For supercritical fluid-based syntheses, it is particularly important to balance precursor decomposition kinetics as well as the molar ratio of semiconductor precursors and metal seeds in order to avoid homogeneous nucleation of isotropic particles.[108] In supercritical fluid-based synthesis of silicon and germanium nanowires, the precursor decomposition kinetics can be influenced by reaction temperature, degree of aryl substitution, and solvent choice.[67,69,70,108] Both aryl- silanes and germanes undergo disproportionation reactions prior to semiconductor nanowire growth. By increasing the degree of aryl substitutions, the rate of the disproportionation reaction can be decreased, resulting in a slower supply of semiconductor atoms to the metal seed. Similarly, balancing precursor dynamics is important for III-V[109] and II-VI[92] nanowires. Importantly, if the precursor decomposition kinetics are too slow in supercritical fluid-based syntheses, resulting in slow mass transport of the semiconductor atoms to the seeds, the resulting semiconductor nanowires may have a tortuous morphology or may not grow at all.[108]

As an additional handle to tune precursor decomposition kinetics, the reaction medium can be leveraged to influence the disproportionation reaction of aryl precursors.[67] Solvents such as hexane have shown low (1.4%) yield of silicon nanowires grown with monophenylsilane, whereas toluene and benzene, under identical reaction parameters, resulted in a 38% and 63% yield, respectively.[67] The difference in yield as a function of solvent is thought to be a result of a solvent-mediation effect during the precursor disproportionation reaction as aryl-silanes decompose to liberate silane[67].

1.3 CHALLENGES FOR SOLUTION-PHASE SEEDED NANOWIRE GROWTH

To-date, semiconductor nanowires have been used for cell scaffolds,[110–113] sensors,[12,38,49,114–116] photonics,[50,117–123] electronics,[124–129] quantum computing,[130,130–136] energy conversion,[18,137,137–145] and energy storage.[20,21,23,25,59,69,70,146,147] For many applications, particularly those that require a high mass or volume of nanowires, the ability to produce a high yield at low cost is a major hurdle to commercial viability. The development of solution-phase semiconductor nanowire synthesis has greatly improved the scalability of semiconductor nanowire synthesis.[33,38,66,69] However, there are still a number of challenges for solution-grown nanowires.

Certain capabilities of vapor-based nanowire growth would be desirable to translate to solution-based processes. Yet, there still exist synthetic capabilities that have been difficult to achieve for both vapor-based and solution-based growth methods. In particular, we would like to be able to observe and measure solution-based nanowire growth dynamics, improve complex compositional control over nanowires grown through solution-based processes, and assemble solution-grown nanowires into larger ensembles and precise hierarchical structures.

Additionally, because nanowires have an extremely high surface area to volume ratio, understanding how nanowire surface chemistry affects device performance will be important. In order for nanowires grown through vapor-based nanowire growth techniques to have controlled surface chemistry, additional acid-etching processes are required to remove surface oxides prior to any surface functionalization which can compromise the desired surface functionalization on the nanowire.[74,75,148,149] Supercritical fluid-based nanowire growth methods are uniquely positioned to carefully control nanowire surface chemistry through *in situ* thermally initiated surface functionalization.[69,77,78] However, the dynamic between surface chemistry and device performance, especially after integration into electrodes for battery applications, is not yet fully understood. In the following sections, we will expand upon the challenges associated with nanowire synthesis and integration and briefly describe some strategies that have been developed to address these challenges.

1.3.1 *Observing and measuring solution-phase nanowire growth dynamics*

The ability to observe and measure nanowire growth in solution could enhance our understanding of solution-based nanowire growth dynamics, potentially broadening the scope of synthetic possibilities. Observations during vapor-based nanowire growth, including *in situ* TEM studies,[32,150,151] *operando* infrared spectroscopy,[152] and optical scattering,[153] have provided us with invaluable information towards our fundamental understanding of seeded semiconductor nanowire growth. From these studies, the field has developed a better understanding of how certain synthetic parameters influence nanowire nucleation kinetics,[154] growth rate,[54,155] growth direction,[94,156] morphology,[157–159] phase selection,[89,160] and defect incorporation.[161–163] However, major differences exist between vapor-based and solution-based nanowire growth that prevent smooth

translation of techniques from one method to the other. For example, vapor-based nanowire growth occurs over the time scale of minutes to hours, whereas solution-based nanowire growth ranges from seconds to minutes.

Although the faster nanowire growth rate makes solution-based semiconductor nanowire growth processes more scalable, it also makes measuring and observing growth dynamics more difficult. Moreover, because thermal energy sources used to drive reactions often require resistive heating equipment, such as heating nests or heating blocks, and since many reactions require thick-walled metal vessels to maintain high or low pressure, the reaction solution can be difficult to access for *in situ* measurements. In order to observe solution-based nanowire growth *in situ*, providing alternative energy sources that do not rely on resistive heating or high-pressure/low-pressure equipment can facilitate tracking of nanowire growth dynamics in solution.[164] Expanding upon these types of alternative solution-based nanowire growth strategies could enable *in situ* observation of solution-based nanowire growth, providing real-time information, which could in turn, provide rapid and iterative feedback to improve synthetic control.

1.3.2 *Improving control over solution-grown semiconductor nanowire composition*

A notable challenge of nanowire growth—across both vapor- and solution-based syntheses—is the intentional and homogeneous incorporation of dopants. Incorporating dopants into semiconductor nanowires serves as a handle to adjust the electronic and optical properties. Being able to rationally control the degree of dopants would be beneficial for thermoelectric,[139,165] quantum computing and information,[166,167] sensing,[12,168] and photonic applications.[169–171] One tactic to incorporate dopants into nanowires is through ion implantation. While ion implantation enables solubility-independent incorporation of dopants, it also risks damaging the integrity of the

semiconductor nanowire.[172,173] An alternative strategy to incorporate dopants into nanowires is to include a post-growth diffusional doping process, which can either involve reacting a dopant-containing molecule with the nanowire surface[174] or epitaxially growing a dopant-containing shell and then annealing the nanowires to drive dopant diffusion.[175] Such strategies have had mixed success and are dependent on the temperature-dependent diffusion coefficient of the dopant atom in the semiconductor host lattice. Instead of using post-synthetic doping strategies, incorporating dopants during the semiconductor nanowire growth process could potentially result in nanowires with a homogeneous distribution of dopants and could also be a more cost-effective strategy to produce doped semiconductor nanowires.

Both vapor- and solution-based semiconductor nanowire growth methods have had some degree of success with incorporating dopants during nanowire synthesis, rather than through post-synthetic processing techniques. One strategy involves selectively choosing a metal seed for nanowire growth that also acts as a reservoir of dopant atoms. A range of metal and alloy nanocrystals, such as Mn, Al, Ga, Sn, have been investigated as promotors for semiconductor nanowire growth and as sources of dopant atoms to alter the electronic and optical properties of nanowires.[176–182] However, using the metal seed as a source of dopant atoms is limited to certain metal-semiconductor material systems in which the metal is soluble in the semiconductor nanowire. Equilibrium phase diagrams are especially helpful for identifying such material systems.

Dopants can also be incorporated into semiconductor nanowires during growth through a dopant-containing molecular precursor by balancing precursor decomposition kinetics and precursor solubilities in the metal-semiconductor alloy melt.[183] Notably, vapor-based growth uses gaseous dopant precursors, which can also diffuse through the nanowire sidewall and contribute to an inhomogeneous, radial dopant distribution throughout the length of the nanowire.[184] Despite

the inhomogeneity associated with *in situ* doping of nanowires through vapor-based processes,[162] it remains one of the few ways to successfully introduce dopants into semiconductor nanowires during growth across group IV,[87,182,185–187] II-VI,[175,188] and III-V[189–191] material systems, for both n- and p-type dopants. Introducing dopants into semiconductor nanowires through solution-based processes remains limited to a handful of demonstrations such as Mn- and Eu-doped Bi-seeded CdS nanowires[192] as well as Mn-doped CdSe nanowires.[62] This highlights the difficulty associated with developing new, solution-based strategies in to synthesize homogeneously doped semiconductor nanowires.

1.3.3 *Assembly of semiconductor nanowires*

The ability to synthesize nanoscale materials with well-defined size dimensions and compositions through solution-based processes has vastly improved over the past few decades and will continue to advance as we discover additional methods to control and modify nanomaterial growth processes.[193] Solution-phase synthesis of nanomaterials has enabled well-defined nanomaterial morphology[58,63,193–197,197] and surface chemistry[69,77,198–200], which is especially important, given the high surface area to volume ratio of nanomaterials. However, the ability to assemble nanostructures for integration into devices is still somewhat limited, especially in comparison to top-down lithographic techniques, which excel at achieving precise placement of nanostructures.[26,201]

Nanowires grown through vapor-based techniques have an inherent advantage in terms of assembly because they are typically grown from substrates, often resulting in aligned vertical arrays of nanowires. These types of as-grown, straight, aligned arrays of nanowires, have been integrated into devices as light emitting diodes,[53,202,203] solar cells,[5,204,205] and quantum information

applications.[206–208] Although the product of aligned semiconductor nanowires can be more easily integrated into some devices, the vapor-based growth process is limited in scalability. Nanowires grown through solution-based methods are often unaligned and tangled because they are grown from metal seeds dispersed in a solvent. While it is possible to simply place a metal nanocrystal-decorated substrate in a solution-phase reaction,[37,146,209] this tactic negates the desirable aspects of scalability associated with using to a solution-based, colloidal system. Moreover, the nanowires grown from a substrate in solution are often connected to the substrate, but still unaligned. In order to integrate solution-grown semiconductor nanowires into the wide range of their proposed applications, a variety of assembly processes should exist to fit the different needs of such applications.

To assemble bulk volumes of semiconductor nanowires into macroscopic materials for further integration into devices, a number of techniques have been implemented. Nonwoven nanowire fabrics have been produced simply by drop-casting a concentrated nanowire dispersion into a trough and allowing the solvent to evaporate.[21,210] These types of nonwoven fabrics have been integrated as a binder-free negative electrode for lithium ion batteries.[21] In addition, macroscopic semiconductor nanowire yarns have been produced through light-induced nanowire assembly, which used separated photogenerated charge carriers and an applied electric field to induce dipoles within the nanowire, facilitating nanowire bundling.[211] Flow-assisted dielectrophoresis, combined with impedance spectroscopy, was used to simultaneously select semiconductor nanowires with favorable electronic properties and to align solution-grown nanowires across electrodes.[212] Additional techniques to align numerous semiconductor nanowires relative to each other include, but are not limited to, contact printing,[213–215] dip-coating,[216–218] shear forces,[219,220] and molecular forces.[221,222]

A handful of strategies have been devised to place single nanowires into predetermined locations on substrates and within devices. For example, a combination of dielectrophoretic and microfluidic assembly was used to achieve precise placement of thousands of single nanowires across patterned metal electrodes.[223] Additional variations of dielectrophoresis, fluidic assembly, and optical traps have been used to systematically place semiconductor nanowires into precise locations.[224,225] Notably, optical traps, which can provide three-dimensional control over single nanoparticles in solution, have been used to pin nanomaterials to specific locations on substrates into complex configurations.[226]

Despite the impressive feats achieved through alignment and assembly processes to-date, challenges remain for nanomaterial assembly, especially for nanomaterials grown from solution processes. For example, our ability to create precise heterojunctions and assemble nanomaterials into integrated hierarchical structures remains somewhat limited. As more methods are discovered to manipulate and place nanowires in specific locations, new developments will push the boundary of nanomaterial integration and technological discovery.

1.3.4 *Improving the energy density of lithium ion batteries*

Increasing the energy density of energy storage systems remains a major obstacle for the widespread adoption and integration of renewable energy in order to address the climate crisis.[227,228] As we integrate a larger fraction of renewable energy (wind, solar, etc) into our energy portfolio to combat the climate crisis, our energy sources will become more intermittent on a daily a basis as well as throughout the year.[229] Although high energy demands and low energy supply can be supplemented with energy provided by fossil fuels, this should be mitigated as much as possible. Instead, energy storage systems that can provide energy during times of high demand

and low supply will be key to our energy security. Moreover, despite the progress associated with implementing renewable energy sources into energy demands of residential and commercial sectors, the transportation sector within the United States still sources ~70% of its energy from petroleum.[230]

Although lithium ion batteries are not as energy dense as petroleum, they are still well-suited to transform the transportation industry and are already being used in commercial electric vehicles.[229] For a rechargeable battery, lithium ion batteries have one of the highest energy densities when compared to other types of battery technologies. Although lithium ion batteries are not as energy dense as petroleum, electric vehicles are still capable of covering the distance of an average daily commute (40 miles) and can even traverse over 300 miles on a single charge.[231–233] Currently, carbon-based active materials such as graphite are still the most commonly used negative electrode material for lithium ion batteries, due to stability over extended cycling, low cost, and reproducibility. However, graphite has a relatively low theoretical gravimetric capacity (372 mAh/g) and will likely need to be replaced in order to achieve lithium ion batteries with higher energy densities.[229]

Group IV materials, such as silicon and germanium, have attracted increasing interest as negative electrode materials for lithium ion (Li-ion) batteries.[20–22,227,234–238] Silicon and germanium have high theoretical gravimetric capacities that are electrochemically accessible at room temperature, 3579 mAh/g and 1384 mAh/g, respectively, which are an order of magnitude higher than the current standard for Li-ion negative electrodes, graphite.[22,238,239] However, both silicon and germanium undergo large volume changes (~300%) upon lithiation and delithiation, which can cause electrode fracture, deleterious irreversible reactions that trap lithium ions, and loss of contact with the current collector.[240–247] Nonetheless, the strain and electrode fracture associated

with volume changes can be mitigated to an extent by nanostructuring alloying electrode materials.[20,234–236,248–254]

Nanowires are particularly advantageous for lithium ion batteries due to their ability to withstand the large volume expansion associated with lithiation,[20,251] which typically results in electrode fracture and degradation of bulk or thin film electrodes.[235] They are also an archetypal geometry for electrodes because they afford a high surface area for fast electrochemical reactions and a continuous percolation network for transport.[146] In addition to their advantageous material and morphological properties, the ability to produce semiconductor nanowires on a large scale through supercritical fluid-based processes makes them unique target materials for battery applications. However, the instability of typical electrolyte solvents within the voltage window for lithium ion batteries can result in recurring parasitic reactions at exposed silicon or germanium electrode surfaces, highlighting the criticality of interfacial chemistry for electrode stability.[255,256]

1.4 DISSERTATION OVERVIEW

The research included in this dissertation focuses on the development of scalable, solution-based production of semiconductor nanowires and the nuanced challenges associated with their integration into devices. This work aims to develop new, solution-based semiconductor nanowire growth processes to facilitate *in situ* characterization; to advance strategies for creating compositionally complex semiconductor nanowires—both for doped and alloyed semiconductor nanowires; and to build on existing assembly strategies to create hierarchical materials from semiconductor nanowire building blocks. Lastly, this work aims to understand how surface functionalizing semiconductor nanowires affects their performance as the active material in negative electrodes for lithium ion batteries.

Chapters 2 and 3 will discuss a new method of semiconductor nanowire production which uses irradiated, colloidal low-melting point metal nanocrystals as photothermal transducers to thermally drive decomposition of semiconductor precursors and simultaneously as seeds to facilitate anisotropic growth of semiconductor nanowires. In particular, Chapter 2 will highlight the versatility of this photothermally-driven nanowire growth process, demonstrating growth of II-VI and group IV nanowires from molecular precursors in an optically accessible cuvette on a benchtop. Chapter 2 will also demonstrate how this type of laser-induced solution-liquid solid growth can be translated to a continuous-flow setup, enabling rapid testing and optimization of nanowire growth parameters. In addition, Chapter 2 will discuss recent efforts to use magic-sized clusters as single-source precursors for III-V semiconductor nanowire growth.

Chapter 3 will leverage the ability to grow semiconductor nanowires in solution on the benchtop in an optically accessible reactor to study laser-driven, solution-based nanowire growth and dynamics via ultra-small-angle X-ray scattering. Moreover, we demonstrate the ability to examine the effects of nanocrystal number density and laser power on bismuth-seeded cadmium selenide nanowire growth rates. In addition, we demonstrate on-demand, stepwise nanowire growth simply by turning the incident irradiation on and off.

Whereas Chapters 2 and 3 highlight semiconductor nanowire growth through optically driven processes, Chapter 4 will discuss a method to manipulate and assemble semiconductor nanowires using a laser beam that has been highly focused to form an optical trap. This chapter demonstrates the use of an optical trap to align and assemble inorganic nanomaterials in non-aqueous solvents, broadening the range of temperatures and chemistries possible within an optical trap. We then assemble metal-seeded semiconductor nanowire building blocks into hierarchical

metal-semiconductor heterostructures via the high temperatures afforded by photonic soldering in a high boiling point solvent.

Chapters 5 and 6 discuss the synthesis of group IV nanowires in supercritical organic solvents and their performance as negative electrode active materials for lithium-ion batteries. Chapter 5 focuses on the importance of the interfacial chemistry at the germanium nanowire-electrolyte interface. We show that functionalizing the nanowire surface can improve electrode performance without the need for expensive fluorinated electrolyte additives that are typically required for stable cycling of group IV materials. In addition, Chapter 5 will demonstrate how different slurry processing techniques for highly anisotropic nanomaterials can affect final device performance. Chapter 6 discusses recent efforts to improve compositional control of nanowires through supercritical fluid-based processes, enabling growth of alloyed silicon-germanium nanowires for tunable capacity and rate capability. Chapter 7 will highlight conclusions from these studies and expand upon areas of interest for future work.

Chapter 2. LASER-DRIVEN SOLUTION-LIQUID-SOLID GROWTH OF SEMICONDUCTOR NANOWIRES

The work presented in this chapter is the result of a highly collaborative project between the Holmberg lab and the Pauzauskie lab (UW Materials Science & Engineerng). Dr. Matthew Crane, Professor Jim Davis, and Professor Peter Pauzauskie contributed significant efforts towards developing heat transport models that enhanced our understanding of phenomena observed in this work.

2.1 INTRODUCTION

The absorption of light and subsequent energy transfer processes affords a unique handle for initiating chemical reactions in a wide range of materials and processes for diverse applications. For example, light absorption by photosensitive molecules can be used to initiate photopolymerization and photoconjugation to spatially control the chemical and physical properties of biomaterials[257–259] as well as to control photodegradation for tissue engineering[260,261] and targeted therapeutic delivery.[262,263] In addition, light can be used to initiate surface reactions, thereby imparting additional functionality to the surfaces of inorganic materials.[148,264] In each of these examples, the energy from the incident radiation is transferred through a photoinitiator to start the chemical reaction or a certain wavelength is chosen to target a specific bond. However, light-driven chemical and physical processes are not limited to photosensitizing molecules for energy transfer or to directly cleaving bonds; inorganic nanomaterials also participate in light-driven energy transfer processes, which can be used to initiate chemical reactions[153,265–273] and phase transformations.[274–279] For instance, irradiation of plasmonic colloidal metal nanoparticles dispersed in water has been used for solar steam generation as well as for off-grid water

purification and medical instrument sterilization.[274–276,280–282] In addition, as another example of the extreme local conditions that can be created under such energy transfer processes, gold nanoparticles can be reshaped under resonant irradiation of their plasmons, which increases their temperature above the boiling point of water.[283,284] In fact, photothermal heating of dilute nanoscale materials can locally superheat water to temperatures greater than 300°C without boiling due to the large Young-Laplace interfacial surface pressures that arise due to nanoscale radii of curvature.[277,285,286] The high temperatures afforded by metal nanocrystal irradiation have been used to induce local reaction conditions at the nanocrystal surface that can be costly and inefficient to create on the bulk scale, as well as to fabricate inorganic, crystalline nanomaterials.[287–289]

Importantly, metal nanocrystals are also commonly used as seeds for the growth of anisotropic semiconductor nanowires.[38] Typically, semiconductor nanowires are grown via the decomposition of a semiconductor precursor and subsequent diffusion of semiconductor atoms into a metal nanocrystal seed, which, upon saturation, facilitates nucleation and continued growth of an anisotropic, crystalline semiconductor nanowire.[290–292] Although semiconductor nanowire synthesis typically involves globally heating a reactor system, some reports have used metal nanocrystals not only as seeds for semiconductor nanowire growth, but also as local heat sources under resonant irradiation to enable precursor decomposition and diffusion.[153,272,273] For example, irradiating metal nanoparticle-decorated substrates in a modified chemical vapor deposition chamber enabled site-specific heating and, ultimately, plasmon-assisted growth of nanowire arrays[272] as well as single nanowires.[153,273] To date, photothermally-driven nanowire growth has largely been studied in substrate-based, gas phase reactions, yet the growth of semiconductor nanowires in solution through direct laser irradiation of colloidal metal nanocrystals remains largely unexplored.

A handful of reports have utilized substrate-bound metal nanocrystals to transduce incident irradiation into thermal energy to decompose semiconductor precursors for nanowire growth using a solution-based carrier phase;[293–295] however, for both vapor- and solution-based nanowire growth, past work has exclusively focused on irradiating a substrate that has been decorated with metal nanocrystals.[153,272,273,293–295] While this substrate-based configuration exploits the photothermal heating of gold nanocrystals, it lacks the potentially advantageous scalability afforded by solution-phase nanowire growth and superheating. Actualizing light-driven, substrate-free, solution-based nanowire growth could enable continuous flow-based nanowire growth on the benchtop, as well as broader access to a range of nanowire chemistries that require high growth temperatures, without the need for expensive or niche equipment.

Here, we capitalize on the unique optical properties of metallic nanomaterials under laser irradiation to act as both a thermal energy source and as a growth-directing seed for the synthesis of anisotropic semiconductor nanostructures through a bottom-up, one-step, colloidal, solution-based process. By using metal nanocrystals to transduce incident irradiation into thermal energy, rather than globally heating the reaction solvent, we lift reactor design constraints to enable the growth of semiconductor nanowires on the benchtop, eliminating the need for specialized, high-temperature or high-pressure equipment. By using a dispersion of nanocrystals, rather than a metal nanocrystal-decorated substrate, we highlight a system in which colloidal nanocrystals irradiated with a broad beam can reach the high temperatures (>200°C) required for solution-phase nanowire synthesis. This demonstrates a generalizable process for semiconductor nanowire growth that can be performed on a benchtop in either batch or continuous operation, for rapid, high-throughput screening and parameter optimization during nanowire growth.

2.2 EXPERIMENTAL DETAILS

2.2.1 *Materials*

Bismuth (III) chloride ($BiCl_3$, 99.99% trace metals basis), cadmium oxide (CdO, ≥99.9% trace metals basis), ethanol (anhydrous, ≤0.005% water), indium (III) chloride (99.999% trace metals basis), isopropanol (anhydrous, 99.5%), molecular sieves (3 Å), n-butyllithium (1.3 M in n-heptane), 1-octadecene (ODE, 90%), oleylamine (90%), oleic acid (degassed, 90%), sodium bis(trimethylsilyl)amide (1.0 M solution in tetrahydrofuran), squalane (96%), Super-Hydride® solution (1.0 M lithium triethylborohydride in tetrahydrofuran), selenium (Se, <5 mm particle size, ≥99.999% trace metals basis), tetrahydrofuran (THF, anhydrous, ≥99.9%), toluene (anhydrous, 99.8%), and trioctylphosphine (TOP, 97%) were purchased from Sigma-Aldrich. Diphenylgermane (>95%) was purchased from Gelest. Poly(1-hexadecene-co-1-vinylpyrrolidinone) (PHD-co-PVP) was provided by Ashland under the trade name Ganex™ V-216. Toluene (Certified ACS, 99.8%) was purchased from Fisher. Ethanol (200 proof) was purchased from Decon Laboratories.

2.2.2 *Bismuth nanocrystal synthesis*

Bismuth nanocrystals were synthesized based on the protocol outlined by Wang, et al.[61] A 25 wt% solution of PHD-co-PVP in 1-octadecene was dried over molecular sieves for one week. $BiCl_3$ (2.6×10^{-2} mmol) was mixed at 800 RPM with THF (570 µL) under nitrogen for forty minutes. The solution of PHD-co-PVP in octadecene (6.1 mL) was added to the flask under continuous mixing at 900 RPM. The flask was cycled between nitrogen and vacuum three times. Sodium bis(trimethylsilyl)amide (825 µL) was injected, and the flask was stirred until a dark orange-brown

color was observed (~10 minutes, 1100 RPM). The solution was then heated to 200°C for 17 hours, cooled, and then transferred into a nitrogen-filled glove box for storage. Bismuth nanocrystals were handled under nitrogen for cleaning. Nanocrystals were washed five times using a 1:4 ratio of anhydrous hexanes:ethanol and centrifugation (6800 RCF for 10 minutes) to remove excess PHD-co-PVP prior to use for nanowire growth. The resulting bismuth stock concentration measured from ICP-AOS was 6.4×10^{-3} mole elemental Bi/L. The average diameter of the bismuth nanocrystal seeds was 52 nm ± 8 nm.

2.2.3 *Indium nanocrystal synthesis*

Indium nanocrystals were synthesized using the protocol outlined by He, et al.[2] $InCl_3$ (1.4×10^{-1} mmol) was measured in the glove box, transferred into a three-neck flask, and attached to a Schlenk line. The flask was purged with nitrogen and then transitioned between vacuum and nitrogen atmosphere three times. Oleylamine (13 mL) was added to the flask, which was heated to 100°C while mixing (1000 RPM) and then placed under vacuum for an additional 45 minutes. The mixture was blanketed with nitrogen and further heated to 160°C. A solution of 1.3 M n-butyllithium in n-heptane (1.3 mL) was injected into the flask, followed by an injection of 1.0 M Super-Hydride® solution (300 µL). The reaction was allowed to run for ten seconds, whereupon 12 mL of anhydrous toluene was injected to cool the solution and quench the reaction. At 50°C, oleic acid (400 µL) was added to stabilize the nanocrystals. Nanocrystals were then transferred into a glove box and handled under nitrogen for cleaning. Anhydrous ethanol (12 mL) was added to the dispersion, which was centrifuged at 4180 RCF 10 minutes. The supernatant was discarded and the nanocrystals were washed with a 2:1 ratio of anhydrous hexanes:ethanol three more times. The average diameter of the indium nanocrystal seeds was 16 nm ± 2 nm.

2.2.4 *Photothermal nanowire growth*

Nanowire precursor growth solutions consisting of metal nanocrystals, molecular semiconductor precursors, and squalane or ODE, were loaded into a screw-top quartz cuvette in the glove box, where the top of the cuvette was lined with Teflon and then wrapped with Parafilm to prevent oxidation of nanocrystals. Nanowire precursor growth solutions for each material system are described in Table A.1. The cuvette with the growth solution was transferred out of the glove box and subsequently irradiated with a polarized near-infrared fiber laser (λ=1070 nm) at a range of powers (15-60 W) and times (5-20 minutes). The resulting product was washed with a 2:1 ratio of toluene and ethanol, collected by centrifugation at 19,000 RCF, dispersed in toluene, and washed two more times.

For a typical continuous flow-based, photothermally driven nanowire growth synthesis, a glass tube with an inner diameter, outer diameter, and length of 4 mm, 5 mm, and 95 mm, respectively, was sealed under a nitrogen atmosphere with two small rubber septa. The reaction vessel was pre-filled with degassed 1-octadecene to displace all nitrogen prior to injection of the nanowire growth solution. The nanowire precursor growth solution, consisting of 60 µL of a Bi nanocrystal dispersion (1.34 mmol/L), 750 µL of Cd-oleate (0.15 M), 1.3 mL of TOP:Se (1.0 M), and 240 µL of degassed 1-ODE, was prepared in a nitrogen-filled glove box and loaded into a syringe. The needle of the precursor syringe was inserted through a rubber septum leading into the reaction vessel and the syringe was fixed onto a syringe pump in order to control the flow rate (5 mL/hr). A second needle was inserted into the other rubber septum on the exit side of the reaction vessel, leading to a glass vial used to collect the nanowire product. Prior to injecting the nanowire precursor growth solution, the laser was aligned to irradiate the center of the reaction vessel. After injecting the glass reactor vessel with the nanowire precursor solution, the reactor was irradiated

with a polarized, near-infrared fiber laser (λ=1070 nm) at 5 W. The product was washed with a 2:1:1 ratio of toluene:chloroform:ethanol, collected by centrifugation at 19,000 RCF, dispersed into toluene, and washed two more times prior to sample characterization.

2.2.5 *Materials characterization*

Transmission electron microscopy (TEM) images were acquired with a FEI Technai G2 F20 Supertwin TEM operating with a 200-kV accelerating voltage and were analyzed using ImageJ Software. X-ray diffraction (XRD) scans were collected using a Bruker D8 Discover equipped with an IμS 2-D XRD detector system and were analyzed using EVA software. Inductively coupled plasma optical emission spectroscopy (ICP-OES) was performed with a Perkin Elmer Optima 8300 spectrophotometer. UV-vis extinction spectra were collected using an Agilent Cary 60 UV-vis spectrophotometer. Time-dependent infrared thermal imaging was performed with a FLIR A325sc camera using the 0-350°C temperature range setting, and the resulting videos were analyzed using ResearchIR software.

2.3 RESULTS AND DISCUSSION

The contact-free, laser-driven, solution-based nanowire growth process is detailed in Figure 2.1, in which a cuvette contains a dispersion of metal nanocrystals and molecular precursors (Figure 2.1i) for semiconductor nanowire growth. Upon irradiation (Figure 2.1ii), the nanocrystals transduce the incident light into thermal energy, which drives the decomposition of molecular semiconductor precursors, thereby facilitating the formation of a saturated metal-semiconductor alloy that enables seeded nanowire growth (Figure 2.1iii).

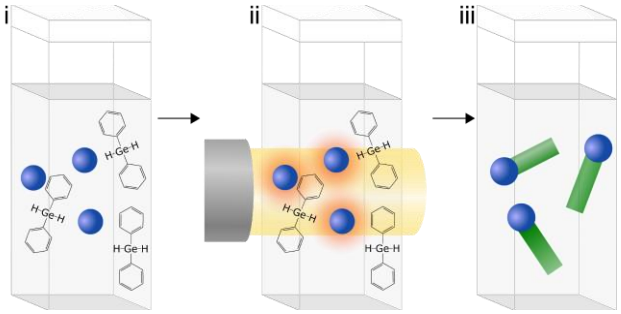

Figure 2.1. Illustration of contact-free, laser-driven, colloidal semiconductor nanowire growth on the benchtop, in a quartz cuvette. (i-iii) The irradiation of colloidal metal nanocrystals with a broad, unfocused laser generates heat in solution, which can then be used to drive local chemistry – such as the decomposition of molecular precursors – thus enabling the contact-free, solution-based, photothermal synthesis of semiconductor nanowires.

2.3.1 *Low-melting point nanocrystals as colloidal, photothermal transducers*

While numerous studies have examined the heating of metal nanocrystals under irradiation, most of these investigations have focused on noble metal nanoparticles, such as gold.[274,275,275–277,277,278,285,286] To examine the potential heating effects afforded by contact-free irradiation of low-melting point colloidal metal nanocrystals, we irradiated bismuth nanocrystals (Figure 2.2) over a range of concentrations, denoted by the optical density of the dispersion at the 1070 nm excitation wavelength.

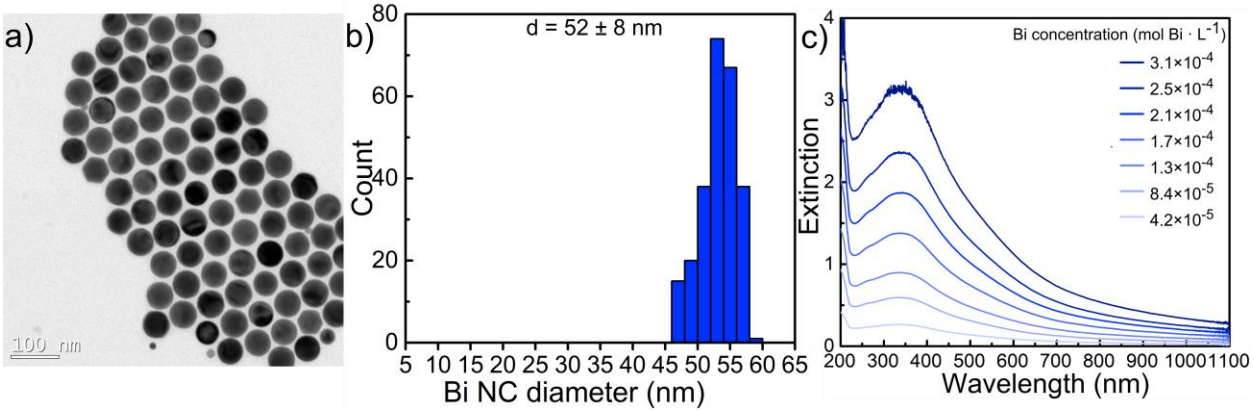

Figure 2.2. (a) TEM image of bismuth nanocrystals, (b) histogram of the bismuth nanocrystal diameter distribution, and (c) extinction spectra of the bismuth nanocrystals used to synthesize Bi-seeded Ge nanowires and CdSe nanowires.

Thermographic infrared images of a bismuth nanocrystal dispersion in ODE (OD_{1070} = 0.52) in a cuvette under irradiation (Figure 2.3e) demonstrate the photothermal transduction characteristics of the colloidal nanocrystals, compared with neat solvent under identical excitation conditions (Figure 2.3a). We note that because the quartz cuvette walls absorb the far infrared light used in thermographic imaging, the measurement only reflects the temperature of the cuvette surface. Thus, the reaction volume is likely at a significantly higher temperature due to heat transfer resistances of both the solvent volume and the quartz cuvette walls. As the optical density of the Bi nanocrystal dispersion increases, the maximum temperature achieved also increases (Figure 2.3, Figure 2.4) whereas the neat solvent temperature increases by a maximum of 17 °C under near-infrared excitation (Figure 2.3a). Therefore, the observed temperature increase of the nanocrystal dispersions is clearly due to bismuth nanocrystal photothermal transduction.

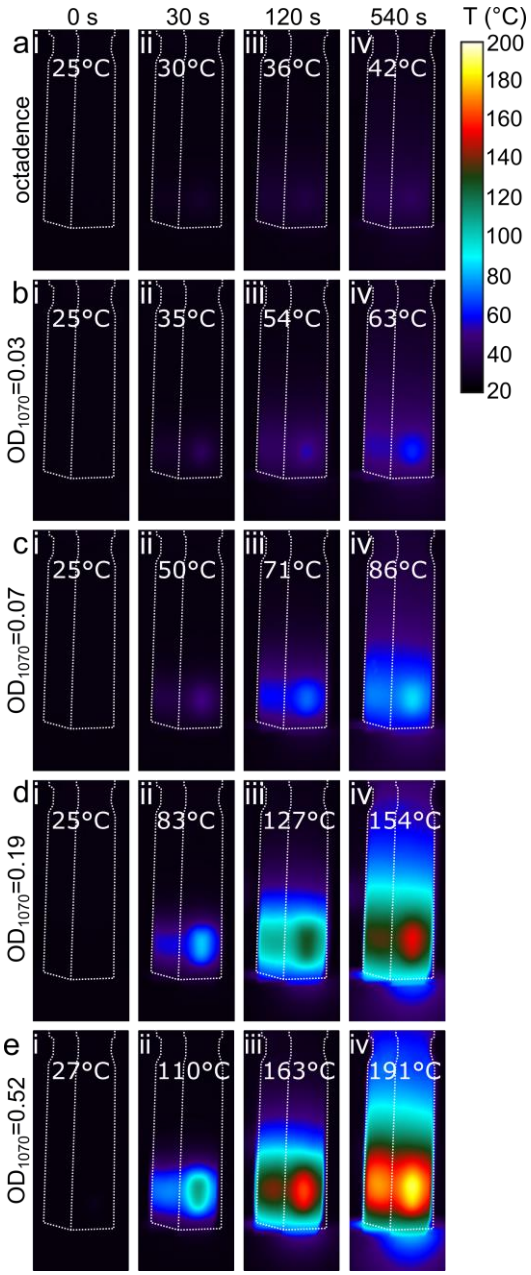

Figure 2.3. Characteristic set of snapshots taken from an infrared thermal imaging camera, illustrating the temporal evolution of (a) neat 1-octadecene in a quartz cuvette under irradiation with a near-infrared laser (1070 nm, 15 W) and (b-e) the photothermally induced temperature distribution of bismuth nanocrystal dispersions (OD_{1070} = 0.03-0.52) in a quartz cuvette under irradiation with a near-infrared laser (1070 nm, 15 W). Temperature labels correspond to the maximum temperature recorded in each image.

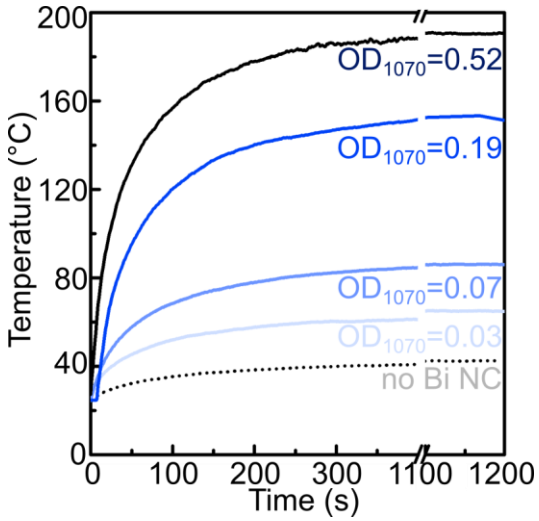

Figure 2.4. Time-dependent temperature profiles for octadecene and a range of bismuth nanocrystal concentrations (OD_{1070} = 0.03-0.52) under 1070-nm irradiation (15 W).

In addition to measuring the bismuth nanocrystal concentration dependence of the temperature profile through infrared thermometry, we used COMSOL to model the surface temperature of an irradiated cuvette containing a bismuth nanocrystal dispersion (Figure 2.5a-d). These numerical solutions accurately predict the surface temperature of the cuvette at low bismuth nanocrystal concentrations; however, the predicted temperatures diverge from the experimentally measured values at higher nanocrystal concentrations and higher temperatures. Inaccurate numerical solutions at higher bismuth nanocrystal concentrations suggest that the model likely fails to account for high-temperature effects, such as solvent boiling, Ostwald ripening, or coalescence of bismuth nanocrystals, which are not included in the model. With this caveat, the numerical model provides an upper bound for the internal temperature profiles and demonstrates that the nanocrystals in the center of the cuvette can reach extraordinarily high temperatures at steady state (cutaway internal temperature profiles can be found in Figure 2.5e-f). Using an analytical solution based on a Mie theory source term, we also calculated the temperatures of single bismuth or indium nanocrystals (discussed later) suspended in an infinite bath of the growth

solution. Under illumination in this formalism, isolated bismuth and indium nanocrystals heat very little relative to the temperature of the overall growth solution, indicating that, at these laser irradiances and absorption coefficients, a single nanocrystal may not sufficiently transduce enough heat to drive an energy-intensive nanowire growth process. Critically, this observation also suggests that the nanocrystals heat via collective absorption and subsequent heat diffusion, which is agreement with previous work performed with gold nanoparticles in an aqueous solution under irradiation.[269,275,280] Thus, the achievable temperature and the ability to drive a nanowire growth reaction will depend on many factors, including the concentration of nanocrystals and the irradiance.

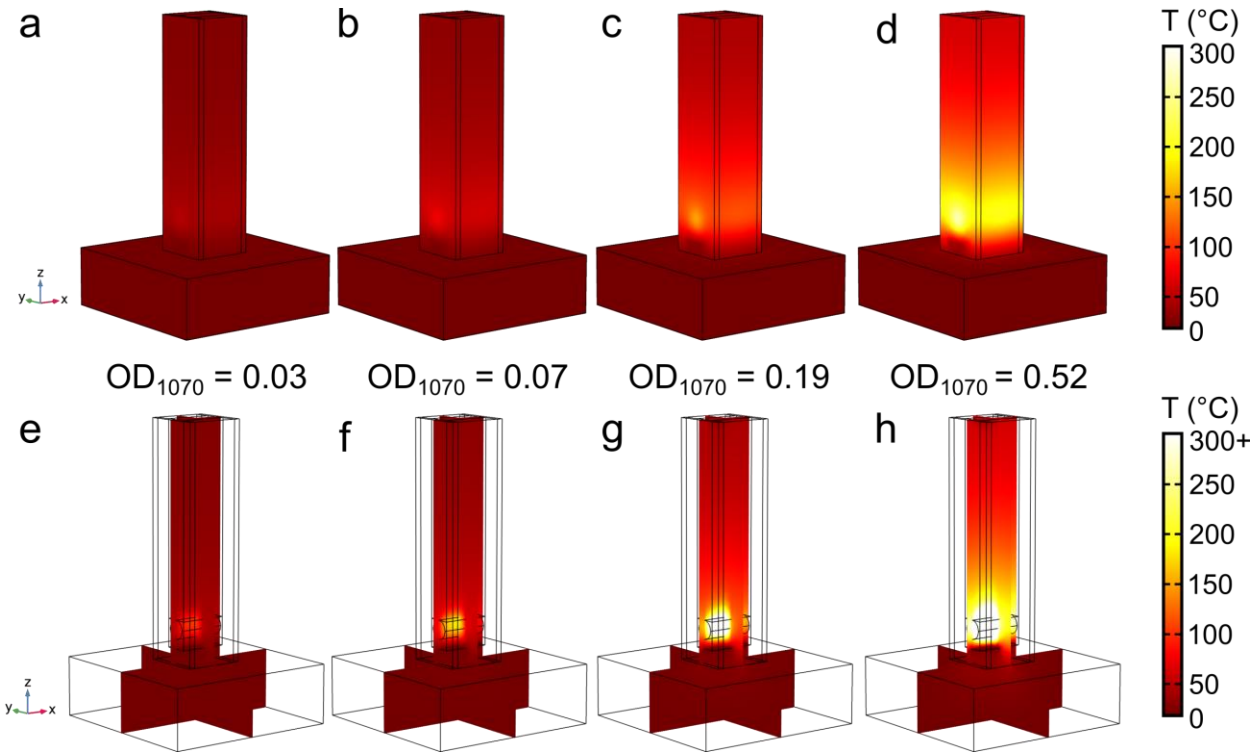

Figure 2.5. (a-d) Surface temperatures of quartz cuvettes with a range of Bi nanocrystal concentrations under 1070-nm irradiation, calculated via COMSOL modeling. (e-h) Cross-sectional temperature profiles of the cuvettes, calculated using COMSOL modeling.

2.3.2 *Photothermally-driven semiconductor nanowire growth using molecular precursors*

With clear evidence of nanocrystal-generated photothermal transduction via the unfocused, collimated irradiation of low-melting-point colloidal metal nanocrystals in dispersion, we then incorporated II-VI molecular precursors in an attempt to drive a solution-liquid-solid (SLS) nanowire growth reaction. Under irradiation, the bismuth nanocrystals rapidly heated the nanowire precursors, facilitating decomposition of the CdSe molecular precursors and successfully driving the solution-based growth of bismuth-seeded CdSe nanowires (Figure 2.6a-e).

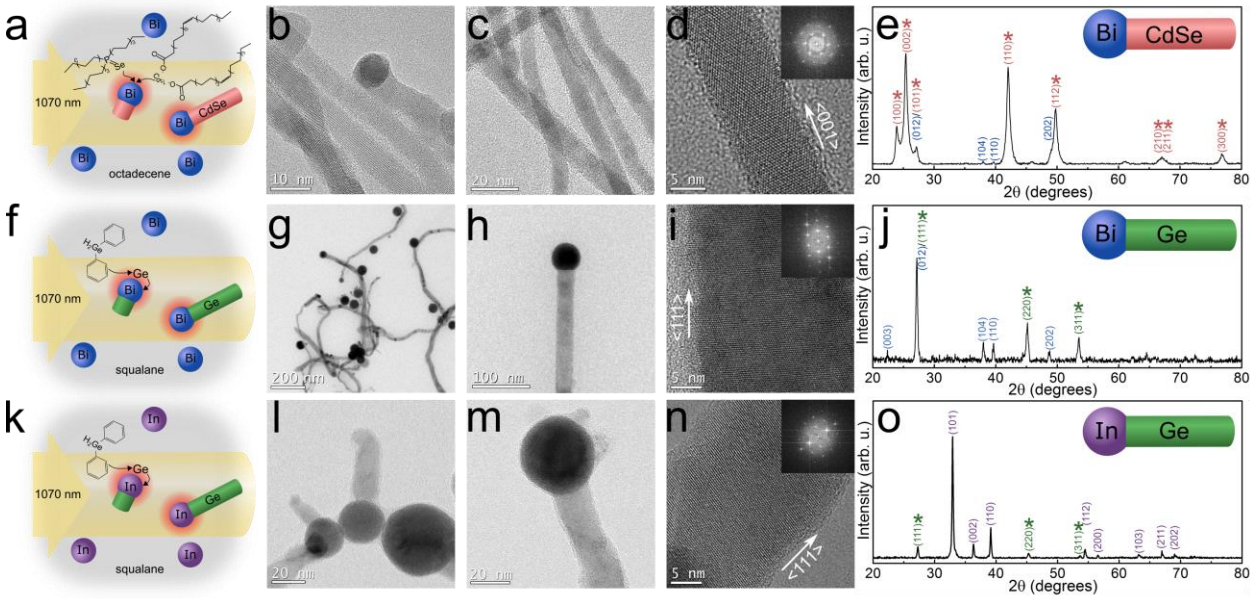

Figure 2.6. Examples of contact-free, solution-based, laser-driven nanowire growth of semiconductor nanowire systems with both ionic and covalent character, produced using different metal nanocrystal seeds under 1070-nm excitation on the benchtop. (a-e) Narrow-diameter, wurtzite-phase CdSe nanowires grown from bismuth nanocrystal seeds with cadmium oleate and trioctylphosphine selenide precursors, (f-j) diamond-cubic, bismuth-seeded germanium nanowires produced via photothermal decomposition of diphenylgermane, and (k-o) Indium-seeded germanium nanowires grown using indium nanocrystal seeds as photothermal heat sources.

Nanowire (highlighted with asterisks) and nanocrystal seed materials are indexed in each X-ray diffraction pattern.

Infrared thermal images and the associated temperature profiles (Figure 2.7b-d and Figure 2.8) show that nanowire growth solution temperatures under irradiation similarly increase with an increased concentration of bismuth nanocrystals, while the irradiation of CdSe molecular precursor solutions in the absence of bismuth nanocrystals (Figure 2.7a) resulted in limited temperature increases and no detectible precursor decomposition or nanowire growth.

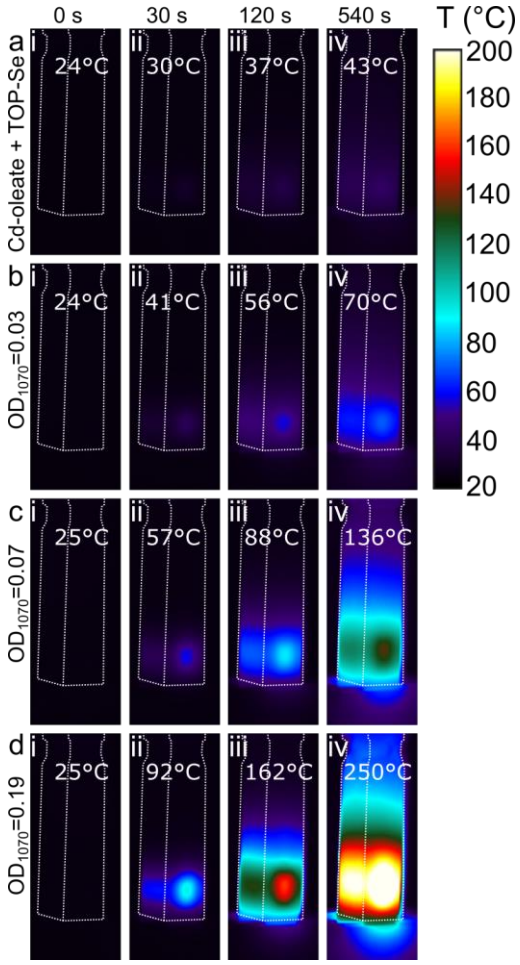

Figure 2.7. Thermal infrared images of (a) octadecene with CdSe precursors under irradiation (1070 nm, 15W) and (b-d) nanowire growth solutions with different nanocrystal concentrations

OD1070 = 0.03-0.19) under irradiation (1070 nm, 15 W), showing the evolution of the temperature profile in the cuvette.

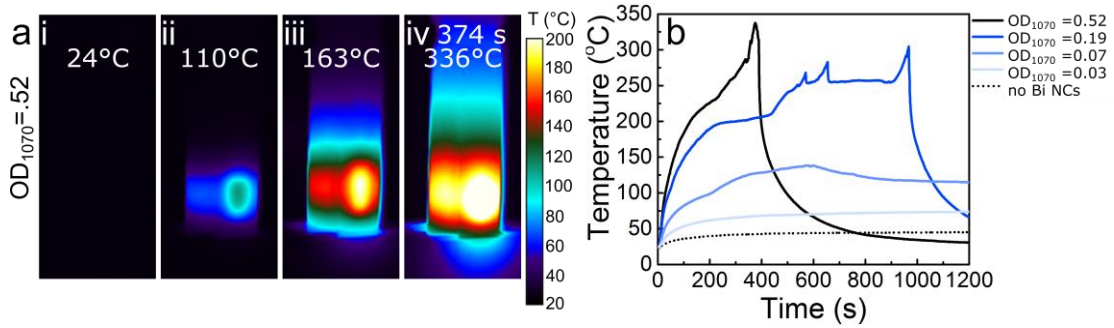

Figure 2.8. (a) Thermal infrared time series images of a nanowire precursor solution with bismuth nanocrystals at high concentrations (OD_{1070}=0.52) under irradiation (1070 nm, 15W), demonstrating the extremely high temperatures achieved by photothermal heating and (b) time-dependent temperature profiles for different bismuth nanocrystal concentrations (OD_{1070}=0.03-0.52) with CdSe precursors under irradiation (1070 nm, 15W).

Notably, typical nanocrystal-seeded, SLS-based CdSe nanowire growth processes require the use of a Schlenk line and reaction temperatures in the range of 230-350°C;[61,296] here, heat generated by photothermal transduction enabled the same high temperature process to be carried out in a standard quartz cuvette out on a benchtop without additional heating equipment. This is emphasized by the fact that the OD_{1070} = 0.07 cuvette surface only reached a maximum temperature of 136°C, but still resulted in the successful growth of CdSe nanowires. This observation confirms that the temperature at the nanocrystal-solvent interface is higher than the reactor chamber temperature.

In each of the experiments, the resulting nanowire product rapidly flocculated as soon as the laser was blocked. Bright-field TEM imaging (Figure 2.6b-d) clearly demonstrates that laser heating did not result in homogeneously nucleated CdSe byproducts upon decomposition. Rather, the metal seeds act as growth-directing agents to produce nanowires via a photothermally-driven

SLS growth mechanism. Compared to previous two-step, optically-driven II-IV nanowire growth processes,[295] the CdSe nanowire synthesis performed here was carried out in a single step. TEM images (Figure 2.6b-d) highlight the narrow nanowire diameters (7.3 ± 1.9 nm, Figure 2.9) achieved via this photothermally-driven process, while high-resolution TEM imaging (Figure 2.6d) shows that the CdSe nanowires exhibit a <001> growth direction, which is consistent with XRD measurements that show an increased intensity of the (002) reflection due to nanowire anisotropy (Figure 2.6e).

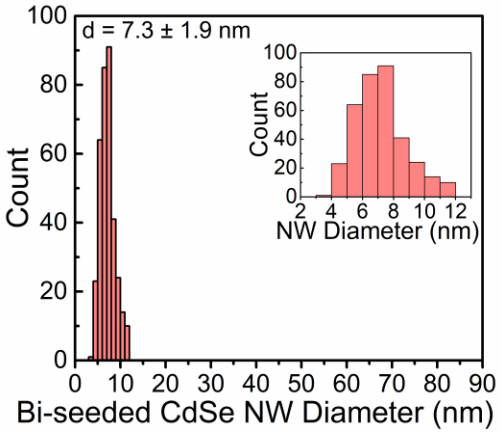

Figure 2.9. Distribution of Bi-seeded CdSe nanowires diameters synthesized by laser-driven growth.

While this represents a successful demonstration of solution-based, photothermally driven, seeded nanowire growth, the CdSe material system is highly ionic in character, and materials that are more covalent in character (such as Si and Ge) typically have higher crystallization barriers, and therefore typically require much higher temperatures (>300°C) for nanowire growth.[33,37,59,65,297,298] Consequently, in order to investigate the versatility and potential scope of the photothermally driven nanowire growth process, we also targeted the production of group-IV semiconductor nanowires, using the same bismuth nanocrystal seeds to drive the reaction. In this

scenario, colloidal bismuth nanocrystals under near-infrared irradiation once again act both as heat sources and as seeds for nanowire growth, this time driving the decomposition of diphenylgermane precursor to facilitate the optically driven SLS-growth of Ge nanowires (Figure 2.6f-j), without the need for a vacuum system, Schlenk line, or supercritical reactor system. Bright-field TEM images (Figure 2.6g-i) demonstrate the growth of crystalline Ge nanowires with diameters of 15.6 ± 7.8 nm (Figure 2.10) and a predominantly <111> growth direction, which is characteristic of high-temperature growth processes in the Ge material system.[299] While XRD (Figure 2.6f) clearly shows the presence of both crystalline Bi and Ge, the Bi-seeded Ge nanowires synthesized through contact-free photothermal heating were typically observed to have a tortuous morphology, likely due to the small volume of solution that was irradiated, and subsequent convection of nanowires into and out of the beam.

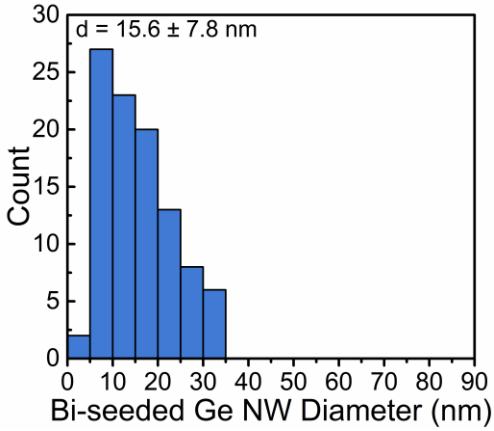

Figure 2.10. Distribution of Bi-seeded germanium nanowire diameters synthesized by laser-driven growth.

Since both of the above nanowire growth examples relied on the use of Bi nanocrystals as the local heat sources and nanowire growth-directing agents, we then switched to an indium (In) nanocrystal system to further demonstrate the versatility of the laser-driven, seeded nanowire

growth process. While indium has been used to grow germanium nanowires via vapor-liquid-solid (VLS) growth[300] and other semiconductor nanowires through modified SLS growth,[37] most of this work has exploited the low melting point of In to generate In droplets on a substrate from an evaporated In thin film. Here, we demonstrate the use of colloidal In nanocrystals (Figure 2.11) as photothermal heat transducers under incident near-infrared irradiation to decompose diphenylgermane in solution, once again enabling the laser-driven, seeded growth of germanium nanowires in a cuvette (Figure 2.6k-o).

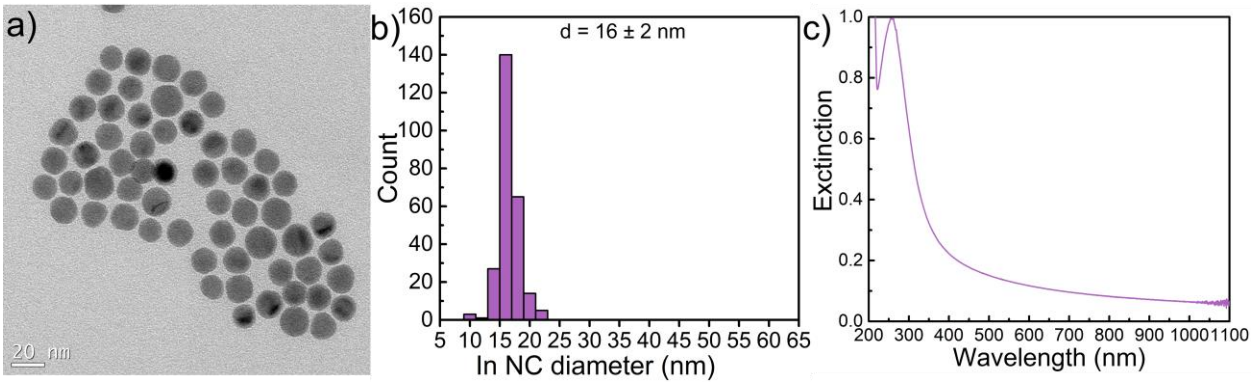

Figure 2.11. (a) TEM image of indium nanocrystals, (b) histogram of the indium NC diameter distribution, and (c) extinction spectrum of the indium nanocrystals used to synthesize In-seeded Ge nanowires.

The In-seeded Ge nanowires generated from this optically driven process typically had shorter lengths and wider diameters (Figure 2.6k-o, Figure 2.12) than the photothermally grown Bi-seeded Ge nanowires. These morphological differences could likely be attributed to the markedly lower melting point of In (156 °C) when compared to Bi (271 °C), which could result in the rapid coalescence of In nanoparticles upon irradiation, leading to larger seed particles and, thus, larger nanowire diameters, in addition to the differences in surface energies and contact angles for the two different nanocrystal seeds.

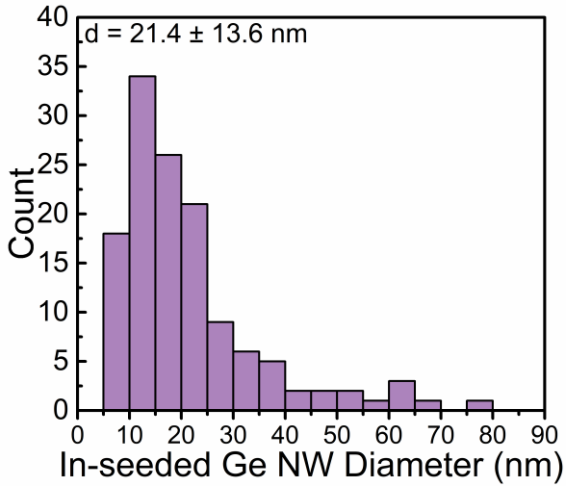

Figure 2.12. Distribution of In-seeded germanium nanowire diameters synthesized by laser-driven growth.

2.3.3 *Photothermally-driven nanowire growth using magic-sized clusters as precursors*

In order to create more compositionally complex semiconductor nanowires, such as doped semiconductor nanowires, using a single-source precursor could be advantageous. Strategies to incorporate dopants into semiconductor nanowires have traditionally taken the approach of balancing precursor decomposition kinetics and solubility in the metal-semiconductor alloy droplet. II-VI and III-V semiconductor nanowires provide an additional challenge because their synthesis inherently requires balanced reactivities of two precursors: a metallic-element precursor and a nonmetallic-element precursor. By using a single precursor, the challenge of balancing competing precursor decomposition kinetics can be simplified. Development of single-source semiconductor precursors has been widely sought-after, especially for II-VI and III-V nanocrystal syntheses.[301–304] However, the use of single-source precursors for compound semiconductor nanowire growth through VLS,[175,302] SLS,[301,305,306] and SFLS nanowire growth processes remains limited; notably the single-source precursors used to-date have only been developed for a host semiconductor and have not yet included dopants.

Here, we use photothermally-driven nanowire growth to rapidly test the potential of indium phosphide magic-sized clusters as a single-source precursor for bismuth-seeded indium phosphide nanowires. Although magic-sized clusters have been used extensively for nanocrystal syntheses, to our knowledge, the use of clusters as single-source precursors for semiconductor nanowires remains limited[305]. Most semiconductor nanowire syntheses—across both vapor- and solution-based syntheses—have primarily used molecular precursors. Moreover, by using magic-sized clusters as an alternative precursor for photothermally-grown indium phosphide nanowires; we limit the use of common phosphorus precursors, such as tris(trimethylsilyl)phosphine, which are extremely reactive and pyrophoric and pose a safety hazard.

The indium phosphide nanowires grown from magic-sized clusters have narrow diameters (Figure 2.13b-d) and are zincblende phase (Figure 2.13e) with a <111> growth direction, which is consistent with other SLS-grown indium phosphide nanowires.[33,291] The anisotropy of the nanowires is highlighted by the strong (111) reflection at 26.3° and the nearly nonexistent (200) reflection at 30.4°.

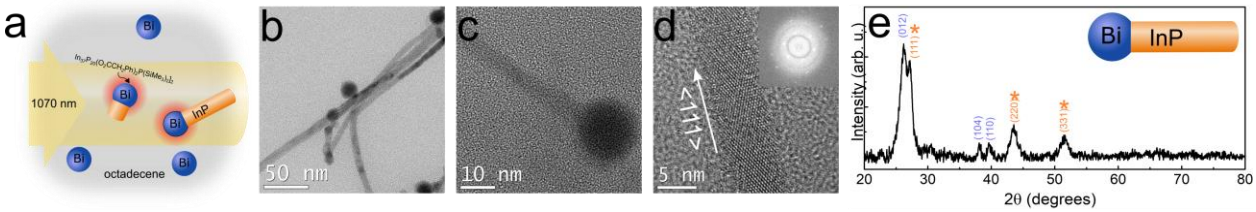

Figure 2.13. (a) Bismuth-seeded indium phosphide nanowires grown from a single source precursor through contact-free, solution-based, laser-driven synthesis on the benchtop under 1070-nm excitation. (b-d) TEM of narrow-diameter, InP nanowires grown from Bi nanocrystal seeds using indium phosphide magic sized clusters as a single-source precursor. (e) XRD of the zincblende Bi-seeded InP nanowires. Both nanowire (orange, highlighted with asterisks) and nanocrystal seed (blue) are indexed.

2.3.4 *Continuous, laser-driven solution-liquid-solid nanowire growth under flow*

All of these processes generated SLS-grown nanowires at "bulk" ambient temperatures via photothermal heating without the use of a Schlenk line, pressure vessel, insulation, or resistive heating. In comparison, global resistive heating of a SLS nanowire growth reactor system involves an isothermal process in which the reaction vessel and chemical components are at thermal equilibrium. In contrast, the high temperatures generated by contact-free, optical heating of the metal nanocrystals can rapidly drive nanowire growth without the need for high-temperature equipment. In addition to using a quartz cuvette as a reaction vessel, we have also used a simple NMR tube combined with an inexpensive, low-power, 808-nm diode (2 W) to grow Bi-seeded CdSe nanowires, demonstrating that the optically driven process can be carried out using a variety of powers and excitation wavelengths.

The versatility of this growth strategy naturally lends itself toward the integration of spectroscopic methods that could be used to study in situ nanowire growth dynamics. However, in all of the above nanowire growth demonstrations—using both quartz cuvettes and NMR tubes as reaction vessels—the nanowire growth solution inevitably developed convective patterns due to the size of the photothermal heating zone and variations in intensity across the Gaussian laser source. In order to realize the greater potential of this contact-free, colloidal nanocrystal-based semiconductor nanowire growth process, as a proof of principle, we demonstrate the photothermally driven growth of semiconductor nanowires using a continuous-flow reaction scheme to circumvent problems associated with free convection (Figure 2.14). We first constructed an optically interrogable reaction zone (Figure 2.14a), through which solutions of II-VI semiconductor precursors and colloidal nanocrystals can be injected simultaneously. Upon irradiation and while under flow, the nanocrystals once again rapidly generated heat to decompose

the precursor and seed nanowire growth (Figure 2.14e), eventually exiting the flow cell further downstream. Converting this non-contact, laser-driven nanowire growth method into a continuous flow process is a further step towards a low-cost, scalable system in which nanowire growth dynamics and various growth parameters can be rapidly scanned and spectroscopically probed to enable real-time feedback and optimization of material properties.

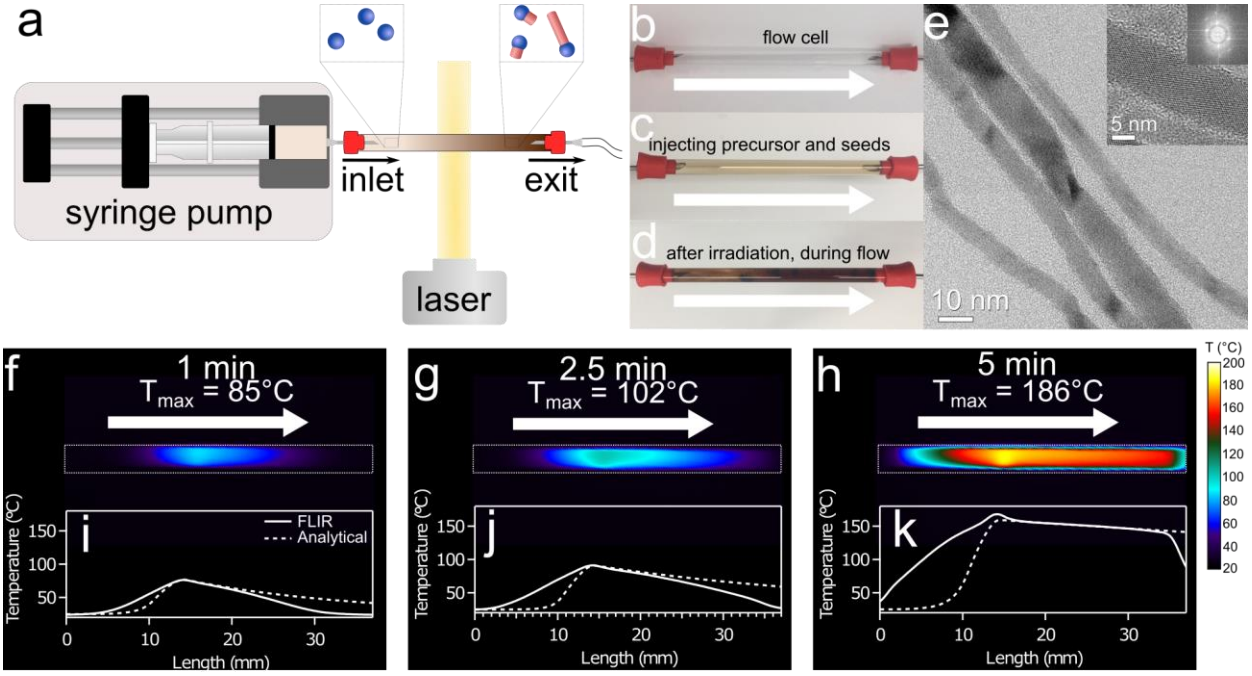

Figure 2.14. Demonstration of continuous, laser-driven nanowire growth under flow. (a) Flow cell schematic along with (b-d) associated images of the reaction zone (b) containing only octadecene, (c) during injection of Bi nanocrystal seeds (OD_{1070} = 0.07) and II-VI molecular precursors, and (d) after irradiation under flow. (e) Characteristic TEM images of the Bi-seeded CdSe nanowire product. (f-h) Snapshots from an infrared thermal imaging camera, showing temporal evolution of temperature profiles in the reaction zone of the flow cell after 1 minute, 2.5 minutes, and 5 minutes of 1070 nm irradiation under continuous flow (0.05 mL/min). Temperature labels correspond to the maximum temperature recorded in each image. (i-k) Measured (solid line) and calculated (dashed line) temperature line profiles throughout the flow cell at each time point.

To confirm the internal temperature of the flow cell during heating, we analytically calculated the temperature profile within the reactor volume during laser-driven nanowire growth under flow (Appendix A). We provide details of this derivation and model, which should be valid for a wide range of flow rates, in the Supporting Information. At low flow rates, the Peclet number is ~1, which means that heat transport via both thermal conduction and fluid flow are important and cannot be neglected. The observed axial diffusion of heat both upstream and downstream of the incident laser spot (Figure 2.14f-g) clearly reflects this effect. Figure 2.14i-k also shows the projected temperature distribution on the surface of the flow cell and the analytically calculated, radially averaged temperature. This analysis shows that there is very little radial temperature distribution, and, unlike with the cuvette, the infrared thermography images are within 1% of the internal temperatures, suggesting that the maximum temperature during growth in the flow cell was ~188°C, which is below the typical 230°C temperature used for bismuth-seeded CdSe nanowire synthesis. In addition, these results demonstrate that a flow cell geometry may be useful for future in situ spectroscopic experiments. We note that analytical temperature distributions of both a bismuth-seeded CdSe nanowire and a bismuth nanocrystal (Figure A.1) in an infinite bath do not demonstrate appreciable heating above ambient temperatures. Thus, it is possible that the decreased temperature requirement for nanowire synthesis could be due to local heating of the nanowire caused by exothermic precursor decomposition or hot-electron effects. To examine these possibilities, we heated colloidal bismuth nanocrystals in a cuvette and measured the surface temperatures with and without CdSe precursors (Figure 2.3d and Figure 2.7d). After 540 seconds, the surfaces of the cuvettes containing the irradiated nanocrystal solutions with CdSe precursors present were 96°C higher in temperature than cuvettes containing identical nanocrystal concentrations but no semiconductor precursors. This demonstrates additional heating associated

with the reaction of CdSe precursors, which may accelerate nanowire synthesis. Alternatively, the growth of nanowires may generate additional scattering effects that could boost the absorption of light.

Overall, we have demonstrated that we can rapidly generate heat in solution by irradiating colloidal, low-melting point nanocrystals such as bismuth and indium. This fast, contact-free heating process has been leveraged to drive precursor decomposition and metal-seeded SLS nanowire growth. Because these colloidal nanocrystals are dispersed in solution, rather than pinned to a substrate, they have the potential to locally superheat the solvent due to the large Young-Laplace interfacial surface pressure required to nucleate a bubble. As an example of this effect, it has been previously demonstrated that irradiation of a single gold nanocrystal in water can produce local temperatures greater than 300°C prior to bubble nucleation.[277] By utilizing metal nanocrystal photothermal transduction to generate heat in this system, the immediate environment near the nanocrystal surface likely reaches much higher temperatures than the bulk solvent, potentially enabling energy intensive chemical reactions to occur in local proximity to the irradiated nanocrystals, without the need to heat the entire bulk solvent or reactor volume. Consequently, the use of colloidal metal nanocrystals in solution to transduce light into thermal energy lifts the temperature and gas handling requirements of the reactor to a certain extent, possibly also capitalizing on collective heating effects,[14,26] and thus enables the use of a simple quartz cuvette or NMR tube on a benchtop as a reaction vessel. We have explored a range of metal/semiconductor combinations in this optically driven process to grow nanowires with both ionic and covalent character. In addition to using typical molecular semiconductor precursors, we utilize magic-sized clusters as a single-source precursor for SLS-grown nanowires.

Moreover, this laser-driven, colloidal reaction system is readily converted from a batch process—performed on a benchtop in a cuvette—to a low-cost, scalable continuous-flow process. This first demonstration of optically driven nanowire growth in a continuous-flow cell opens a range of new potential pathways to rapidly scan new nanowire chemistries as well as optimize nanowire growth conditions with real-time feedback through paired spectroscopies and scattering measurements. Furthermore, the ability to quickly reach high temperatures near the metal nanocrystal seed could potentially enable the nonequilibrium incorporation of semiconductor dopants during the nanowire growth process, rather than during an additional post-synthetic doping step.

2.4 CONCLUSIONS

We have demonstrated that the photothermal heating of metallic nanocrystals during continuous-wave NIR laser irradiation is capable of synthesizing semiconductor nanowires with both ionic and covalent character, in solution under continuous flow conditions. The photothermal transduction capabilities of metal nanocrystals were utilized to generate sufficient heat to facilitate solution-liquid-solid nanowire synthesis. Because the metal nanocrystals are dispersed freely in solution and are heated collectively, they have the potential to reach very high temperatures due to Young-Laplace interfacial surface pressures. With further optimization, this optically driven nanowire growth process could enable solution-based growth of systems that currently require alternative growth methods due to solvent boiling point limitations.

In addition, photothermal heating makes rapid changes in temperature possible, which could facilitate the production of complex, heterostructured nanowires or rational dopant incorporation via solution-based methods. By using indium phosphide magic-sized clusters as a

single-source precursor for SLS-grown nanowires, we extend the possible routes for dopant incorporation into semiconductor nanowires.

Moreover, because this photothermally-driven process can be performed on a benchtop in virtually any chemically resistive, optically interrogable reaction vessel, it could enable the facile integration of *in situ* scattering and spectroscopic techniques for the interrogation of solution-based nanowire growth in a variety of different material systems. In addition, the development of optically driven nanowire growth under continuous flow could further enable high-throughput screening and optimization of solution-based nanowire systems. This growth strategy will also likely open a pathway to the study of single-particle nanowire growth dynamics in solution through the implementation of an optical trap and orthogonal scattering or spectroscopic measurements.

Chapter 3. STUDYING THE DYNAMICS OF LASER-DRIVEN SOLUTION-LIQUID-SOLID SEMICONDUCTOR NANOWIRE GROWTH USING ULTRA-SMALL-ANGLE X-RAY SCATTERING

The work presented in this chapter is the result of a highly collaborative project between the Holmberg lab, the Pozzo lab (UW Chemical Engineering), and the Pauzauskie lab (UW Materials Science and Engineering). Dr. Yi-Ting Lee, and Dr. Matthew Crane aided with data collection at the Advanced Photon Source; Dr. Yi-Ting Lee, Dr. David Li, and Professor Lilo Pozzo provided invaluable expertise required for the analysis of ultra-small-angle X-ray scattering data.

3.1 INTRODUCTION

Developments in the solution-phase synthesis of inorganic nanomaterials over the past few decades have resulted in remarkable control over material properties through the careful tuning of nanomaterial size,[307–310] shape,[298,195,311,312] composition,[193,308,313–316] and surface chemistry.[78,198,317,318] In many cases, information related to the dynamics of nanostructure growth has been critical in order to identify reaction parameters that can be used to rationally engineer syntheses and achieve desired properties.[44,86,101,103,316,319] In all cases, the combination of reaction timescales and sampling rate frequencies dictate and limit which methods can provide useful *in situ* information about dynamic processes. For example, many semiconductor quantum dot growth processes occur at a sufficiently slow rate to allow for frequent aliquot collection to track nanocrystal growth via periodic absorption and photoluminescence measurements.[320] However, some synthetic methods are not conducive for aliquot extraction and thus require inventive methods to study growth dynamics.

Semiconductor nanowires are a particularly interesting class of nanomaterials due to their unique optical,[4–6] electronic,[1–3] and mechanical properties.[7–9] These characteristics have been leveraged for numerous applications including, sensors,[12,38,49,114–116] energy conversion,[19,139,165,321] and energy storage,[20–25] to name a few. Metal-seeded semiconductor nanowire growth is a powerful method for the production of nanowires with well-defined dimensions and compositions through both vapor-based processes such as vapor-liquid-solid (VLS) nanowire growth as well as through solvent-based processes such as the solution-liquid-solid (SLS) and supercritical-fluid-liquid-solid (SFLS) growth methods. Much of the current knowledge we have about the mechanism of metal-seeded semiconductor nanowire growth comes from *in situ* experiments studying vapor-phase nanowire growth. For example, *in situ* TEM experiments have clearly demonstrated how thermodynamic growth conditions and reaction parameters such as precursor partial pressure, nanoparticle diameter, and seed composition, among other experimental parameters, can control nanowire nucleation kinetics, growth direction, morphology, phase selection, and defect incorporation.[32,101,150,151,158,322–326] Many *in situ* TEM experiments highlight the importance of fluid-seed-nanowire interface dynamics (at the triple phase boundary) and have provided context that has since enabled the production of anisotropic nanostructures with improved control.[89,101,103,327,328]

In an additional example, dark-field scattering was also used as a tool to study nanowire growth dynamics by irradiating a gold-nanocrystal-decorated substrate while simultaneously introducing a vapor-phase semiconductor precursor into a chemical vapor deposition chamber.[153] In this case, the incident laser acted both as a trigger to initiate nanowire growth from the substrate as well as a light source to study nanowire growth dynamics by tracking changes in the optical scattering signal. In general, most studies of nanowire growth dynamics have been limited to

substrate-based, vapor-phase growth, with this particular experiment requiring the construction of a custom-built, optically interrogable chemical vapor deposition chamber. While solution-based nanowire growth is often considered a direct analogue to the VLS growth process, *in situ* methods to study solution-based nanowire growth dynamics remain somewhat limited.[164,329]

More recently, microfluidic SLS-based growth has provided a route to study nanowire growth dynamics and kinetics in solution.[330] In this microfluidic demonstration, semiconductor precursors could be supplied and mixed in the solution phase, prior to entering a heated reaction zone, which contained a substrate covered with a thin film of metallic bismuth, designed to melt and de-wet into seed droplets at elevated temperatures. Nonetheless, this example was once again limited to investigations of nanowire growth from a substrate, rather than the dynamics of a scalable, colloidal-nanocrystal-based growth process.

Here, we leverage our recently developed photothermally-driven solution-liquid-solid nanowire growth process, which can be performed in any optically accessible, chemically inert container, along with the unique capabilities of ultra-small-angle X-ray scattering (USAXS) to study the solution-based growth dynamics of bismuth-nanocrystal-seeded cadmium selenide nanowires in dispersion. In this preliminary study, we investigate the effects of bismuth nanocrystal concentration and laser power on nanowire growth rate as well as demonstrate the ability to activate stepwise nanowire growth on demand, in solution, simply by turning the incident laser on and off.

3.2 EXPERIMENTAL DETAILS

3.2.1 *Materials*

Bismuth (III) chloride ($BiCl_3$, 99.99% trace metals basis), cadmium oxide (CdO, ≥99.9% trace metals basis), ethanol (anhydrous, ≤0.005% water), indium (III) chloride (99.999% trace metals basis), isopropanol (anhydrous, 99.5%), molecular sieves (3 Å), *n*-butyllithium (1.3 M in *n*-heptane), 1-octadecene (ODE, 90%), oleylamine (90%), oleic acid (degassed, 90%), sodium bis(trimethylsilyl)amide (1.0 M solution in tetrahydrofuran), squalane (96%), Super-Hydride® solution (1.0 M lithium triethylborohydride in tetrahydrofuran), selenium (Se, <5 mm particle size, ≥99.999% trace metals basis), tetrahydrofuran (THF, anhydrous, ≥99.9%), toluene (anhydrous, 99.8%), and trioctylphosphine (TOP, 97%) were purchased from Sigma-Aldrich. Poly(1-hexadecene-*co*-1-vinylpyrrolidinone) (PHD-*co*-PVP) was provided by Ashland under the trade name Ganex™ V-216. Toluene (Certified ACS, 99.8%) was purchased from Fisher. Ethanol (200 proof) was purchased from Decon Laboratories.

3.2.2 *Bismuth nanocrystal synthesis*

Bismuth nanocrystals were synthesized based on the protocol outlined by Wang, *et al*.[61] A 25 wt% solution of PHD-*co*-PVP in 1-octadecene was dried over molecular sieves for one week. $BiCl_3$ (2.6×10^{-2} mmol) was mixed with THF (570 μL) in a three-neck, round bottom flask under nitrogen at 800 RPM on a stir plate for thirty minutes. The solution of PHD-*co*-PVP in octadecene (6.1 mL) was then added to the $BiCl_3$containing flask under continuous mixing at 900 RPM. The flask was cycled between nitrogen and vacuum three times. Sodium bis(trimethylsilyl)amide (825 μL) was injected, and the flask was stirred until a dark orange-brown color was observed (~10 minutes,

1100 RPM). The solution was then heated to 200°C for 17 hours, cooled, and then transferred into a nitrogen-filled glove box for storage. Bismuth nanocrystals were handled under nitrogen for cleaning. Nanocrystals were washed five times using a 1:4 ratio of anhydrous hexanes:ethanol and centrifugation (6800 RCF for 10 minutes) to remove excess PHD-*co*-PVP prior to use for nanowire growth. The resulting bismuth nanocrystal stock solution was 8×10^{-3} mol elemental Bi/L.

3.2.3 *Preparation of cadmium oleate*

Using standard Schlenk line techniques, 0.15 M cadmium oleate in 1-octadecene (ODE) was prepared by combining 210 mg CdO, 2.7 g oleic acid and 5.2 g ODE in a flask. The mixture was blanketed with nitrogen and stirred at 800 RPM, heated to 110°C, and placed under vacuum for 30 minutes. The mixture was cooled to room temperature under nitrogen and transferred to a glove box, whereupon 1 mL of trioctylphosphine (TOP) was added and mixed for 15 minutes.

3.2.4 *Preparation of trioctylphosphine-selenide*

A 1.0 M stock solution of TOP:Se was prepared in a nitrogen-filled glove box by stirring 238 mg of Se in 5 mL of TOP for 16 hours, until dissolved.

3.2.5 *Ultra-small-angle X-ray scattering measurements of photothermal nanowire growth*

Nanowire precursor growth solutions, containing bismuth nanocrystals, cadmium oleate, TOP-Se, and octadecene, were mixed at the desired proportion and loaded into an NMR tube (ASTM E438 Type 1 Class B glass, outer diameter: 5 mm, inner diameter 4.62 mm) under a nitrogen atmosphere.

The top of the NMR tube was covered with Teflon tape, capped, and covered with Parafilm to prevent oxidation of nanocrystals. Nanowire precursor growth solutions for each sample are outlined in Table B.1. The NMR tube with the growth solution was transferred out of the nitrogen atmosphere and placed into a holder with a fixed distance between the 808 nm laser (MDL-III-808 IR diode laser) and the NMR tube. The nanowire growth sample was then irradiated at a range of laser powers outlined in Table B.1. USAXS experiments were performed simultaneously during irradiation, using the USAXS instrument in the standard Bonse-Hart configuration at beamline 9-ID-C at the Advanced Photon Source, Argonne National Laboratory, using an X-ray beam energy of 21 keV.[331] Samples were irradiated for a total of 3 minutes at each USAXS time point.

The recorded USAXS scattering data was reduced to an absolute scale and de-smeared using the Indra module of the SAS software package.[332,333] The de-smeared, background-subtracted scattering data of the initial and final time points were fit with a sum of two models to describe the complexity of the system. SasView 4.2.2. was used to fit the initial and final time points as well as to calculate the invariant. To fit the initial time point, prior to irradiation, we used a model of a sphere with a fractal component to describe the bismuth nanocrystals. To fit the final time point after continuous irradiation, we used a model consisting of cylinders with a fractal component to account for the dominant scattering of the cadmium selenide nanowires. To calculate the invariant, assuming that both the nanocrystals and nanowires have smooth interfaces, a Porod extrapolation with a fixed power-law exponent of -4 was used at high q and a Guinier extrapolation was used at low q.

3.3 RESULTS AND DISCUSSION

3.3.1 *In situ characterization of SLS nanowire growth with USAXS*

USAXS is a uniquely fitting *in situ* characterization technique to track nanowire growth because it can probe the relevant characteristic length scales of both isotropic nanocrystal seeds as well as the highly anisotropic semiconductor nanowires. The experimental setup used to track the photothermally-driven SLS nanowire growth process in solution is shown in Figure 3.1a, in which both the 808-nm laser and the X-rays are orthogonally aligned to irradiate and probe the same sample volume within the NMR tube. Figure 3.1b shows characteristic time-dependent scattering data of the nanowire precursor solution—colloidal bismuth nanoparticles and molecular cadmium selenide precursors (Cd-oleate and TOP-Se)—under irradiation. To note, the incident X-rays did not promote nanowire growth in the absence of laser irradiation; nanowire growth only occurred when the nanocrystals and CdSe precursors were irradiated by the 808-nm laser.

A representative TEM image of the bismuth nanocrystals used in this study is shown in Figure 3.1c. When irradiated, the colloidal bismuth nanocrystals photothermally transduce the incident light into heat, facilitating decomposition of both Cd-oleate and TOP-Se, whereupon the semiconductor atoms alloy with the nanocrystal, nucleating anisotropic growth of CdSe nanowires once the alloy droplet reaches saturation. A representative TEM image of the resulting bismuth-seeded CdSe nanowires is shown in Figure 3.1d.

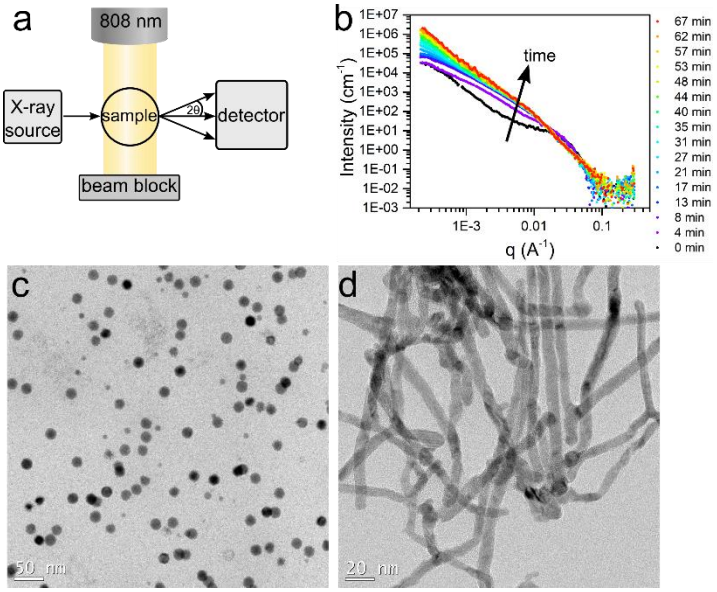

Figure 3.1. (a) A top-view schematic of the experimental setup used to irradiate the nanowire growth solution and simultaneously collect scattering profiles *in situ*, where the sample in an NMR tube is irradiated by an 808-nm laser, which drives the nanowire growth process; the X-ray source hits the same sample volume orthogonally, and the detector behind the sample collects the resulting scattering profile. (b) Time-dependent USAXS profiles of the nanowire growth solution (Bi NC OD_{808}=0.35) irradiated with an incident power of 2 W, where the black curve corresponds to the scattering profile of bismuth nanocrystals dispersed in CdSe precursors and solvent prior to irradiation, and the red curve corresponds to the growth solution after 67 minutes of irradiation. (c) A representative TEM image of the bismuth nanocrystal seeds and (d) a representative TEM image of CdSe nanowires produced using the laser-driven SLS nanowire growth process.

To fit the USAXS curve of the bismuth nanocrystals at the initial time point, we used a two-component model, using a combination of spheres[334] and a fractal component[335] (Figure 3.3c, black line), where the 1D scattering intensity of a sphere was calculated as

$$I(q) = \frac{s}{V}\left[3V(\Delta\rho)\cdot\frac{\sin(qr)-qr\,\cos(qr)}{(qr)^3}\right]^2 + b \qquad (3.1)$$

where s is a volume fraction, V is the volume of the particle (bismuth nanocrystals), r is the radius of the spherical bismuth particle, b is the background level, and $\Delta\rho$ is the difference in scattering

length densities between the scatterer of interest (bismuth nanocrystals) and the precursors and solvent. The model used to calculate the scattering from fractal-like aggregates of spheres is

$$I_0(q) = \phi V_0 \left(\rho_{Bi} - \rho_{precursors}\right)^2 P_0(q) S_0(q) + b \tag{3.2}$$

where ϕ is the volume fraction of the building block particles V_0 is the volume of a single bismuth nanocrystal building block. $P_0(q)$ and $S_0(q)$ are defined as:

$$P_0(q) = \frac{3(\sin q - q\cos q)}{q^3}(qR_0)^2 \tag{3.3}$$

$$V_0 = \frac{4}{3}\pi R_0^3 \tag{3.4}$$

$$S_0(q) == 1 + \frac{D_f\,\Gamma(D_f-1)}{[1+1/(q\xi)^2]^{(D_f-1)/2}} \frac{\sin[(D_f-1)\tan^{-1}(q\xi)]}{(qR_0)^{D_f}} \tag{3.5}$$

where R_0 is the radius of the building block particle, ξ is the correlation length representing the aggregate size of particles, and D_f is the fractal dimension. Again, these particles act as both photothermal transducers and as seeds to facilitate anisotropic nanowire growth. Based on the USAXS fit, the bismuth nanocrystals have an average diameter of 9.6 ± 5 nm (Figure 3.3c). Both the fractal dimension (2.4) in the low-q range (Figure 3.3c) as well as the radius of the fractal component extracted from the model fit (15.8 ± 7 nm) suggest that the bismuth nanoparticles are partially aggregated prior to the start of the reaction.

The increased intensity of the USAXS profiles (Figure 3.1b, Figure 3.3a) throughout the mid- and low-q ranges as a function of time is indicative of a reaction occurring as the growth solution was continuously irradiated; in addition, the scattering profiles suggest that larger, emergent structures were formed under these experimental conditions, consistent with nanowire growth. To fit the USAXS profiles of the cadmium selenide nanowires at the final time point, we

used a fractal model[335] to calculate the scattering from fractal-like aggregates of spheres, defined as:

$$I_f(q) = \phi V_f \left(\rho_{CdSe} - \rho_{precursrs}\right)^2 P_f(q) S_f(q) + b \quad (3.6)$$

where ϕ is the volume fraction of the cadmium selenide building block particles and $P_f(q)$ and $S_f(q)$ are defined as:

$$P_f(q) = \frac{3(\sin q - q\cos q)}{q^3}(qR_f)^2 \quad (3.7)$$

$$V_f = \pi\frac{4}{3}\pi R_f^3 \quad (3.8)$$

$$S_f(q) = 1 + \frac{D_{f,f}\,\Gamma(D_{f,f}-1)}{\left[1+1/(q\xi_f)^2\right]^{(D_{f,f}-1)/2}} \frac{\sin\left[(D_{f,f}-1)\tan^{-1}(q\xi_f)\right]}{(qR_f)^{D_{f,f}}} \quad (3.9)$$

where V_f is the volume of a single cadmium selenide building block of radius R_f, ξ_f is the correlation length representing the aggregate size of nanowires, and $D_{f,f}$ is the fractal dimension of the nanowire network. Although this fractal model is not based on an aggregate of cylinders, the nanowires can be considered as extended chains of spherical particles. At low q values, this assumption is reasonable because the scattering in this region provides more information about the larger, emergent network and is not sensitive to the shape of the building block. In addition, because the nanowire diameter is dependent on the nanocrystal seed diameter, the radius of the nanowires at the final time point, R_f, was assumed to be approximately equal to the radius of the initial nanocrystal radius (R_0, 5 nm); TEM of the representative nanowires (Figure 3.2d) validates this approximation.

The change in the fractal dimension for the low-q region ($1\times10^{-4} \leq q \leq 0.01$) from 2.4 at the initial time point (Figure 3.3c), to 2.7 after 67 minutes (Figure 3.3b), indicates the formation of more densely packed aggregates over time. Because the nanowires are seeded by colloidal

nanocrystals, the nanowires grow in various orientations in solution, resulting in an emergent structure that is more similar to a fractal (Figure 3.1b, Figure 3.1d, Figure 3.3a) than singular or co-aligned nanowires. Although the bismuth nanocrystal seeds may contribute to the scattering profile in the final time point, here we assume that the scattering contribution from the CdSe wires is much greater than the contribution from the bismuth nanocrystals due to the high ratio of cadmium selenide precursors to bismuth nanocrystals (Table B.1) and the lengths observed in post-growth TEM images Figure 3.1d. A simple fractal model (Figure 3.3b, black line) was sufficient to fit the final time point at low q; due to the inherent complexity and polydispersity of the sample, models containing more detail were not implemented.

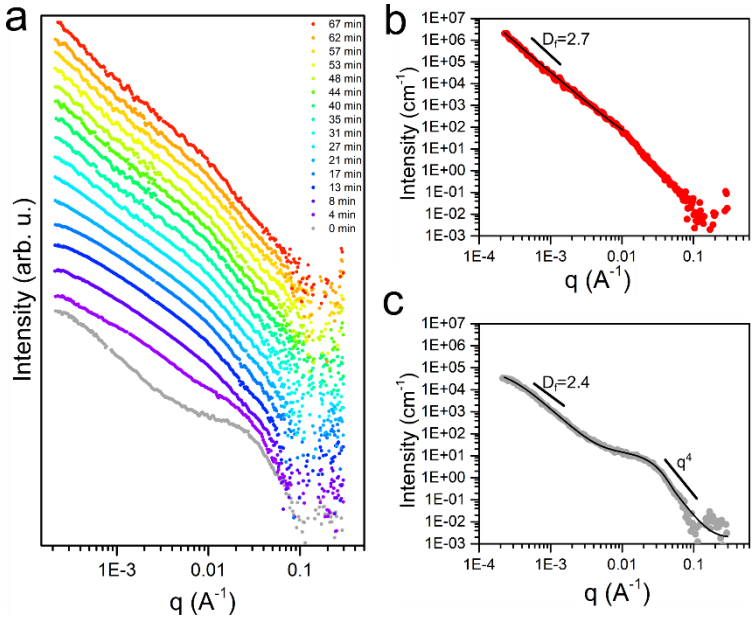

Figure 3.3. (a) Y-stacked scattering profiles of a CdSe nanowire growth solution (OD_{808}=0.35) irradiated with 2 W over 67 minutes, with the (b) model fit (black line) for the final time point for the low- to mid-q range, using a fractal model and the (c) model fit (black line) for the initial time point, using a sphere model with a fractal component to account for partial aggregation.

3.3.2 *Controlling nanowire growth rate through experimental parameters*

Although a fit was ascribed to both the initial and final time points for the nanowire growth process, modeling this system with geometric form-factor models is particularly difficult due to the combination of nanocrystal and nanowire polydispersity, as well as the larger fractals formed by both materials. Instead, we use the scattering invariant as a model-independent method to evaluate how the total volume of scattering particles changes over time. The scattering invariant (Q^*) is defined as:[336]

$$Q^* = \int_0^\infty q^2 I(q) dq \tag{3.10}$$

the integral of the square of the wavevector transfer multiplied by the scattering cross section of the full q range from zero to infinity. To calculate the invariant from zero to infinity, data in the low-q region was extrapolated with a Guinier fit and data in the high-q region was extrapolated with a power law fit, with a fixed power-law exponent of -4, which is the expected Porod scaling for particles with smooth interfaces.

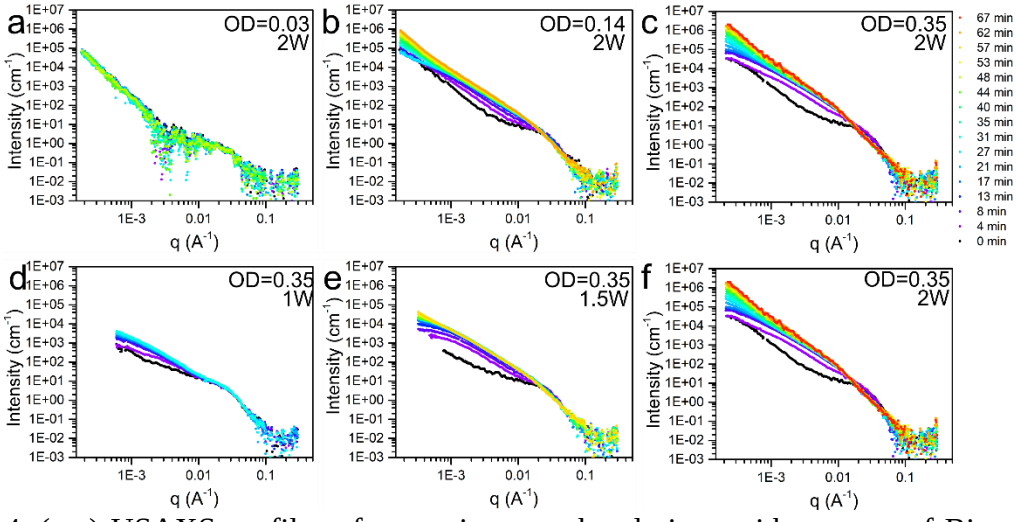

Figure 3.4. (a-c) USAXS profiles of nanowire growth solutions with a range of Bi nanocrystal concentrations, denoted by the optical density at 808 nm, (a) OD=0.03 (b) OD=0.14 (c) OD=0.35,

under continuous 808-nm irradiation at a an incident power of 2 W. (d-f) USAXS profiles of nanowire growth solutions with a constant Bi nanocrystal concentration (OD=0.35) under continuous irradiation at various powers: (d)1 W (e)1.5 W (f) 2 W.

The invariant was calculated from the USAXS profiles in Figure 3.4 and is shown in Figure 3.5a and Figure 3.5b, clearly demonstrating that the change in invariant is dependent on bismuth nanocrystal concentration (Figure 3.4a-c, Figure 3.5a) as well as the laser power used to irradiate the nanowire growth solution (Figure 3.4d-f, Figure 3.5b). From the invariant, the total volume fraction of cadmium selenide that formed during the reaction that contributes to additional scattering was calculated. The invariant and cadmium selenide volume fraction are related through the following equation:

$$\phi = \frac{1+\sqrt{1-4\frac{Q^*}{2\pi^2(\Delta\rho)^2}}}{2} \tag{3.11}$$

where ϕ is the volume fraction, Q* is the invariant, and Δρ is the scattering length density contrast, which is defined as:

$$\Delta\rho = \rho_s - \rho_0 \tag{3.12}$$

where ρ_s is the scattering length density of the scattering material of interest and ρ_0 is the scattering length density of the solvent and the precursors. The scattering length density is 4.2×10^{-5}, 6.2×10^{-5}, 8.4×10^{-6}, and 7.4×10^{-6} $Å^{-2}$ for CdSe, bismuth, CdSe precursors, and solvents, respectively. Because the change in scattering length density contrast is relatively small (approximately 6%) between nanowires dispersed in precursor and nanowires dispersed in neat solvent, we assume that the scattering length density contrast is roughly constant duration irradiation. From the change in volume fraction, assuming an average nanowire diameter of 10 nm, we calculated the average nanowire length as a function of time (Figure 1.1, Figure 3.5,

Appendix B), representing one of the first *in situ* measurements of colloidal, solution-based, laser-driven nanowire growth.

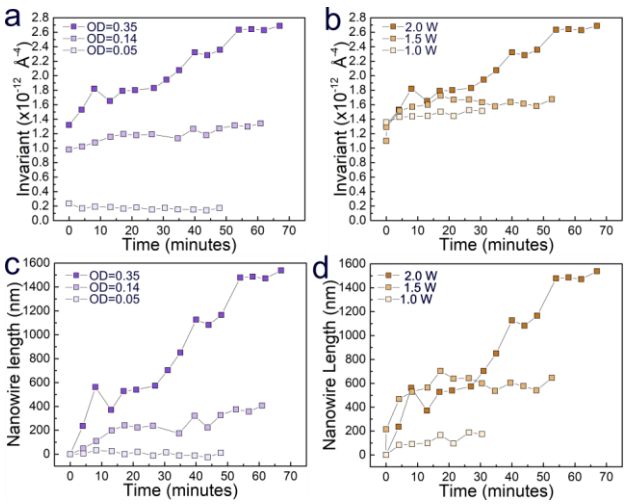

Figure 3.5. (a, b) Scattering invariant and (c,d) resultant average nanowire length calculated from USAXS profiles as a function of time, demonstrating (a, c) a dependence on bismuth nanocrystal concentration, dictated by the optical density at 808 nm (Bi NC OD_{808} = 0.05, 0.14, 0.35), at a constant irradiance and (b, d) a dependence on the irradiance (1 W, 1.5 W, and 2 W), with a constant Bi nanocrystal concentration.

For these calculations, the bismuth nanocrystals were assumed to coalesce during the heating/alloying process, resulting in an overall decreased number density of nanocrystals, which is a typical process for seeded nanowire growth, where the liquid alloy droplets can coalesce freely.[104,337–339] Consequently, for metal-seeded semiconductor nanowire growth, in which the nanowire is grown from a liquid-phase alloy droplet, even an initially monodisperse metal nanocrystal sample results in a log-normal distribution of nanowire diameters, which clearly impacts the average growth rate determined from the invariant. As an initial approximation, we assumed a final average seed diameter of 30 nm, which is a reasonable estimate given the inevitable log-normal coalescence of the initial 10-nm-diameter bismuth nanocrystals. Applying

a simple linear fit to the data in Figure 3.4 resulted in average growth rates of 20 nm/min and 10 nm/min, respectively, for samples with bismuth nanocrystal optical densities of 0.35 and 0.14, irradiated with 2 W of power. Growth solutions with a constant bismuth nanocrystal optical density of 0.35, but with incident powers of 1.5 W and 1 W resulted in measured growth rates of 11 nm/min and 6nm/min, respectively. The nanowire growth rates represented in Figure 3.5c and Figure 3.5d are in agreement with previous reports SLS-grown CdSe nanowires, with growth rates ranging from 11 nm/min to 46.6 nm/min.[330]

Upon irradiation, bismuth nanocrystals generate heat through a combination of photothermal transduction and collective heating effects;[340] however, at the lowest bismuth nanocrystal concentration investigated (Bi NC OD_{808} = 0.05), no measurable nanowire growth was observed. In this regime, the nanocrystals may be too dilute to produce enough heat to drive nanowire growth. As the nanocrystal number density increases, the number of photothermal transduction agents also increases, with the collective heating effect resulting in an overall temperature increase of the bulk fluid, as well as increased nanowire growth rates and longer nanowire lengths (Figure 3.5a and Figure 3.5c). In addition, we observe even the lowest incident power (1W) results in nanowire growth (Figure 3.5d, 1W), though at a much slower rate compared to the two higher incident powers (1.5 W and 2W). Although our previous demonstrations of laser-driven SLS nanowire growth have typically used higher powers at near-infrared wavelengths, here we demonstrate that low-power laser diodes are capable of driving nanowire growth.

3.3.3 *On demand, step-wise growth of semiconductor nanowires in solution*

To demonstrate the ability to rapidly start and stop photothermally-driven SLS nanowire growth, which could lead to improved synthetic control as well as open up additional possibilities to study

colloidal semiconductor nanowire growth, we subjected the nanowire growth solution (Figure 3.6) to controlled periodic intervals of incident radiation. The resultant USAXS profiles are shown in Figure 3.6a; the red curves correspond to profiles collected when the sample was being irradiated, while the blue curves correspond to profiles collected during periods when the sample was not being irradiated. In Figure 3.6a, all of the blue curves (except for the initial and final time points) are masked by the preceding red curve, which is consistent with the majority of nanowire growth occurring when the laser is turned on, with minimal changes occurring during the intervening periods. To more clearly demonstrate on-demand, pulsed nanowire growth through this solution-based, laser-driven process, the calculated nanowire length is shown in Figure 3.6b. Nanowire growth clearly occurs primarily during periods of irradiation (red highlight bars), with little change in average nanowire length during periods with no incident irradiation (white regions). The small increases in nanowire length observed after the incident laser was turned off each time can likely be attributed to latent heat that facilitates precursor decomposition, diffusion, and nanowire growth; however, this latent heat contributes to only a small fraction of the overall nanowire growth process.

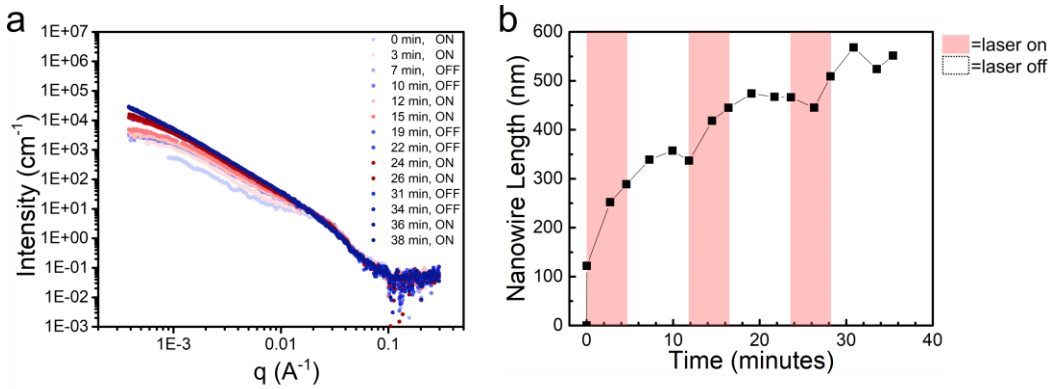

Figure 3.6. On-demand, step-growth of CdSe nanowires achieved by intermittently irradiating the nanowire growth solution. (a) Scattering profiles of a nanowire growth solution (Bi NC OD_{808}=0.35) under 808-nm irradiation (2 W) as a function of time. Blue profiles indicate that the

laser is off; red profiles indicate that the laser is on. (b) Change in average nanowire length as a function of time, demonstrating on-demand, pulsed CdSe nanowire growth via *in situ* characterization.

3.4 CONCLUSIONS

In summary, we have demonstrated characterization of solution-based, laser-driven, colloidal bismuth nanocrystal-seeded cadmium selenide nanowire growth via USAXS. To do this, we leveraged our recently developed laser-driven SLS nanowire growth process, which can be performed on a benchtop in virtually any chemically resistive, optically interrogable reaction vessel. Changes in nanowire length over time were calculated from the scattering invariant of USAXS profiles and the associated change in volume fraction. USAXS profiles and the associated changes in volume fraction enabled us to calculate changes in average nanowire length over time, with observations carried out under different reaction parameters demonstrating that laser-driven nanowire growth is dependent on both the bismuth nanocrystal number density as well as the incident power.

Although this is a first demonstration of *in situ* monitoring of laser-driven solution-based semiconductor nanowire growth, improving sample monodispersity would greatly enhance our ability to evaluate nanowire growth rates through both model fits and the invariant. In addition, because the photothermally-driven process is dependent on light absorption from the metal nanocrystal seed, exploring the effect of different bismuth nanocrystal sizes on nanowire growth rate could provide further insight into the photothermally-driven semiconductor nanowire process. Similarly, using alternative seeds, such as plasmonic nanocrystals with the incident radiation tuned to the nanoparticle resonant frequency could lead to interesting effects on semiconductor nanowire

growth rates. While bismuth-seeded cadmium selenide nanowire growth dynamics were monitored in this study, this process and characterization could be extended to understand the growth dynamics of other material systems that can be grown through photothermal processes, including II-VI, III-V and group-IV semiconductor nanowires.

Chapter 4. OPTICALLY ORIENTED ATTACHMENT OF NANOSCALE METAL-SEMICONDUCTOR HETEROSTRUCTURES IN ORGANIC SOLVENTS VIA PHOTONIC NANOSOLDERING

The work presented in this chapter is the result of a collaborative project between the Holmberg lab and the Pauzauskie lab (UW Materials Science and Engineering). Dr. Matthew Crane, Professor Jim Davis, and Professor Peter Pauzauskie provided analytical heat transport calculations included within this chapter.

Reproduced with permission from "Crane, M.J., Pandres, E.P., Davis, E.J. *et al.* Optically oriented attachment of nanoscale metal-semiconductor heterostructures in organic solvents via photonic nanosoldering. *Nat Commun* **10,** 4942 (2019). https://doi.org/10.1038/s41467-019-12827-w".

4.1 INTRODUCTION

The ability to synthesize nanoscale colloidal materials with controlled composition, morphology, and electronic structure has increased rapidly over the past decades.[341]. However, our capacity to integrate nanomaterials into devices remains limited by the ability to deterministically assemble atomically precise nanostructures.[84,226,342–345] Creating junctions between different nanomaterials is a unifying challenge in the production of almost all nanoscale devices, and overcoming barriers in this area will disrupt conventional technologies and spur the development of new ones.[130,321,346–349] Devices built from colloidal nanomaterials that rely on rectifying heterostructures – e.g. highly efficient photovoltaics,[350,351] light emitting diodes,[352,353] and sensors[354–356] – are typically produced by sequential deposition of different colloidal nanoparticle solutions to form junctions between layers of materials via spin coating, dip coating, or doctor blading.[357] In addition, there are a range

of techniques to assemble colloidal materials in solution based on hydrodynamic effects or particle-particle interactions.[358–361] However, none of these methods deterministically produce heterojunctions between individual nanoparticles. An alternative approach is to directly synthesize periodic nanowire junctions, for example, by exchanging gaseous semiconductor precursors during a seed particle-directed growth process to yield epitaxially matched nanowire heterojunctions.[362,363] Nonetheless, this approach is limited by the compatibility of the seed particle with the semiconductor material. Moreover, the above methods cannot produce rationally designed metal-semiconductor-metal or metal-metal-metal junctions between colloidal nanomaterials, critical for quantum computing and thermoelectrics.[321] For example, superconductor/non-superconductor interfaces, such as those in a superconductor-bismuth-superconductor junction, are important for quantum computing via Majorana states and studies of topological insulators.[130,349] Currently, applications involving single- or few-particle junctions are forced to rely on lithography due to the challenges outlined above. However, lithographically synthesized nanomaterials are limited in comparison to colloidal chemistries, which can be used to produce materials with a wide range of compositions, geometries, and dopant distributions.

In 2018, Arthur Ashkin shared the Nobel Prize in Physics for the development of the optical trap, which allows the three-dimensional, non-contact manipulation and study of individual nanostructures.[342] Optical traps have the potential to deterministically manufacture heterojunctions between individual nanostructures.[226,341,343,347,348,364–367] To date, the use of optical traps has almost exclusively been limited to the study of cells or materials dispersed in aqueous media.[368,369] The restriction to aqueous solvents severely limits both the library of materials available for single particle trapping and the range of possible experiments. For example, a large fraction of technologically important colloidal nanomaterials are produced and handled in anhydrous organic

solvents, as exposure to water can often interfere with the desired chemistry or degrade material properties. Moreover, exclusively trapping in water limits studies of hydrodynamic effects, chemical reactions, and electronic excitations to the range of physical properties exhibited by water, water-soluble reactants, and electronic transitions that will not be quenched by dipole coupling to water.[341]

Although nonaqueous solvents have been explored as media for optical trapping in a few reports—for example, Spadaro et al. demonstrated optical trapping of gold-silica mesocapsules in ethanol,[370] Sainis et al. investigated the impact of surface moieties on organic beads in nonpolar solvents,[371] and Black et al. presented the optical trapping of silica-coated polymer microspheres in organic solvents[346]—to the best of our knowledge, the optical trapping and manipulation of colloidal inorganic nanomaterials in organic solvents has not yet been reported. Here, we demonstrate the optical trapping and assembly of metal nanocrystal-seeded semiconductor nanowires in organic solvents with viscosities up to 28 times greater than water. A modified version of an established organic solution-liquid-solid growth process was employed to synthesize bismuth-seeded germanium nanowires, which were then used as nanoscale building blocks for the optical assembly of extended semiconductor-metal-semiconductor heterostructures in organic solution. Both discrete dipole approximation (DDA) calculations and experimental data show that the bismuth nanocrystal seeds experience greater radiation pressure than the germanium nanowires, causing the bismuth-tipped ends of the nanowire to orient away from trapping laser, with the nanowire's growth axis aligned parallel to the Poynting vector of the incident laser.[372,373] We leveraged this effect in tandem with an optically driven nanosoldering process, to construct arbitrarily long, periodic bismuth nanocrystal-germanium nanowire heterostructures freely in non-aqueous solution. Heat transport analysis reveals significant photothermal heating of optically

trapped nanowires in organic solvents relative to aqueous environments due to the reduced thermal conductivity of the organic solvent. Moreover, coupled electromagnetic and heat transport simulations demonstrate that particles trapped and assembled freely in solution reach significantly higher local temperatures—without bubble nucleation or autoignition—as compared to particle trapping and assembling on a surface, due to the large Young-Laplace interfacial surface pressure.[368,374]

4.2 EXPERIMENTAL DETAILS

4.2.1 *Materials*

Bismuth (III) chloride ($BiCl_3$, 99.99% trace metals basis), ethanol (anhydrous, ≤0.005% water), molecular sieves (3 Å), 1-octadecene (ODE, 90%), sodium bis(trimethylsilyl)amide (1.0 M solution in tetrahydrofuran), squalane (96%), tetrahydrofuran (THF, anhydrous, ≥99.9%), toluene (anhydrous, 99.8%), trioctylphosphine oxide (TOPO, 90%)were purchased from Sigma-Aldrich. Diphenylgermane (>95%) was purchased from Gelest. Poly(1-hexadecene-co-1-vinylpyrrolidinone) (PHD-co-PVP) was provided by Ashland under the trade name Ganex™ V-216.

4.2.2 *Bismuth nanocrystal synthesis*

Bismuth nanocrystals were synthesized based on the protocol outlined by Wang, et al.[61] A 25 wt% solution of PHD-co-PVP in 1-octadecene was dried over molecular sieves for one week. $BiCl_3$ (2.6×10^{-2} mmol) was mixed at 800 RPM with THF (570 μL) under nitrogen for thirty minutes. The solution of PHD-co-PVP in octadecene (6.1 mL) was added to the flask under continuous

mixing at 900 RPM. The flask was cycled between nitrogen and vacuum three times. Sodium bis(trimethylsilyl)amide (825 μL) was injected, and the flask was stirred until a dark orange-brown color was observed (~10 minutes, 1100 RPM). The solution was then heated to 200°C for 17 hours, cooled, and then transferred into a nitrogen-filled glove box for storage. Bismuth nanocrystals were handled under nitrogen for cleaning. Nanocrystals were washed five times using a 1:4 ratio of anhydrous hexanes:ethanol and centrifugation (6800 RCF for 10 minutes) to remove excess PHD-co-PVP prior to use for nanowire growth.

Briefly, a solution of 25 wt % PHD-co-PVP in 1-ODE was dried over molecular sieves for one week. Using typical Schlenk line techniques, $BiCl_3$ (71 mg) was combined with anhydrous THF (0.46 mL) and stirred at 950 RPM. After one hour of mixing, 6.1 mL of dried 25 wt % poly(1-hexadecene-co-1-vinylpyrrolidinone) in 1-ODE was added and vacuum was quickly pulled on the solution before returning to nitrogen and increasing the mixing speed to 1150 RPM. 1.2 mL of 1.0 M sodium bis(trimethylsilyl) amide in THF was quickly injected into the flask under nitrogen and the reaction ran for 17 hours. The nanocrystals were cooled and immediately transferred to a nitrogen atmosphere for storage and future purification. Nanocrystals were washed five times using a 1:4 ratio of anhydrous hexanes:ethanol and centrifugation (6800 RCF for 10 minutes) to remove excess PHD-co-PVP prior to use for nanowire growth.

4.2.3 *Bismuth-seeded germanium nanorod synthesis*

To synthesize germanium nanorods, a modified synthesis from Chockla, et al was implemented.[375] Briefly, TOPO (2 g) and squalane (4 mL) were combined in a round-bottom flask at 900 RPM and degassed for an hour and a half at 150 °C. Purified bismuth nanocrystals (200 μL) were diluted with squalane (400 μL) prior to being added to the reaction flask. Low boiling point solvents were

removed by quickly placing the flask under vacuum. The solution was heated to 350 °C and a solution of 50 μL DPG in 500 μL squalane was rapidly injected. The reaction ran for ten minutes, was cooled 100 °C, quenched with 10 mL of anhydrous toluene, and transferred to a nitrogen atmosphere. A fraction of the nanorod dispersion (500 μL) was removed from the glove box and cleaned with a ratio of 2:3 toluene:ethanol and centrifuged at 3885 RCF for 10 minutes for a total of five washes. The resulting bismuth-seeded germanium nanorods were redispersed in toluene for further characterization.

4.2.4 *Materials Characterization*

Transmission electron microscopy (TEM) images were acquired with a FEI Technai G2 F20 Supertwin TEM operating with a 200-kV accelerating voltage and were analyzed using ImageJ Software. Raman spectra were collected on a Renishaw inVia Raman scpectroscope connected to a Leica upright DMLM microscope. A 785 nm laser was focused with a 50x objective. Optical microscopy images were collected with ThorLabs high resolution CCD camera.

4.2.5 *Back focal plane interferometry and temperature calculations*

The optical trapping kit was purchased from Thor Labs and modified with a different condenser. During trapping, forward-scattered light was collected with a long-working-distance 10X Mitutoyo condenser (Plan Apo infinity-corrected long WD objective, stock no. 46–144) and focused onto a quadrant photodiode, providing a measurement of the trapped nanowire position. The quadrant photodiode data was collected with a DAQ card (PCIe-6361 X series, National Instruments) and controlled with home-built LabVIEW software.[376] Power spectra were collected

and fit to solve for the diffusion coefficient. These diffusion coefficients were then used to calculate the local temperature at either the hydrodynamic radius of the particle or at the surface of the particle using a hot Brownian motion correlation. The instrument and methodology described here are outlined in previous reports in more detail.[369,374,376]

4.3 RESULTS AND DISCUSSION

4.3.1 *Optical trapping and alignment in organic solvents*

To trap, manipulate, and assemble colloidal nanostructures in organic solvents, we employed a home-built optical trap (Figure 4.1a) that consisted of a tunable, linearly polarized, diode-pumped, solid-state Yb^{3+}:YAG thin-disk laser set to 1020 nm, a beam expansion region, a 100X trapping oil-immersion objective (NA = 1.25), and a modified perfusion chamber with a 300 μm spacer.[369,377] Germanium nanowires were grown from colloidal bismuth nanocrystal seeds via a solution-liquid-solid process using a modified version of an established synthetic protocol, described below.[375] The perfusion chamber was loaded and sealed in a nitrogen-filled glovebox. The nanowires investigated in this study had monodisperse diameters tunable from 10 to 100 nm with corresponding lengths ranging from 0.1 to 5 micrometers, depending on the chosen synthetic parameters. The bright-field and dark-field transmission electron microscopy (TEM) images in Figure 4.1b and Figure 4.1c illustrate the presence of bismuth nanocrystals on the tips of the germanium nanowires after growth, as well as the monodispersity of the nanowires used in the optical trapping experiments.

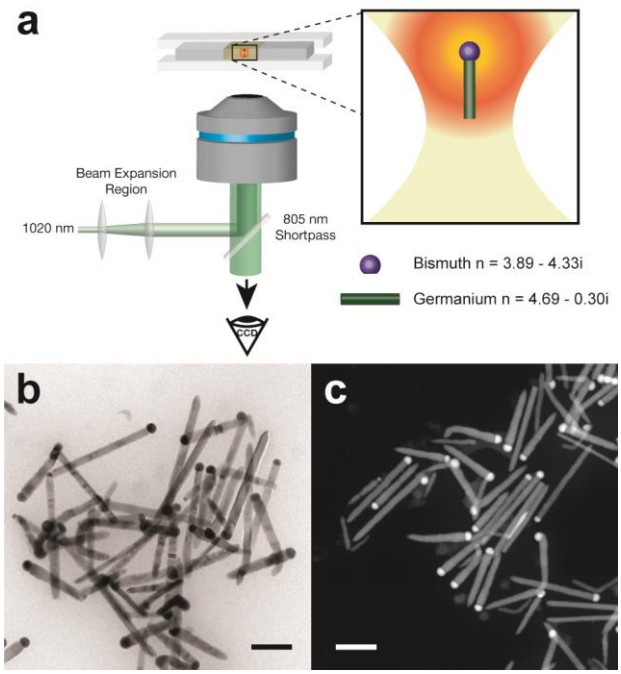

Figure 4.1. A diagram of the optical trap and images of bismuth-seeded germanium nanowires. A schematic of the optical trapping experiment (a), and bright-field TEM (b) and high-angle annular dark field scanning TEM (HAADF-STEM) (c) images of the germanium nanowires used in this study. Scale bars are 200 nm.

To demonstrate the range of solvents available for optical trapping in organic media, we prepared nanowire dispersions in mixtures of toluene and squalane and were able to optically trap nanowires in these solvents. This significantly expands the currently reported range of liquid viscosities suitable for trapping from 1 cP to 28.4 cP with Prandtl numbers ranging from 7.1 to 317.[341,346,378] We were able to trap individual nanowires at powers ranging from 1.0 to 10 W (limited by the trapping laser). Figure 4.2a shows the power spectrum of an optically trapped germanium nanowire in squalane, illustrating the Hookean trapping force acting on the nanowire.

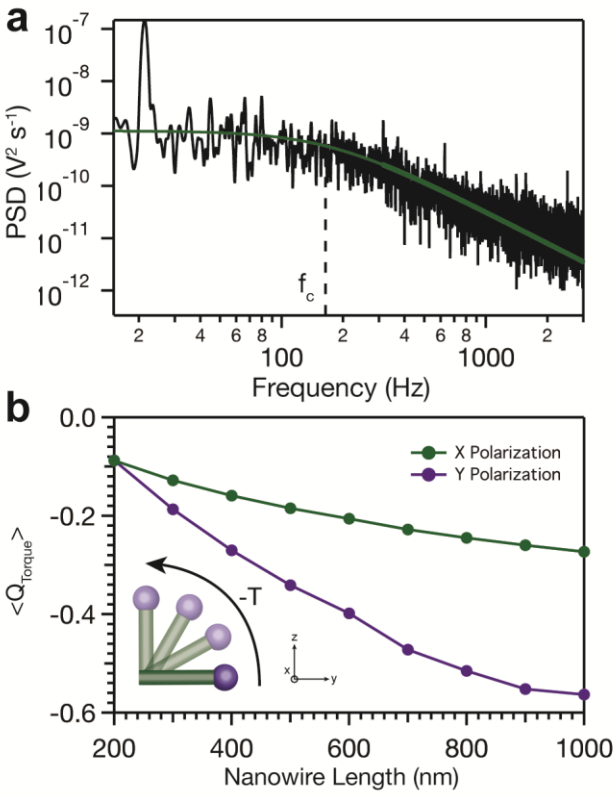

Figure 4.2. Optical trapping and orientation of metal-seeded nanowires. The power spectrum (a) of an optically trapped germanium nanowire was collected via back focal plane interferometry and shows radial confinement of the nanowire. The green line shows a fit of the power spectrum to a Lorentzian with a corner frequency of 164 Hz, highlighted by the dashed line. The spike at low frequency is used to calibrate the nanowire position. Prior to optical trapping, far from the focal plane, the nanowire experiences a scattering-induced alignment torque due to the axial anisotropy of the bismuth-tipped nanostructure. Panel (b) illustrates the torque for a y-polarized plane wave averaged over all theta angles of the nanowire.

As discussed below, power-dependent temperatures and highly non-isothermal temperature distributions within optically trapped particles prevent an exact determination of the trap stiffness. With this caveat in mind, assuming a non-isothermal particle and extrapolating solvent properties (Figure 4.3), a trapping stiffness of ~1.0 pN·μm^{-1} was calculated.

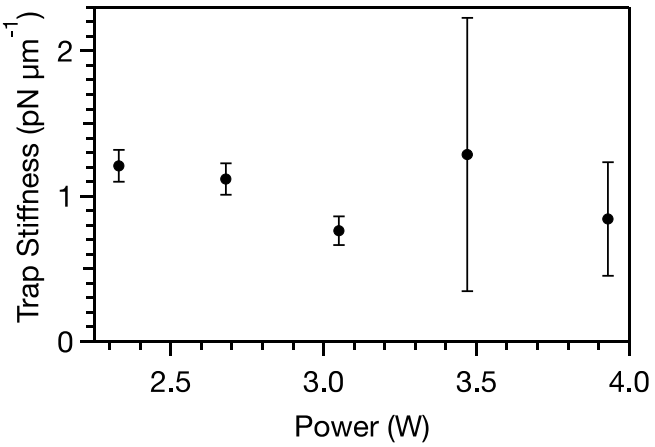

Figure 4.3. The calculated trap stiffness as a function of power before beam expansion.[369,379] Note that this includes the temperature-dependent solvent properties shown in Figure C.1. The significant variation in viscosity with trapping power strongly influences the trap stiffness. Error bars indicate the standard deviation from three separate measurements.

Notably, these trapping stiffnesses are comparable to those observed for InP nanowires trapped in water.[380,381] We observed that nanowires longer than 1 μm were generally easier to trap than shorter nanowires. To achieve stable trapping, the gradient force must eventually overcome the scattering force. The potential well created by the combination of these forces establishes the equilibrium position of the optically trapped particle, which typically sits slightly above the focal plane of the trap. One potential explanation for the difficulty of trapping smaller wires could be a polarization-induced torque in the optical trap that draws the nanowire into the plane of linear polarization. Tilting the nanowire increases its projected surface area and the scattering force, thus prohibiting trapping.[382] The observation that longer nanowires trapped more reliably could also be due to the different optical gradient and scattering forces acting on the germanium nanowire and the attached bismuth nanocrystal, which act to repel the bismuth tip. To estimate these forces, we used Discrete Dipole Scattering (DDSCAT) code[372] to calculate the relative radiation pressure on bismuth and germanium within a single nanowire. The radiation pressure exerted on a bismuth

nanocrystal was calculated to be ~15 times greater than the radiation pressure on an equivalent volume of germanium.[383,384] The disparate forces experienced by the nanowire and its metal tip are predominantly due to the large imaginary component of the refractive index of bismuth (n_{Bi} = 3.89 - 4.33i), as compared to germanium (n_{Ge} = 4.65 - 0.30i). Thus, in the optical trap, the scattering force is reduced when the bismuth sits farther from the focal plane, enabling a more stable optical trap and explaining why longer nanowires trap more efficiently (Figure 4.4).[381]

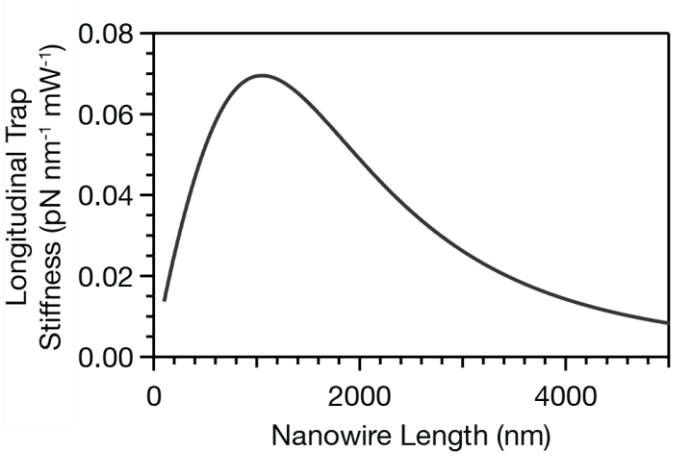

Figure 4.4. Analytical approximation of nanowire longitudinal trap stiffness as a function of length, using the theory developed by Simpson and Hanna.[381] To include the effect of nanowire length, we used the Maxwell-Garnett approximation weighed by the volume fraction of the bismuth nanocrystal, which remains constant, and the germanium nanowire, which varies with length. In the first region, the longitudinal trap stiffness increased as the length of that nanowire increased up to ~1200 nm—that is, as the distance from focal plane to the bismuth nanocrystal increased. This reflects the observation that longer nanowires are easier to trap than shorter nanowires. In the second region, the trap stiffness decreased due to a decreased magnitude of the gradient force as more of the nanowire sits outside of the focal plane.

These anisotropic radiation-pressure effects also occur prior to optical trapping, as the laser pushes the nanowire toward the focal plane. At large distances from the high electric field gradient

in the focal plane of the optical trap, radiation pressure is the dominant force, effectively inducing a torque on the nanowire. This torque causes the nanowire to align vertically in the trap with the bismuth nanocrystal-tipped end of the wire oriented away from the laser source (Figure 4.2b).[342,382,385,386] Moreover, thermophoretic effects[364,387,388] due to anisotropic heating of the bismuth nanoparticle and hydrodynamic drag[359,389] are additional forces that act on the nanowire before trapping to push the bismuth end of the nanowire away from the laser source, resulting in nanowire alignment. Given the high free carrier concentration in virtually all metal seeds employed in the growth of semiconductor nanowires, these simulations suggest that anisotropic radiation pressure likely represents a general method to align nanowires produced by seeded-growth mechanisms.[84] As was noted during the optical trapping of similarly high refractive index nanowires in water with lengths that exceed the length of the focal volume (Rayleigh range), the gradient force experienced by the wire was independent of nanowire length.[380,386,390] For germanium nanowires in these experiments, the gradient force acting on the germanium section of nanowire was largely responsible for enabling optical trapping, while the scattering forces experienced by the metal seed were responsible for orientation (Figure 4.4).[381]

4.3.2 *Nanosoldering bismuth nanocrystal-germanium nanowire heterojunctions*

To demonstrate the application of alignment forces in organic solvents, we used the optical trap to assemble periodic bismuth nanocrystal-germanium nanowire heterostructures from colloidal nanowires dispersed in squalane (Figure 4.5).[343,347,348,367] We accomplished this optically oriented alignment and attachment by trapping a single nanowire and then moving it towards a second nanowire in Brownian motion outside the optical trap (Figure 4.5a-c). Radiation pressure then oriented and accelerated the second nanowire toward the first trapped nanowire. When the second

nanowire reached the first nanowire in the trap, it “soldered” coaxially, tip-to-tail, with the first nanowire, overcoming interfacial electrostatic and hydrodynamic forces (Figure 4.5d).[364,366,371,388] When the nanostructure was released from the trap, optical images showed a bismuth-germanium-bismuth-germanium heterostructure with twice the length of an individual nanowire (Figure 4.5e). Re-engaging the optical trap allowed us to repeat this process, soldering additional oriented nanowires to fabricate long, periodic heterostructures in solution (Figure 4.5f). Radiative heating of the trapped nanostructure (discussed below) enabled the tip-to-tail nanosoldering to produce the repeating nanowire heterostructures. The addition of diphenylgermane (DPG) to the solution enhanced fusion of the optically aligned nanowires. The bismuth seeds are visible at the interface between nanowires in the heterostructure (Figure 4.5f). Raman spectroscopy (Figure 4.5g) also demonstrates that ensembles of germanium nanowires dispersed in toluene retain their crystallinity even after extended laser heating at high irradiances with a focused (~1.5 $MW \cdot cm^{-2}$) and unfocused, collimated (50 $kW \cdot cm^{-2}$) beam.

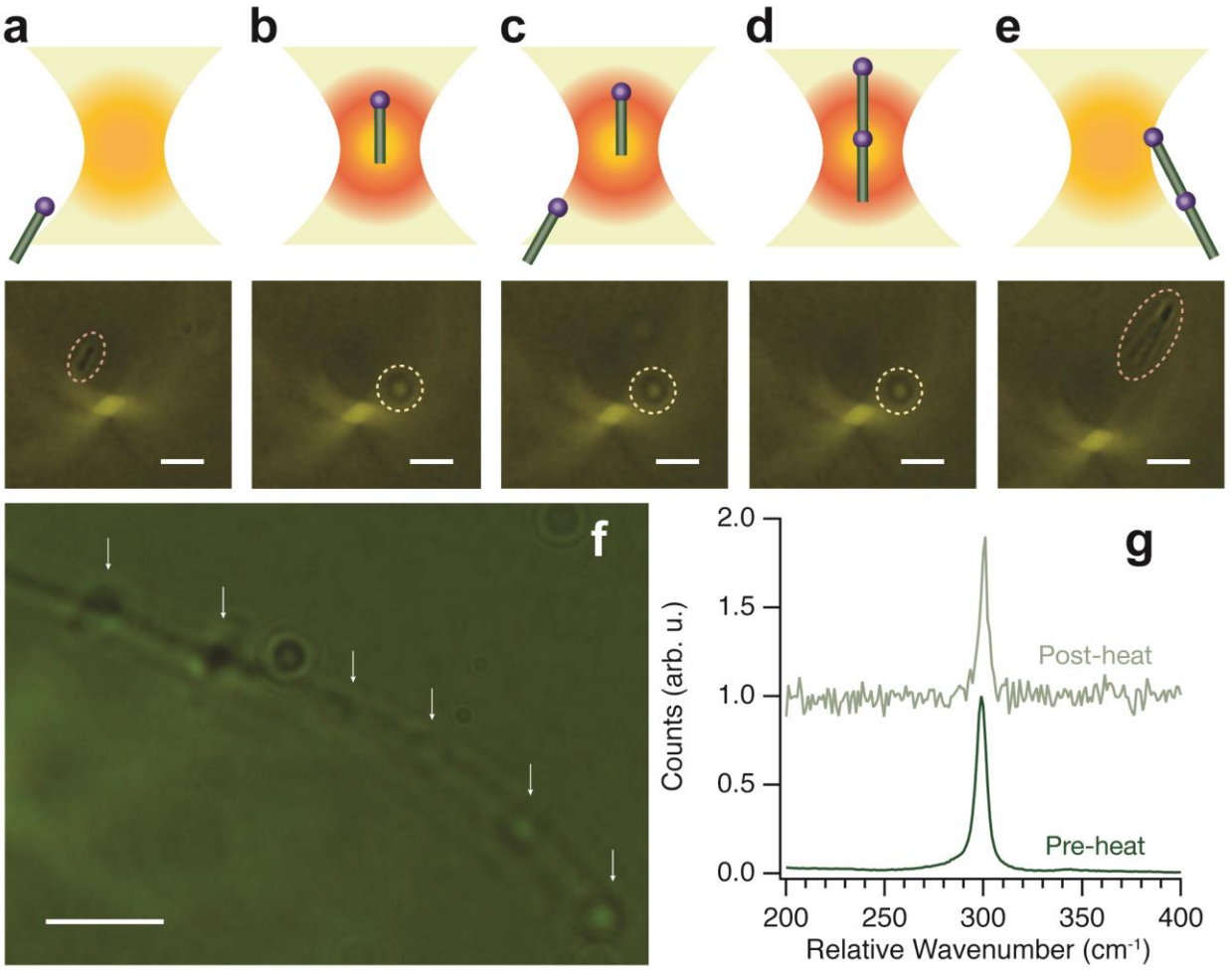

Figure 4.5. Demonstration of optically oriented nanowire assembly via photonic nanosoldering. First, radiation pressure pushes (a) a single nanowire into the optical trap (b). We then bring the trapped nanowire near a second nanowire diffusing freely in Brownian motion (c). Forces due to asymmetric radiation pressure combined with photothermally induced laser heating result in the formation of an optically aligned coaxial heterostructure (d), which is subsequently released back into Brownian motion (e). An image showing a periodic heterostructure assembled at a trapping power of 5.5 W in an environment of squalane with DPG. The white arrows illustrate bismuth nanocrystal junctions between each of the germanium segments (f). Orange circles highlight freely moving, untrapped nanowires while yellow circles indicate optically trapped nanowires. All scale bars are 2 μm. Raman scattering (g) from ensembles of germanium nanowires dispersed in toluene before and after photothermal heating by both a focused (~1.5 $MW \cdot cm^{-2}$) and unfocused, collimated (50 $kW \cdot cm^{-2}$) 1070 nm laser demonstrates that photothermal heating during trapping does not alter the crystallinity of the material.

4.3.3 *Laser heating during trapping in organic solvents*

When employing water-based optical trapping with a near-infrared (NIR) laser, the relatively large absorption coefficient of water can lead to appreciable adventitious solvent heating. For temperature-sensitive measurements, this effect has led to the use of D_2O as a trapping medium due to its low NIR absorption coefficient.[369] A number of groups have independently studied photothermal solvent effects and have measured heating on the order of ~1–10 K/W.[368,391] As a potential alternative, organic solvents often exhibit significantly lower NIR absorption coefficients and thermal conductivities.[392] For an empty optical trap, the dominant heat dissipation mechanism is thermal conduction. Using reported NIR absorption coefficients, α, and thermal conductivities, λ, we estimate that the solvent-induced heating in toluene ($\alpha = 3.5\ m^{-1}$, $\lambda = 0.14\ W \cdot m^{-1}K^{-1}$) is 1.7 W/mK.[391] A similar analysis for water ($\alpha = 29\ m^{-1}$, $\lambda = 0.60\ W \cdot m^{-1}K^{-1}$) yields 3.6 W/mK, suggesting that, for an empty trap, solvent-induced heating effects are slightly lower in organic solvents than in aqueous solvents. However, when the optical trap contains a highly absorbing particle, the lower thermal conductivity of organic solvents (~$0.15\ W \cdot m^{-1}K^{-1}$) leads to significantly greater local temperatures. The powers reported are measured after beam expansion and before the high numerical aperture trapping objective, which decreases the laser power by less than 30% at these trapping wavelengths.

The conventional approach to determine the temperature of an optically trapped particle uses back focal plane interferometry to determine the diffusion coefficient of the particle in the trap. With sufficient knowledge of the physical characteristics of the trapping medium and the size of the particle, this information enables calculation of the temperature of the particle.[376,393] Using this formalism, we report both the average temperature at the hydrodynamic radius of trapped nanowires and the average temperature of the nanowire at irradiances relevant for nanosoldering

(Figure 4.6). These average temperatures vary from 135 to 221°C at the hydrodynamic radius and 266 to 392°C at the nanowire surface, depending on the trapping power, thus illustrating significant heating of the trapped nanowire, along with a steep temperature gradient in the surrounding fluid. Notably, the temperatures at the nanowire surface are above the bulk bismuth melting point of 271°C. Moreover, to the best of our knowledge, these temperatures are higher than the temperature of any previously measured, optically trapped nanowire in solution. Finally, although this methodology used to measure particle temperature assumes that the trapped particle is isothermal, the stark differences in the optical properties of the bismuth tip and the germanium wire produce a large thermal gradient within the trapped nanowire that perturbs the local fluid properties.

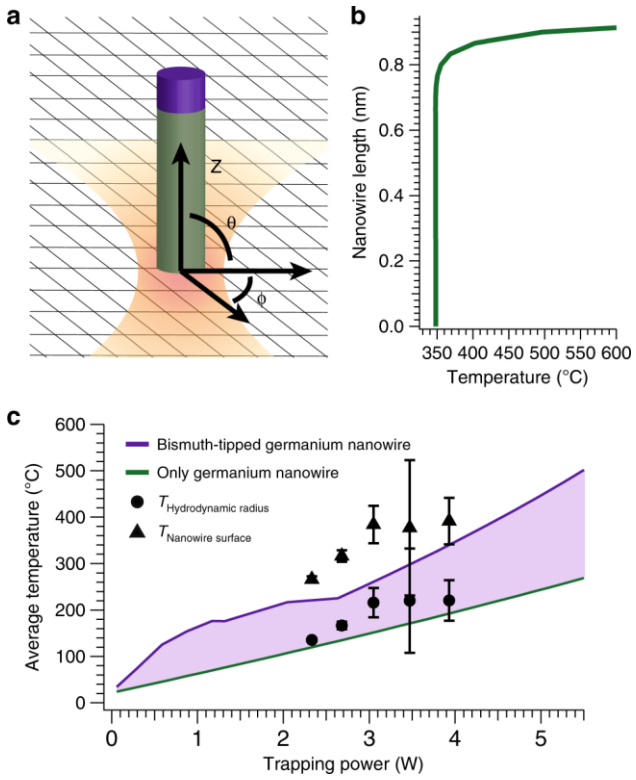

Figure 4.6. Analytically predicted temperatures of an optically trapped bismuth-seeded germanium nanowire. Average local temperature along the length of the nanowire (b) during trapping at a power of 5.5 W, showing that the entire nanowire is above the bismuth melting temperature during alignment and nanosoldering, and that the end of the nanowire near the bismuth tip experiences

significantly higher local temperatures. To create lower and upper temperature bounds for the optically trapped nanostructure, the average temperatures of trapped germanium nanowires with (purple) and without (green) bismuth tips were calculated as a function of trapping power (c). Appendix C includes full details of these calculations. Average experimental temperatures at the nanowire surface were calculated using a hot Brownian motion diffusion model.[394] Error bars indicate the standard deviation of the average temperature from three separate measurements.

To validate these temperatures and elucidate the nanosoldering mechanism, we modified the theory developed by Roder et al.[377] for a germanium-bismuth nanowire heterostructure. We approximated the heterostructure as a cylinder with bismuth and germanium sections (Figure 4.6a) and solved the heat conduction equation

$$\rho C_p \frac{\partial T}{\partial t} = \kappa \nabla^2 T + \dot{Q}''' \tag{4.1}$$

in each section of the cylinder, where ρ, κ, and C_p are the density, thermal conductivity, and specific heat capacity, respectively, of the bismuth or germanium portion of the nanowire. The cylinder-cylinder approximation of the heterostructure in Figure 4.6a simplifies the heat transport analysis and is valid when the diameter is much smaller than the wavelength of the trapping laser, as in this case. The heat generated per unit time per unit volume, $\dot{Q}'''$, depends on the laser irradiance and polarization, and is related to the electric field $\mathbf{E}$ and its complex conjugate $\mathbf{E}^*$ by

$$\dot{Q}''' = \frac{2\pi Re\{n\}Im\{n\}}{\lambda \mu c} \mathbf{E} \cdot \mathbf{E}^* \tag{4.2}$$

where n in the complex refractive index, λ is the wavelength of the incident laser irradiation, c is the velocity of light, and μ is the electromagnetic permeability. Table C.1 contains all parameter values for the heat transport calculations. For isotropic cylinders and spheres, Mie theory solutions provide the complex internal electric field, $\mathbf{E}$, to calculate the source term. However, for the

cylinder-cylinder geometry (Figure 4.6a), there is no analytical solution. Consequently, we used numerical discrete-dipole calculations to determine the electric field.

As discussed below, photothermal heating melts the bismuth nanocrystal, forming a liquid metal droplet at the nanowire tip that facilitates nanosoldering.[375] As such, we allowed the composition and optical characteristics of the molten droplet to vary with temperature in accordance with the Bi-Ge binary phase diagram. Data regarding nonlinear absorption effects, including saturation and two photon absorption, in bismuth are conflicting, with reported values spanning orders of magnitude. Due to these uncertainties, we created upper and lower bounds by considering heat transport analysis on a germanium nanowire with a bismuth tip and a germanium nanowire without a bismuth tip, respectively. These upper and lower bounds resulted in average temperatures of 447°C and 244°C in an ambient bath of squalane at a trapping power of 5 W, which was used for optically oriented attachment (Figure 4.6c).

While the average electric field is similar throughout the nanowire heterostructure, the large value of $\mathrm{Im}\{n\} = 4.33$ for bismuth indicates significant absorption relative to $\mathrm{Im}\{n\} = 0.30$ for germanium. Furthermore, the low Biot number of the nanowire suggests that there is little radial temperature variation. The radially-averaged temperature profile of a single bismuth-germanium nanowire trapped at 5 W (Figure 4.6b) illustrates that the bismuth tip is significantly hotter than the germanium wire, due to the disparity in heat generation. We calculate that the bismuth nanocrystal melts at a distance of ~50 μm below the focal plane of the optical trap due photothermal heating. Indeed, calculations show that a trapping power of only 0.35 W is sufficient to melt the bismuth nanocrystal tip in the optical trap's focal plane. Because the time scale to achieve steady-state heating ($< 10^{-9}$ s) is much less than the time for radiation pressure to drive the

nanowire into the optical trap (10^{-2} – 1 s), the incoming nanowire is at a steady-state temperature as it approaches the trap.[395]

During attempts to trap and assemble nanowires dispersed in toluene, nanowires accelerated toward the trap at higher velocities than in squalane and occasionally fused at an angle, rather than coaxially. This resulted in the binding of nanowires at angles, yielding radially-asymmetric structures that eventually rotated out of the trap. While impractical for the continued production of linear periodic heterostructures, this does illustrate the potential application of the nanosoldering process to create more complicated structures.[396] One explanation for this phenomenon is the massive disparity between the viscosity of squalane (28.4 cP) and toluene (0.58 cP). The hydrodynamic drag force in toluene is three orders of magnitude lower than the drag force in squalane; consequently, the radiation pressure required to align and push the nanowire into the optical trap is three orders of magnitude higher in squalane than in toluene. For the Gaussian beam profile used in the single-beam optical trap, there exists a much smaller solid angle over which this balance of forces is satisfied in squalane than in toluene. Thus, nanowires in predominately squalane solutions are only aligned and trapped if they are almost directly below the optical trap—that is, if $\theta \approx 0$. However, in toluene, radiation pressure and torque will act over a much wider solid angle ($\theta > 0$) to drive nanowires into the optical trap, which can enable off-axis addition. Another potential challenge is that, given the low Reynolds number of the system, nanowires enter the trap at their terminal velocity, which is determined by the viscosity of the solvent and the laser power.[342] The large difference in viscosity between squalane and toluene illustrates that nanowires will approach the trap at much higher velocities in toluene than in squalane, which may prevent optical alignment prior to nanosoldering. Thus, using a viscous solvent enables oriented alignment by decreasing the solid angle of radiation pressure, thereby restricting the volume and angle of

nanowires approaching from below the optical trap. In addition, using a high power may be required to impart large radiation pressure forces to align the nanowire prior to entering the trap. Alternatively, heating-induced hydrodynamic effects could also facilitate nanowire alignment.

Notably, the trapped nanowire can reach very high temperatures without locally boiling the solvent due to the high Young-Laplace interfacial surface pressure.[368] To demonstrate the impact of the Young-Laplace pressure, we trapped a nanowire in squalane at 5 W and moved it toward a glass slide, which provided a flat surface for bubble nucleation. Although stable in solution, when the nanowire reached the surface of the glass slide, the solvent immediately boiled and ignited, despite the high thermal conductivity of glass compared to squalane, indicating that the large Young-Laplace pressure prevents local bubble nucleation and ignition near the nanostructure. Importantly, docking with a surface can easily be achieved safely by simply switching to a lower laser power or using a higher viscosity solvent, thus suppressing bubble formation. Both of these strategies enable the safe manipulation of optically trapped materials in organic solvent systems. This serves as a critical safety demonstration, while also highlighting the significant processing advantage afforded by working in solution as opposed to on a surface, thus enabling higher temperature transformations. Moreover, when carrying out a high-temperature manipulation, such as nanosoldering, on a trapped structure in an organic solution, it is critically important to reduce the power of the trapping laser prior to docking the structure with a surface.

4.4 CONCLUSION

This analysis indicates that nanosoldering occurs through sequential steps. First, the radiation pressure from the optical trap acts asymmetrically on the nanowire to exert an optical torque that orients the bismuth nanocrystal tip away from the incident laser and accelerates the nanowire

toward a previously-trapped and aligned nanowire. When the accelerating nanowire comes within ~50 μm of the trap volume, the temperature of the photothermally heated bismuth nanocrystal exceeds the bismuth melting temperature of 271°C, rapidly causing the tip of the nanowire to melt and form a liquid metal droplet. As the nanowire continues to approach the optical trap, its temperature rises, and the gradient force begins to oppose the radiation pressure, decreasing the velocity of the nanowire. Finally, as the gradient force slows the incoming, aligned nanowire, the molten bismuth tip contacts the germanium end of the previously trapped nanowire, fusing the two optically oriented nanostructures together.

In conclusion, we have expanded the range of optical trapping media to include organic solvents and demonstrated the optically oriented assembly of metal-seeded germanium nanowires for the first time. DDA calculations and experimental results show that the bismuth seed particles on the tips of the SLS-grown germanium nanowires experience a significantly greater radiation pressure than the germanium portion of the nanowire, causing it to orient coaxially in the trap, with the bismuth seed oriented away from the incident laser source. In addition, as compared to trapping in aqueous solvents, operating an optical trap in an organic solvent environment facilitates the generation of much higher local temperatures upon trapping due to the decreased thermal conductivity of the solvent. We leveraged these effects to rationally manufacture periodic bismuth nanocrystal-germanium nanowire heterostructures in squalane using an optical trap. We anticipate that these results will usher in a new realm of optical trapping applications, including additive nanomanufacturing from constituent nanomaterial building blocks,[347] single-particle catalysis,[84,346,397] and future hydrodynamic studies.[344,345,371,398,399]

Chapter 5. GERMANIUM NANOWIRE BATTERY ELECTRODES WITH ENGINEERED SURFACE-BINDER INTERACTIONS FOR IMPROVED CYCLE LIFE AND HIGH ENERGY DENSITY WITHOUT FLUORINATED ADDITIVES

The work presented in this chapter is the result of a collaborative project between the Holmberg lab and the Schlenker lab (UW Chemistry). Dr. Jarred Olson and I worked closely together to prepare nanowire-based electrodes, conduct experiments to evaluate nanowire-based electrode performance, and interpret the resulting data.

https://pubs.acs.org/doi/10.1021/acsaem.9b00667

5.1 INTRODUCTION

Group-IV materials, such as silicon and germanium (Ge), continue to garner interest as prospective replacements for graphite as negative electrode materials in lithium ion (Li-ion) batteries due to their high gravimetric lithium storage capacities of 3579 mAh/g and 1384 mAh/g, respectively.[400] Both Si and Ge undergo large volume changes (~300%) upon lithiation,[251] which can cause capacity loss through electrode fracture, deleterious irreversible reactions that trap lithium ions, and electrode delamination from the current collector. Strain and electrode fracture associated with these volume changes can be reduced by nanostructuring the active electrode material,[20,234,248]

particularly for nanowires (NWs).[146,401] NWs produced via colloidal, solution-based methods have been integrated as active materials in devices as freestanding fabrics[21] and as components within a composite electrode.[22,23] Composite electrodes are most commonly obtained by preparing a slurry of active material, conductive carbon, and polymeric binder in some optimized ratio.

Ongoing strategies to improve the cycle life of alloying electrode materials in composite architectures often hinge on controlling the solid-electrolyte interphase (SEI) layer composition and stability.[256,402,403] The SEI layer is a heterogeneous coating of inorganic and organic compounds that forms as electrolyte solvents undergo electrochemical redox processes to form decomposition products at the electrode-electrolyte interface. Both the active material and composite electrode components at the electrode-electrolyte interface can influence the composition and stability of the SEI layer during electrochemical cycling.[404] The continued growth of the SEI layer throughout cycling can lead to the trapping of mobile ions within the layer as well as increased ionic resistance, leading to increased electrochemical impedance.[405] Additionally, the redox byproducts of electrolyte solvents may be soluble in the electrolyte itself, forming a soluble (rather than solid) electrolyte interface.[406–408] Thus, a robust SEI layer is necessary for stable cycling, but the continued growth of the SEI layer, which can occur if fresh electrode surface is exposed, can result in poor capacity retention.

Electrolyte solvents and additives have been shown to strongly influence the cycle life of silicon- and Ge-based electrodes by altering the SEI layer composition, thickness, and ionic conductivity.[402,409,410] Additional strategies have focused on modifying the mechanical and conductive properties of the polymeric binder to enhance its ability to accommodate large volume changes and maintain adhesion to the current collector as well as enhance charge transport, respectively.[24,411–415] Polymeric binders can also influence the composition of the SEI layer by

undergoing different degrees of swelling with the electrolyte solvent, either facilitating or inhibiting reactions at the interface between the binder and the active material.[414,416,417]

The relative reduction potentials of electrolyte solvents and additives largely govern which electrochemical decomposition products are formed first, establishing the innermost portion of the SEI layer, closest to the active material surface.[255,418] The subsequent composition and morphology of the SEI ultimately affects capacity retention.[419–421] In particular, incorporating the FEC additive has consistently been demonstrated to be advantageous – and often considered necessary – in numerous alloying electrode systems, including Si, Ge, and antimony-based electrodes; however, these studies are often performed using materials that likely have surface oxides present due to how the materials are produced and handled.[22,422,423] Without surface functionalization or active coating processes, a native oxide layer forms on Group-IV active materials after brief air exposure upon removal from their growth chamber. This native oxide is particularly important, as it has been proposed to affect the electrochemistry of the SEI layer.[424–426] Moreover, for Ge NW-based composite electrodes using NWs with oxide-terminated surfaces, FEC has appeared to be a critical electrolyte additive for retaining cell capacity and cycle life.[22] Alternatively, alkanethiol functionalized Ge NW-based electrodes were recently demonstrated to have excellent capacity retention over extended cycling using a conventional electrolyte without FEC.[23] Thus, despite the clear importance of interfacial surface chemistry for alloying electrodes, investigations of NW alloying electrodes with careful, well-defined surface chemistry are somewhat limited, likely due to the added difficulty and expense of etching and tailoring NW surface chemistry after air exposure.[427] Likewise, the role of various electrolyte additives has yet to be explored on oxide-free Ge NW electrode surfaces. By comparing electrolyte additives that are structurally similar and undergo similar reductive decomposition pathways, we reveal how the electrochemical

performance of oxide-free, surface-functionalized Ge NWs correlates with electrolyte composition.

Here, we use supercritical fluid-liquid-solid (SFLS)-grown Ge NWs as a model material system to understand the effects of surface chemistry on alloying-type electrode materials. The SFLS process enables in situ surface-functionalization, eliminating potentially expensive and unwieldy acid etching steps and interface oxidation from air exposure. Moreover, since the entire synthesis is carried out in an easily evaporated, volatile organic solvent (toluene in this case), functionalized NW surfaces have intrinsically well-defined surface chemistries, without the need for intensive processing steps to purify samples and remove oily high-boiling-point solvents. We capitalize on the controlled thermal hydrogermylation of the native Ge NW surfaces in situ,[78] and subsequently incorporate these functionalized NWs into composite electrodes with different polymeric binders and electrolyte additives to explore how engineering the interfacial chemistry of functionalized NWs influences cycle life for composite alloying electrodes. We observe both electrolyte- and fabrication-dependent aspects of capacity retention that manifest via delithiation from amorphous and crystalline domains of the nanostructured Ge active material.

5.2 EXPERIMENTAL DETAILS

5.2.1 *Materials*

All materials were used as received without further purification. 1-dodecanethiol (≥98%), fluoroethylene carbonate (99%), hydrogen tetrachloroaurate (III) trihydrate (≥99.99% trace metals basis), lithium metal ribbon (99.9% trace metals basis, 0.75-mm thickness), lithium hexafluorophosphate (99%), N-methyl-2-pyrrolidone (anhydrous, 99.5%), 1-octene (98%), poly(acrylic acid) (average M_W: 1800), sodium borohydride (99.99%), toluene (anhydrous,

99.8%), and vinylene carbonate (≤ 2% BHT as stabilizer, 97%) were purchased from Sigma Aldrich. Chloroform (HPLC grade, 99.9%), toluene (Certified ACS, 99.8%), and Whatman glass fiber separators (19-mm diameter discs, grade gf/f) were purchased from Fisher. Diphenylgermane (>95%) was purchased from Gelest. Ethanol (200 proof) was purchased from Decon Laboratories. Copper foil (9-μm thickness) and poly(vinylidene difluoride) (≥99.5%, average M_W: 600,000) were purchased from MTI. Conductive carbon (Vulcan® XC72R) was obtained from Cabot corporation. Lithium perchlorate (anhydrous, ≥99%) was purchased from Alfa Aesar. Diethyl carbonate (≥99%) and ethylene carbonate (99%) were purchased from BASF. CR2032 type coin cell components were purchased from Pred Materials International.

5.2.2 *Germanium nanowire synthesis and surface functionalization*

Dodecanethiol-passivated gold (Au) nanocrystals were prepared in a mixture of deionized water and toluene via the Brust method.[307] Germanium nanowires were synthesized via SFLS-based growth, and surface functionalized in situ via thermally initiated hydrogermylation with 1-octene.[78] In a typical reaction, a cylindrical 10-mL titanium reaction vessel was transferred into a nitrogen atmosphere glovebox, sealed, and placed in a heating block at 380°C. Keeping the exit valve closed, the reactor was pressurized to 900 psig using anhydrous toluene. A precursor mixture containing 1.7×10^{-2} mg/mL Au nanocrystals and 3.3×10^{-2} M diphenylgermane was prepared in anhydrous toluene (385:1 Ge:Au molar ratio). The mixture was loaded into a sealed stainless-steel piston and subsequently injected into the pre-pressurized and pre-heated reactor (900 psig, 380°C) at a rate of 0.5 mL/min for forty minutes. After nanowire growth, the temperature was then decreased to 220°C for surface hydrogermylation. Nanowire surface functionalization was carried out by injecting 12 mL of 2.1 M 1-octene in anhydrous toluene into the reactor at a rate of 0.5

mL/min for twenty minutes. The reactor temperature was then sealed and held at 220°C for 2 hours, followed by isochoric cooling to room temperature. Nanowires were collected with toluene. All germanium nanowires used in this study were hydrogermylated with 1-octene. Nanowires were washed three times in glass vials with a 2:2:1 ratio of toluene:chloroform:ethanol, and centrifuged at 2355 RCF for ten minutes. The resulting high-aspect-ratio, single-crystalline germanium nanowires produced via this method have diameters ranging from 10 to 100 nm and lengths ranging from micrometers to millimeters.

5.2.3 *Germanium nanowire-based electrode fabrication*

Ge NW electrodes were prepared through two different methods (manual mixing with a mortar and pestle or magnetic stirring in a glass vial), but all composite electrodes were fabricated with a mass ratio of 70% Ge NWs, 10% conductive carbon, and 20% polymeric binder – either poly(acrylic acid) (PAA) or poly(vinylidene difluoride) (PVDF). In a typical "manual mixing" electrode preparation, 50 mg of Ge NWs and 7 mg of conductive carbon additive were combined with 1.5 mL of 9.5 mg/mL polymeric binder (PVDF or PAA) in N-methyl-2-pyrrolidone (NMP) and mixed for ten minutes with a mortar and pestle (manual mixing). The wet slurry was then deposited onto a copper substrate and doctor bladed (25.4-μm thickness). The wet composite electrode on the copper current collector was then placed on a hot plate preheated to 80°C to evaporate the NMP solvent. Figure 5.1 shows characteristic scanning electron microscopy (SEM) images of surface-functionalized Ge NWs before electrode integration, after integration into a composite electrode via manual mixing, and after integration into a composite electrode via magnetic stirring.

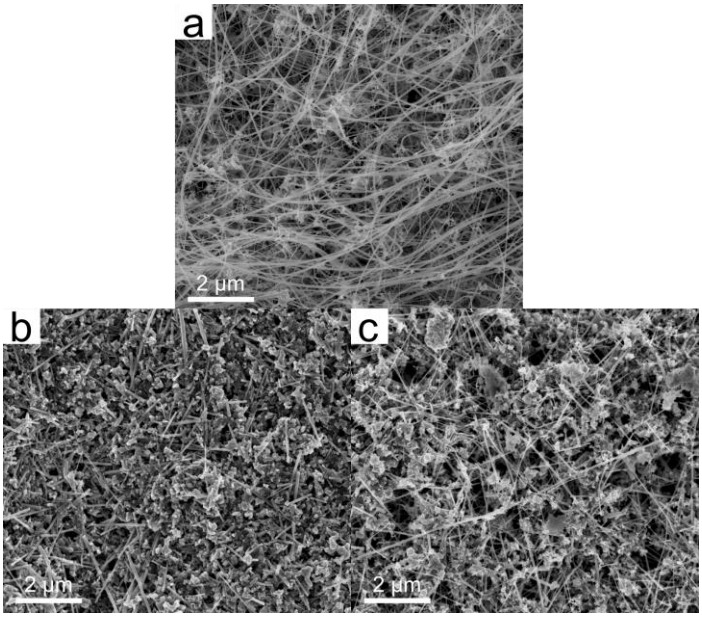

Figure 5.1. SEM images of (a) 1-octene hydrogermylated Ge nanowires before incorporation into a composite electrode, (b) a composite electrode (70:10:20 mass ratio of Ge NWs:conductive carbon:PAA) fabricated via manual mixing with a mortar and pestle, and (c) a composite electrode (70:10:20 mass ratio of Ge NWs:conductive carbon:PAA) fabricated via magnetic stirring.

In a typical "magnetic stirring" electrode preparation, Ge NWs, conductive carbon, and polymeric binder (PVDF or PAA) were combined with 1.5 mL of NMP in a 3 mL scintillation vial and magnetically stirred at 1900 RPM for at least 16 hours. A glass Pasteur pipette was used to transfer the slurry to the copper current collector, which was then doctor bladed to a 25.4-µm thickness and placed onto a hot plate at 80°C until the solvent evaporated. The average areal mass loading of Ge NW active material for fabrication methods that included PAA as a binder was 0.40 mg cm^{-2}, while methods that used PVDF as a binder had an average areal mass loading of 0.60 mg cm^{-2}.

A 15-mm diameter C.S. Osborne hole punch was used to punch out electrodes, which were then dried overnight in a vacuum oven at 100°C that was held at a pressure below 50 mbar. Electrodes were weighed and transferred into an argon-filled MBraun glove box for further

assembly into coin cells. Briefly, the electrode on the current collector, the glass fiber separator, and the plastic spacer were placed in the stainless-steel cup, consecutively. Then 100 μL of the electrolyte solution [1 M $LiPF_6$ in 1:1 w/w EC:DEC (ethylene carbonate: diethyl carbonate), with or without 5% w/w additive (FEC and VC)] was added dropwise onto the glass fiber separator to saturate it. The lithium foil, stainless-steel spacer, stainless-steel spring, and stainless-steel cap were then added to complete the half-cell assembly. A crimper (MTI Corporation) was used to seal the half-cell, whereupon it was transferred to a MACCOR testing unit for cycling.

5.2.4 *Materials characterization*

Transmission electron microscopy (TEM) images were acquired with a FEI Technai G2 F20 Supertwin TEM, operating at 200 kV. Digital Micrograph software was used to generate Fast Fourier Transforms (FFTs) of high-resolution TEM images. Scanning electron microscopy (SEM) images were acquired with a FEI Sirion XL30 SEM operating at 5kV. Galvanostatic measurements were performed with a MACCOR 4200 galvanostat programmed to cycle between 0.01 and 1 V vs. Li/Li^+. The reported specific capacities are based on mass loading of active material, reported rates are based on the theoretical capacity of Ge (1384 $mA \cdot h \cdot g^{-1}$), and the reported capacity retention is relative to the second cycle. All electrodes were tested in duplicate.

5.3 RESULTS AND DISCUSSION

5.3.1 *Surface-functionalized germanium nanowire-based electrodes*

Figure 5.2a shows TEM images of Ge NWs prior to integration into composite electrodes. The high resolution TEM image in Figure 5.2a and the corresponding FFT (inset) indicate that the

SFLS-grown Au-seeded Ge NWs are single-crystalline prior to lithiation, as expected. Notably, all Ge NWs used in this study were hydrogermylated with 1-octene to prevent surface oxides from forming on the NWs. Ge NW composite electrodes fabricated using PAA as a binder along with a range of electrolyte additives demonstrate ~1100 mAh/g gravimetric capacities after 50 cycles (Figure 5.2b), which is close to the theoretical specific capacity of Ge, confirming the high quality of these composite electrodes.

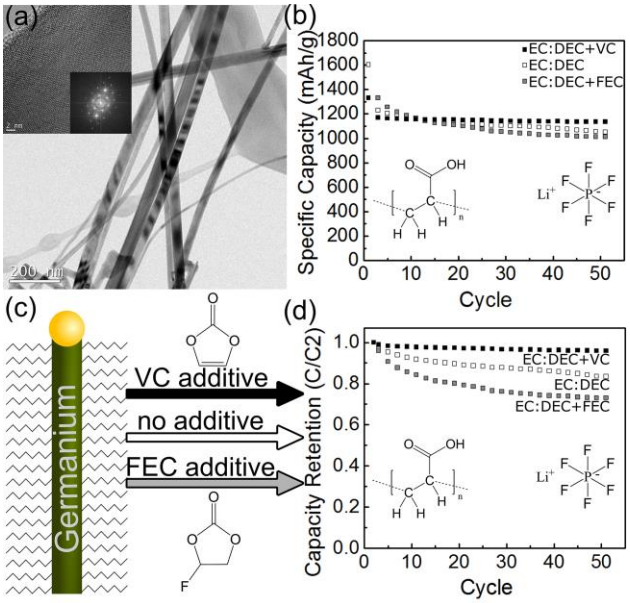

Figure 5.2 (a) TEM images of gold-seeded 1-octene hydrogermylated Ge NWs and (inset) FFT of a high-resolution TEM image. (b) Specific gravimetric capacity of Ge NW electrode composites fabricated via manual mixing, using PAA as a binder, and 1 M $LiPF_6$ in 1:1 w/w EC:DEC with different additives: white (no additive), gray (FEC), and black (VC), cycled at a rate of C/10 (~138 mA/g). (c) Depiction of a 1-octene hydrogermylated Ge NW with different electrolyte additives and (d) the capacity retention of Ge NW composite electrodes fabricated with PAA and cycled at a rate of C/10 (138 mA/g) with different electrolyte additives: white (no additive), gray (FEC), and black (VC) squares. Structural formulas of PAA, FEC, and VC are included for reference.

These surface functionalized Ge NW composite electrodes maintain high capacity retention under extended cycling, as well as under higher cycling rates (Figure 5.3), as has been seen previously for similar Ge NW based alloying electrodes.[23] Although the presence of a large specific capacity is a significant metric for the evaluation of device performance, we also use capacity retention (Figure 5.2d) as a metric to normalize and compare the extent of degradation between electrodes that may have slight variations in absolute capacity.

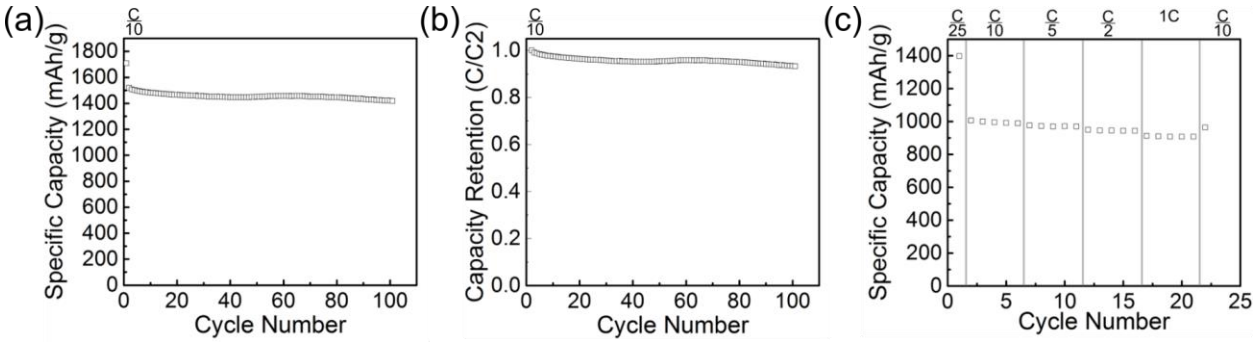

Figure 5.3. (a) Specific capacity and (b) capacity retention for electrodes cycled at a rate of C/10 (138 mA/g) over 100 cycles. (c) Rate test of 1-octene hydrogermylated Ge nanowires cycled at C/25 (55.4 mA/g), C/10 (138 mA/g), C/5 (277 mA/g), C/2 (692 mA/g), 1C (1384 mA/g), and C/10 (138 mA/g). Electrodes were fabricated with PAA via manual mixing and were cycled with a 1M $LiPF_6$ 1:1 w/w EC:DEC electrolyte.

Interestingly, for the hydrogermylated NWs implemented in this study, including FEC as an electrolyte additive adversely affected the capacity retention and cycle life (Figure 5.2d) of the electrode, consistently resulting in the poorest performing devices that employ this particular surface chemistry/binder pairing. Quantitatively, our devices using neat electrolyte solvents without additives (1:1 EC:DEC + 1M $LiPF_6$) consistently exhibited greater capacity retention after fifty cycles (83%) than devices that included the FEC additive (73%). While this performance (see Figure 5.3 for long-term cycling and rate testing) is comparable to the performance of devices

fabricated with alkanethiol-passivated Ge NWs cycled in the absence of FEC that used PVDF as a binder,[23] our results are in stark contrast to previous studies on surface-oxidized Ge NWs,[22] which showed that FEC was critical for robust cycling and capacity retention. In fact, using non-fluorinated VC as an electrolyte additive results in the greatest overall capacity retention for our hydrogermylated Ge NW devices (96%). Moreover, devices that included VC as an electrolyte additive consistently showed very high ~99.5% coulombic efficiencies (Figure 5.4).

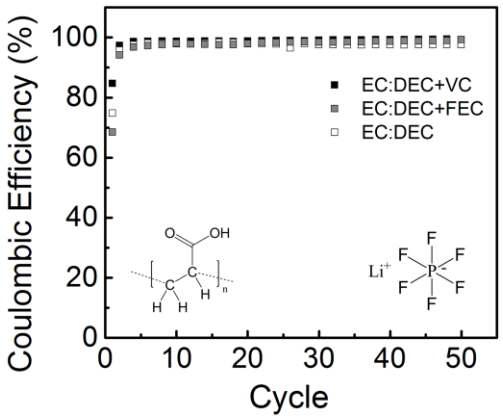

Figure 5.4. Coulombic efficiencies of germanium nanowire composite electrodes fabricated via manual mixing, using PAA as a binder, and 1 M $LiPF_6$ in 1:1 w/w EC:DEC with different additives: white (no additive), gray (FEC), and black (VC), cycled at a rate of C/10.

5.3.2 *Effects of electrolyte additives on the solid-electrolyte interphase layer*

SEI layer formation via the decomposition of different electrolyte solvents has been discussed in depth in the literature, with a heavy focus on the cyclic carbonates. SEI layers produced from reduction of EC-based electrolyte solvents are known to be rich with polyethylene oxides, polycarbonates, and short-chain alkyl dicarbonates.[428] Both VC and FEC-based electrolyte solvents are proposed to undergo similar reduction pathways[429] to form SEIs containing polymeric networks with elastic properties that can withstand the drastic volume changes of the active

material upon lithiation and delithiation, thereby preventing further electrolyte reduction.[430–432] Distinguishing the cycling performance of VC-containing electrolytes from those containing FEC in our data, previous results indicate that the yield of polymeric networks for VC-derived SEIs is higher than FEC-derived SEIs when FEC and VC concentrations are the same.[433] It has been observed that high concentrations of FEC are needed to produce sufficiently robust polymeric SEI structures and minimize electrode cracking.[434] Another recent study by Browning et al. demonstrated that the consumption and instability of polymer networks from an FEC-derived SEI depends on the lithiation state of the electrode.[435] Such effects would minimize the extent to which mechanical properties of a polymeric SEI can stabilize performance as the electrode continuously cycles. Moreover, the presence of fluorine in FEC is believed to produce a SEI structure rich in LiF at the innermost region, which stabilizes the SEI layer.[436] Several studies have also suggested that the presence of FEC could be advantageous with respect to mitigating or etching surface oxides to create a more stable SEI.[437–439] However, in this study, we eliminate the presence of surface oxide by carefully controlling the Ge NW surface chemistry through in situ hydrogermylation. As a result, the previously observed stabilization afforded by the decomposition of FEC on nanostructured Ge electrode materials with native oxide surfaces[437–439] appears to be unnecessary for oxide-free active materials that are surface functionalized prior to electrode fabrication. Consequently, it is likely that the preferential formation of organic species (short-chain alkyl carbonates and polymeric networks from EC and VC reduction, respectively) maintain the cycling stability of high-capacity alloying electrodes with oxide-free surfaces, as opposed to a more inorganic and rigid SEI via FEC reduction.

5.3.3 *The role of electrolyte additives on the cycling characteristics of hydrogermylated Ge nanowire-based electrodes*

To further elucidate the impact of fluorinated compounds on the capacity retention of alkane-functionalized Ge NW composite electrodes with controlled surface chemistry, additional electrodes were cycled in the complete absence of all possible source of fluorine. The standard electrolyte salt, $LiPF_6$, was replaced with $LiClO_4$, and the fluorine-free PAA binder was employed once again – as opposed to the widely used, fluorine-containing PVDF binder system. Although fluorine-free cells formulated without electrolyte additives exhibited continuous capacity decay (Figure 5.5, white squares) with a capacity retention of 83% after 50 cycles, when the fluorine-free additive, VC, was included as an electrolyte additive (black squares), capacity retention improved to 98%, consistently resulting in our best overall device performance with absolutely no fluorine present anywhere in the electrochemical system. These observations strongly suggest that the polymeric network created by the reductive decomposition of VC is much more important for generating a robust SEI layer than forming LiF for electrodes made using Ge NWs with unoxidized alkane-functionalized surfaces. Previous data on bare Ge NWs cycled with a VC electrolyte additive in the absence of binder[440] reveal a lower capacity retention (~75%) within the first 15 cycles than what was observed in this study, suggesting that alkane functionalization and/or the inclusion of PAA binder imparts greater cycling stability to the active material.

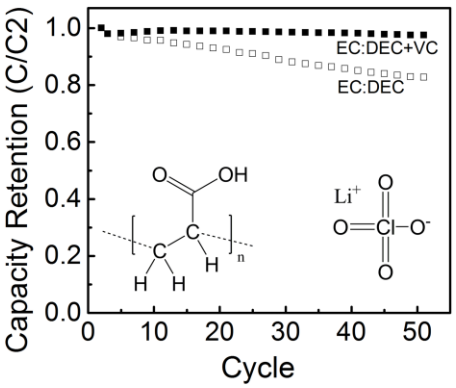

Figure 5.5. Capacity retention of fluorine-free Ge NW-based composite electrodes fabricated via manual mixing with PAA as a binder, using lithium perchlorate as an electrolyte salt without electrolyte additives (white) and with VC (black). Structural formulas of the lithium perchlorate electrolyte salt and PAA binder are included for reference.

In an effort to better distinguish the different mechanisms of capacity retention that occur during cycling, differential capacity plots (Figure 5.6) from the devices shown in Figure 5.2 were analyzed to see how the electrochemical events in each composite changed over the course of 50 cycles for each electrolyte formulation. Negative values along the ordinate in these plots correspond to lithiation, sweeping the voltage from 1 to 0.01 V, while positive values along the ordinate correspond to delithiation as the potential is swept from 0.01 to 1 V. For all electrolyte formulations, there is a sharp peak during the first cycle, corresponding to a two-phase transition at 0.37 V associated with lithiation of crystalline Ge,[441,442] but this peak does not appear in subsequent cycles. As such, this initial feature is ascribed to the lithiation-induced amorphization of crystalline Ge. In all subsequent cycles, the lithiation of amorphous Ge (a-Ge) proceeds via three broad peaks at 0.55 V, 0.4 V, and 0.2 V, which are characteristic of amorphous Li_xGe_y. Delithiation of lithiated Ge exhibits a distinctive peak at ~0.5 V, which corresponds to the delithiation of crystalline $Li_{15}Ge_4$. In past work,[22] capacity retention in Ge NW electrodes has been primarily associated with preserved delithiation peak intensities at ~0.5 V as cycling proceeds.

Indeed, less efficient capacity retention was observed for devices that showed a decrease in this sharp delithiation peak following extended cycling. In addition, a broad delithiation shoulder centered near 0.4 V (e.g. Figure 5.6a) evolves over an increasing number of cycles for certain electrolyte compositions. Although this broad shoulder has not specifically been assigned previously for Ge alloying electrodes, by making an analogy to studies of silicon lithiation and delithiation,[443] we suggest that this feature corresponds to delithiation from amorphous domains of the active material (a-Li_xGe_y).

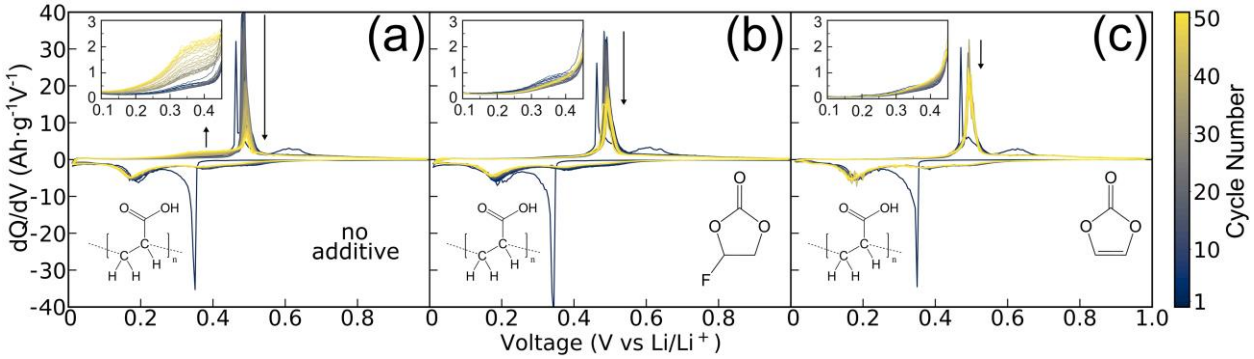

Figure 5.6. Total differential capacity plots of 1-octene hydrogermylated Ge NW composite electrodes fabricated via manual mixing that employ PAA as a binder, 1 M $LiPF_6$ in 1:1 w/w EC:DEC with (a) no electrolyte additive, (b) FEC additive included, and (c) VC additive included. The color scale at the rightmost side delineates the evolution of the differential capacity profile over the first 50 cycles for each device. Arrows highlight changes in peak intensity.

As can be seen from the plots in Figure 5.6, a comparison between the performance of Ge NW composite electrodes with different electrolyte additives demonstrates that the major lithiation and delithiation features of the total differential capacity plots are similar over the course of the first twenty cycles. However, the device without electrolyte additive (Figure 5.6a) shows a substantial decrease in the intensity of the sharp $Li_{15}Ge_4$ delithiation peak at ~0.5 V over extended cycling, along with the concomitant formation of the broad delithiation shoulder at ~0.4 V,

corresponding to delithiation from a-Li_xGe_y as discussed above. Interestingly, these additive-free devices maintain better capacity retention than devices that include the FEC additive (Figure 5.2d), despite the decrease in peak intensity at 0.5 V, likely due to the emergence of a-Li_xGe_y as an additional source of delithiation capacity to compensate for the loss of Faradaic activity from the crystalline $Li_{15}Ge_4$ phase.

Including electrolyte additives (Figure 5.6b and Figure 5.6c, corresponding to FEC and VC) suppresses the ability to delithiate from a-Li_xGe_y domains, as evidenced by the absence of the broad shoulder at ~0.4V over 50 cycles. Although the inclusion of FEC is often observed to result in improved capacity retention, it does not appear to be necessary for improving capacity retention in our hydrogermylated Ge NW-based devices (Figure 5.2d). Additionally, the three features associated with the lithiation of a-Ge for the additive-free and FEC-containing devices (Figure 5.6a and Figure 5.6b) shifted to slightly lower potentials, while including VC as an additive (Figure 5.6c) maintained the position of the original three a-Ge lithiation peaks; this behavior is consistent with results of fluorine-free devices as well (Figure 5.7a). Moreover, when VC was used as an additive (Figure 5.6c, Figure 5.7b), there was little change in the position or intensity of any peaks over the course of 50 cycles.

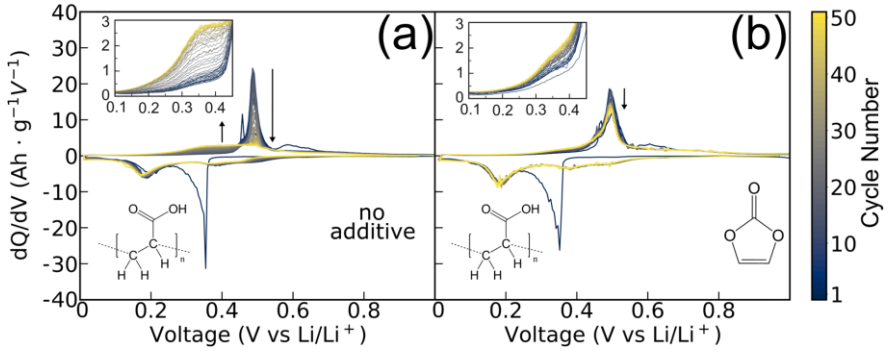

Figure 5.7. Total differential capacity plots of 1-octene hydrogermylated germanium nanowire composite electrodes that employ PAA as a binder, and EC/DEC + 1M $LiClO_4$ as an electrolyte with (a) no electrolyte additive and (b) VC additive included. The color scale at the rightmost side delineates the evolution of the differential capacity profile over the first 50 cycles for each device. Arrows highlight changes in peak intensity.

Furthermore, when VC was included, the crystalline $Li_{15}Ge_4$ delithiation peak at 0.5 V decreased the least out of the three device architectures (Figure 5.6c). Although including VC resulted in the best performing devices, it is clear from the differences between the additive-free and FEC-containing devices (Figure 5.6a and Figure 5.6b), in context with their capacity retention (Figure 5.2d), that overall capacity retention cannot be attributed to a single morphological habit (i.e. crystalline or amorphous domains of the active material). The device without any electrolyte additive (Figure 5.6a) leads us to believe that functionalizing the active material interface produces an SEI that minimizes the loss of capacity retention as compared to the unfunctionalized surfaces cited in this manuscript.

Importantly, the mechanical characteristics of binders can also affect composite electrode stability. Although this study focused on the use of PAA as a binder material, the highly fluorinated PVDF binder system is one of the most widely used polymeric binders for alloying electrode materials, including Ge NW composites.[22,23] Nonetheless, PAA has recently been implemented for silicon-based composite electrodes, with high capacity retention upon extended cycling.[444,445] The

impressive performance of PAA composites has been attributed to the large elastic modulus of PAA,[446] hydrogen bonding of the carboxylate groups with native surface oxide present on silicon electrode materials,[414,447] decreased swelling due to decreased electrolyte uptake,[448] and higher adhesion strength with the copper current collector.[449] However, most of these previous studies utilized alloying electrode materials containing surface oxide coatings. Because the Ge NW surfaces employed in this study have been functionalized in situ with an alkane monolayer to prevent surface oxidation, the observed benefits of using PAA as a binder largely appear to be due to its superior mechanical characteristics, such as the ability to withstand high strain from volume expansion of the active material and improved adhesion to the current collector, as opposed to chemical characteristics such as hydrogen bonding of the PAA carboxylate groups with an oxidized active material surface.

5.3.4 *The role of electrode fabrication processing on hydrogermylated Ge nanowire-based electrode performance*

Since polymeric binders are known to influence the mechanical stability and the SEI layer composition of composite electrodes,[24,413–415] we performed a direct comparison between the performance of PAA- (Figure 5.8b) and PVDF-based (Figure 5.8c) Ge NW composite electrodes. Importantly, we observed that the electrode processing technique chosen to prepare the electrode slurry (Figure 5.8a) drastically affects the performance of the device depending on the binder that is being used. As such, we investigated the implementation of two commonly used processing techniques for each polymeric binder: (i) manual mixing with a mortar and pestle and (ii) magnetic stirring in a glass vial. To our knowledge, there has not been a comparison of electrode preparation techniques for these types of highly anisotropic, alloying negative electrode materials. We

demonstrate that choice of electrode processing technique is particularly critical for devices formulated using PVDF as a binder, and that magnetic stirring is overall a better choice for Ge NW-based composite electrode devices fabricated using either binder system. These results show that optimization of NW-based composite electrodes is highly dependent on slurry preparation, composite architecture, and careful selection of a polymeric binder. This highlights the importance of optimizing electrode processing methods for composite electrode systems.

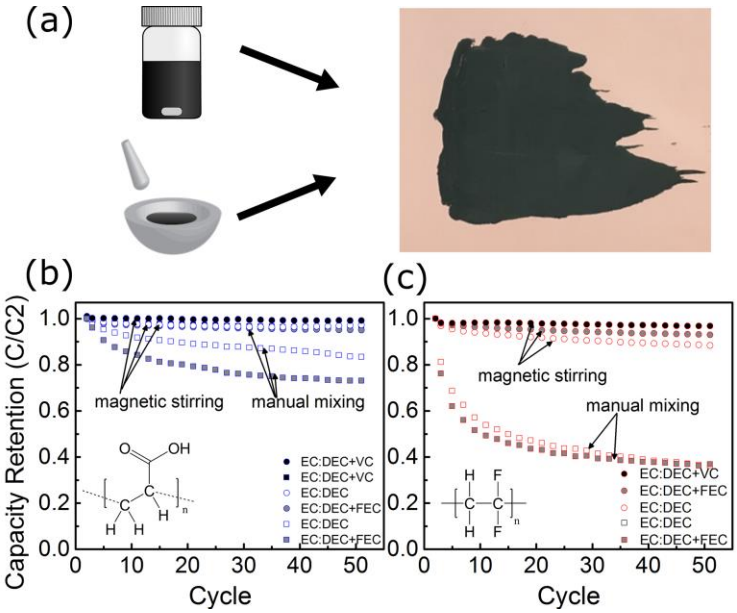

Figure 5.8. (a) Characteristic image of a Ge NW composite slurry (prepared via either magnetic stirring or manual mixing) doctor-bladed onto a copper foil. (b,c) Capacity retention of Ge NW-based electrodes using either (b) PAA or (c) PVDF as a binder, EC/DEC as the electrolyte, $LiPF_6$ as the electrolyte salt, and different electrolyte additives for the two different electrode processing techniques. Circles represent magnetically stirred electrode slurries, while squares represent manually mixed electrode slurries. White symbols correspond to no electrolyte additive, gray fill corresponds to the use of FEC as an additive, and black fill indicates the use of VC additive.

For PAA-based devices (Figure 5.8b), high capacity retention was achieved (>70%), irrespective of the electrode slurry preparation that was chosen, although magnetic stirring gave

rise to composites that exhibited much better overall capacity retention. We observe that magnetic stirring results in electrode composites with NWs whose morphology is largely maintained (Figure 5.1c), while the composite electrodes fabricated by manual mixing show Ge NWs with significantly shorter lengths (Figure 5.1b). The observed morphological differences between the resulting electrode composites, while somewhat subtle, are clearly impactful with respect to electrode performance, thus warranting further study in the future. This effect is exacerbated significantly when PVDF is used as a binder, with PVDF-based devices exhibiting extremely poor capacity retention (~40%) when manual mixing is used to process the NW composite electrodes. Despite the apparent superiority of magnetic stirring over manual mixing, it is important to note that it is much easier to create devices with identical active material mass loadings using manual mixing for PAA-based electrodes, likely due to the heterogeneity of the magnetically stirred PAA/NMP dispersion immediately prior to doctor-blading, resulting in varied active material loadings for cells punched from different regions of the current collector. NWs were observed to flocculate more readily under certain slurry mixing conditions, which may affect the assumed homogeneity of the doctor-bladed electrodes and ultimately impact the average areal mass loading of active material, which can affect the apparent specific capacity. In particular, slurries fabricated with PVDF under magnetic stirring remained well dispersed during deposition, whereas slurries fabricated with PAA under magnetic stirring showed signs of flocculation over time. This highlights the importance of optimizing stable dispersions of fiber-based active materials for slurry casting and electrode fabrication.[73] Nonetheless, all devices prepared using PAA exhibited robust specific capacities and capacity retention, irrespective of variations in the specific active material loading. The observed variations are likely due to differences in electrode slurry viscosity with the

different binders, and likely warrants further optimization of electrode slurry processing for highly anisotropic structures that are prone to flocculation in low viscosity solutions.[450]

Despite the inclusion of FEC, (Figure 5.8c, red outlined-gray squares), there was little improvement in capacity retention (36% vs. 37% capacity retention after 50 cycles) for PVDF-based devices prepared using manual mixing, to an extent that is similarly observed for the PAA-based devices (see Figure 5.2b and Figure 5.2d). However, previous investigations that have integrated these materials into composite electrodes have typically employed magnetically stirred electrode slurries,[22,23] and indeed, we found that when using PVDF as a binder, magnetically stirring the electrode slurry drastically improved the capacity retention of our devices (Figure 5.8c, red outlined circles), which is in agreement with previously published results. [22,23] Nonetheless, in our hydrogermylated Ge NW composite electrodes prepared via magnetic stirring with PVDF (Figure 5.8c), we did not see the same improvement upon addition of FEC that had been previously reported in other studies of analogously processed, unfunctionalized Ge NW composite electrodes.[22] This observation builds on a growing body of evidence that actively functionalizing the surface of electrode materials could reduce the need for fluorinated additives to achieve high capacity retention, especially in alloying electrode systems.[23,427] Certain electrode processing techniques can result in robust electrodes and capacity retention, irrespective of the electrolyte additives used, as seen in Figure 5.8, panels b and c, for both binders when prepared via magnetic stirring. Mechanical grinding via mortar and pestle may expose unpassivated, oxidized surfaces, where the formation of a robust SEI is more dependent on the presence of electrolyte additives, as has been observed previously.[22] Conversely, magnetically stirred electrodes maintain the integrity of the surface passivation and therefore do not require electrolyte additives for high capacity retention.

For completeness, we also extend the total differential capacity analysis to devices prepared via magnetic stirring in the presence and absence of electrolyte additives for both polymeric binder systems in Figure 5.9. All devices show similar electrochemical features, but the three broad peaks associated with the lithiation of a-Ge again shift to slightly lower potentials for the additive-free devices (Figure 5.9a and Figure 5.9d) and devices with FEC additive (Figure 5.9b and Figure 5.9e), which is similar to the observed shifts in manually mixed PAA devices (Figure 5.6a and Figure 5.6b). The devices with VC (Figure 5.9c and Figure 5.9e) maintain the same peak potentials for the lithiation of a-Ge throughout cycling, as before.

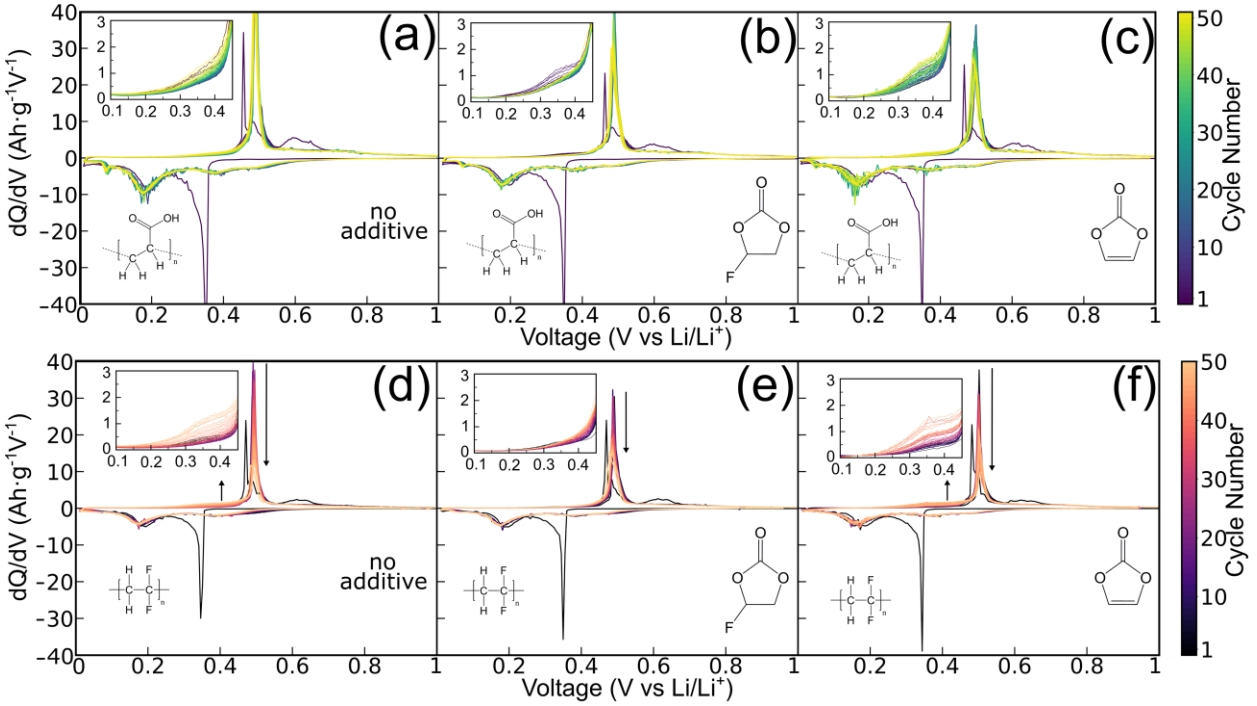

Figure 5.9. Total differential capacity plots of magnetically-stirred Ge NW composite electrode devices fabricated with EC/DEC electrolyte, $LiPF_6$ as the electrolyte salt, (a-c) PAA or (d-f) PVDF as the binder, and a range of electrolyte additives (a, d) no additive (b, e) FEC additive and (c, f) VC additive. The color scales at the rightmost side delineate the evolution of the differential capacity profile over the first 50 cycles for each device. Arrows highlight changes in peak intensity.

Notably, all Ge NW-based PVDF devices that were prepared by magnetically stirring (Figure 5.9d–f) showed a decrease in the magnitude of the c-$Li_{15}Ge_4$ delithiation feature at 0.5 V, with Figure 5.9e displaying a slight shift of this peak to lower potentials as the electrode is cycled. In addition, PVDF-based devices with VC and without additive (Figure 5.9d,f) show the gradual appearance of the broad shoulder at 0.4 V discussed previously, indicative of delithiation from a-Li_xGe_y. This suggests that including VC as an electrolyte additive enables access to the delithiation of a-Li_xGe_y for PVDF devices as an additional source of capacity. Including VC in this composite architecture does not completely suppress the evolution of the broad shoulder at 0.4 V, even though the crystalline delithiation peak at 0.5 V does not decrease as dramatically as it does when electrolyte additives are absent. This indicates that formulations which enable the amorphous delithiation transition (0.4 V), while also maintaining the crystalline delithiation peak (0.5 V) could help to improve the cycle life of these high-capacity composite alloying electrodes.

5.4 CONCLUSION

We demonstrate that high-capacity composite alloying electrodes formulated with unoxidized, 1-octene hydrogermylated Ge NWs do not require commonly used fluorinated additives, such as FEC, in order to maintain robust capacity retention. Devices with controlled surface chemistry fabricated in the complete absence of fluorinated compounds consistently demonstrated among the best capacity retention and overall performance, while the inclusion of FEC often led to decreased capacity retention. In contrast, reductive decomposition of the nonfluorinated VC additive led to consistently superior device characteristics. Total differential capacity plots showed delithiation from a-Li_xGe_y as an additional source of capacity for some cell architectures, with the beneficial characteristics of the PAA binder being attributed to its intrinsic mechanical properties, rather than

its ability to hydrogen bond with native surface oxides. In addition, we demonstrate that although both PAA and PVDF can be used as binders for Ge NW-based composite electrodes, the resultant device characteristics are highly dependent on the electrode processing technique that is chosen, particularly for PVDF-based devices. While the mass loading of electrodes containing PVDF as a binder is higher than those containing PAA (by 0.2 mg/cm^2), the substantial difference in cycling performance and differential capacity profiles between composites fabricated via magnetic stirring and mechanical mixing did not appear to affect the capacity retention based on our initial device optimization data. We therefore conclude that the selection of composite processing conditions can be as significant as the electrolyte additive. Further comparisons between mass loading in full-cell format, additive concentration, and charge/discharge rates will be of interest to pursue in future studies. Most importantly, we demonstrate that FEC is not necessary to achieve robust capacity retention in high-capacity alloying electrodes, as long as the active material surface chemistry is carefully controlled. These results suggest that actively controlling chemical functionalization of the electrode surface of the active material in nanostructured electrode composites may be a general tool for controlling the active material/bind interactions that influence cycle life in next-generation high capacity alloying electrodes. Additionally, our results suggest that standardizing composite preparation methods may be critical for directly comparing the merits of new nanostructured composite formulations.

Chapter 6. SUPERCRITICAL FLUID-BASED SYNTHESIS OF ALLOYED GROUP IV NANOWIRES

The work presented in this chapter is the result of a collaborative project within the Holmberg lab. Ge Gu has contributed significant efforts toward the development of a supercritical fluid-based synthesis of $Si_{1-x}Ge_x$ nanowires.

6.1 INTRODUCTION

In an effort to improve the energy density of lithium ion batteries, materials such as silicon and germanium have gained interest as negative electrode active materials as replacements for graphite. Silicon has the highest theoretical gravimetric capacity for negative electrode materials (3579 mAh/g at room temperature) and is a plentiful element, which has resulted in an explosion of research dedicated to developing silicon-based electrodes for lithium ion batteries over the last few decades.[20,235,236,251,413,425,451,452] Recently, a number of companies and startups have directed efforts to improve lithium-ion battery energy density through the development of silicon-based electrodes for lithium ion batteries, including Tesla, Global Graphene Group, Ecellix, Sila Nanotechnologies, Group14 Technologies, Advano, and Enevate. Despite silicon's apparent unique advantages, it is ultimately limited in its ability to withstand cycling at fast charge and discharge rates.[237] Germanium has the second highest theoretical gravimetric capacity for lithium (1384 mAh/g at room temperature) and, although it is more expensive than silicon, germanium has demonstrated a significantly greater rate capability, tolerating a charge/discharge cycle of twelve minutes, with only a marginal decrease in capacity.[78,234,237,252]

Although the study of silicon and germanium as individual materials is important for battery electrodes, the study of alloyed silicon and germanium ($Si_{1-x}Ge_x$) is a nascent field for

lithium ion batteries. One recent strategy to incorporate these two materials into an electrode material was to grow branched silicon nanowires from germanium nanowires, creating an novel heterostructure, capable of reaching high capacity as well as high rate capability, depending on the Si:Ge atomic ratio incorporated.[453] Another strategy, glancing angle deposition (GLAD), was used to create nanostructured alloyed $Si_{1-x}Ge_x$ film electrodes, which exhibited tunable gravimetric capacity and rate capability as a function of the Si:Ge compositional ratio.[454] By increasing silicon content, high capacity was achieved; by increasing germanium content, rate capability was improved.[70,454] Incorporating a fraction of germanium into silicon to form an alloy is a promising strategy to improve the rate capability of high capacity alloying electrode materials, without increasing the cost significantly. Very recently, alloyed $Si_{1-x}Ge_x$ nanowires, with a range of silicon:germanium ratios, were grown directly from a tin-coated stainless steel current collector and tested as electrodes for lithium ion batteries, demonstrating tunable capacity and rate capability.[70]

When considering the structural architecture of electrodes that use nanowires for batteries, growing nanowires directly from the current collector promotes fast electron transport to the current collector. However, growing nanowires from a fixed number of metal seeds on a two-dimensional substrate limits the total mass loading of active material in the electrode. Furthermore, by growing nanowires from a metallic thin film, the reaction is limited to the volume of the metal nanocrystal seed on the substrate. By transferring this chemistry from a substrate-based growth to a colloidal synthesis, we would circumvent active material mass loading limitations when incorporating these materials into electrodes for lithium ion batteries, resulting in a potentially more scalable process for $Si_{1-x}Ge_x$ nanowire-based electrodes for lithium-ion batteries.

Here, we report the colloidal, supercritical fluid-based synthesis of tin-seeded $Si_{1-x}Ge_x$ alloy nanowires. To our knowledge, this is the first demonstration of using supercritical fluid-based techniques to produce alloyed semiconductor nanowires.

6.2 EXPERIMENTAL DETAILS

6.2.1 *Materials*

Tin (II) chloride ($SnCl_2$, anhydrous, ≥99.99% trace metals basis), oleylamine (90%), lithium bis(trimethylsilyl)amide (97%), superhydride solution (1.0 M lithium triethylborohydride in tetrahydrofuran), oleic acid (degassed, 90%), toluene (anhydrous, 99.8%), and ethanol (anhydrous, ≤0.005% water) were purchased from Sigma-Aldrich. Chloroform (HPLC grade, 99.9%), ethanol (100%), and toluene (≥99.5%) were purchased from Fisher. Monophenylsilane (>95%) and triphenylgermane (>95%) were purchased from Gelest.

6.2.2 *Tin nanocrystal synthesis*

Tin nanocrystals were prepared based on the procedure outlined by He, *et al*.[308] To a 100 mL three-neck round-bottom flask, $SnCl_2$ (7.8×10^{-1} mmol) was combined with oleylamine (24.6 mL). The flask was purged of air for five minutes on the Schlenk line while stirring at 1500 RPM. The mixture underwent a cycling process between vacuum and nitrogen three times. Under nitrogen, the mixture was heated to 140°C, whereupon vacuum was pulled for two hours. In the glovebox, a solution of lithium bis(trimethylsilyl)amide (3.6 mmol) in toluene (2 mL) was prepared and loaded into a syringe. Additionally, 0.6 mL of the superhydride solution was loaded into a syringe. The flask was blanketed with nitrogen and heated to 180°C. The lithium bis(trimethylsilyl)amide

solution was injected first. After ten seconds, the superhydride solution was injected. The reaction ran at 180°C for one hour, after which it was removed from heat. At 120°C, 10 mL of anhydrous toluene was injected, and the flask was cooled rapidly by being submerged in an ice bath. The flask was transferred to the glove box, which is where all nanocrystal handling was performed. To the nanocrystal dispersion, 40 mL of anhydrous ethanol were added, and the nanocrystals were centrifuged at 3885 RPM for 10 minutes for precipitation. The supernatant was discarded, and the nanocrystals were redispersed in 5 mL of anhydrous toluene. 1 mL oleic acid (degassed) was added to stabilize nanocrystals. The washing procedure was repeated with 10 mL of anhydrous ethanol, whereupon after centrifugation, the precipitated nanocrystals were redispersed in 4 mL of anhydrous toluene. Tin nanocrystals were stored in a nitrogen-filled glovebox to prevent oxidation.

6.2.3 *Supercritical fluid-based synthesis of Sn-seeded $Si_{1-x}Ge_x$ nanowires*

$Si_{1-x}Ge_x$ nanowires were synthesized via SFLS-based growth, using tin nanocrystals as seeds. In a typical reaction to synthesize $Si_{1-x}Ge_x$ nanowires, a cylindrical 10-mL titanium reaction vessel was transferred into a nitrogen atmosphere, sealed, and placed in a heating block at 480°C. While keeping the exit valve closed, anhydrous toluene was introduced to the reactor, pressurizing the reactor to 900 psig. A nanowire precursor mixture containing 0.32 mg/mL Sn nanocrystals, 1.3×10^{-2} M triphenylgermane, and 2.2×10^{-1} M monophenylsilane (1:6:52 Sn:Ge:Si molar ratio) was prepared in anhydrous toluene. The precursor solution was loaded into a 10 mL injection coil and subsequently injected into the pre-heated and pre-pressurized reactor for twenty minutes at a rate of 0.5 mL/min. After injection of the nanowire growth solution, the inlet and exit valves were closed and the reactor was cooled to room temperature. Nanowires were collected with toluene

and then washed three times in glass vials for further characterization with a 2:2:1 ratio of toluene:chloroform:ethanol, and centrifuged at 2355 RCF for ten minutes.

6.2.4 *Materials characterization*

Transmission electron microscopy (TEM) images were acquired with a FEI Technai G2 F20 Supertwin TEM, operating at 200 kV. Digital Micrograph software was used to generate Fast Fourier Transforms (FFTs) of high-resolution TEM images. Scanning electron microscopy (SEM) images and energy-dispersive X-ray spectroscopy (EDXS) were acquired with a FEI Sirion XL30 SEM operating at 5kV for imaging and 10kV for EDXS acquisition. Samples for SEM-EDX were prepared on aluminum foil, rather than on silicon substrates. Raman spectra were collected with a Thermo Scientific DXR2 Raman microscope, using an excitation wavelength of 532 nm at a power of 5mW for one minute. X-ray diffraction (XRD) scans were collected using a Bruker D8 Discover equipped with an IμS 2-D XRD detector system and were analyzed using EVA software. Inductively coupled plasma optical emission spectroscopy (ICP-OES) was performed with a Perkin Elmer Optima 8300 spectrophotometer.

6.3 RESULTS AND DISCUSSION

6.3.1 *Demonstration of tin-seeded $Si_{1-x}Ge_x$ nanowires*

The supercritical fluid-based synthesis of alloyed $Si_{1-x}Ge_x$ nanowires involved continuous injection of a nanowire precursor solution—consisting of tin nanocrystals, monophenylsilane, and triphenylgermane—into a pre-heated and pre-pressurized reactor. Figure 6.1a and Figure 6.1b shows TEM of the tin nanocrystals used for the synthesis of supercritical fluid-based synthesis of

$Si_{1-x}Ge_x$ nanowires. XRD data of the nanocrystals (Figure 6.1c) confirms that they are composed of tin.

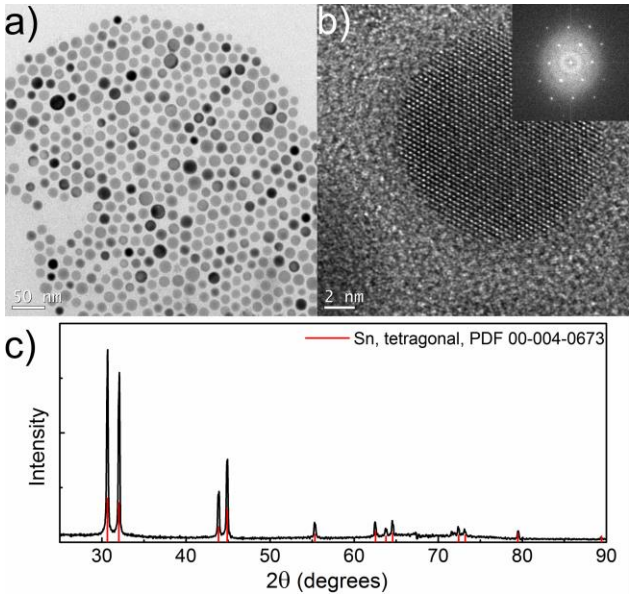

Figure 6.1. (a) Low resolution TEM and (b) high-resolution TEM of tin nanocrystals used as seeds for the supercritical fluid-based growth of $Si_{1-x}Ge_x$ nanowires. (c) XRD of tin nanocrystals (Sn PDF: 00-004-0673).

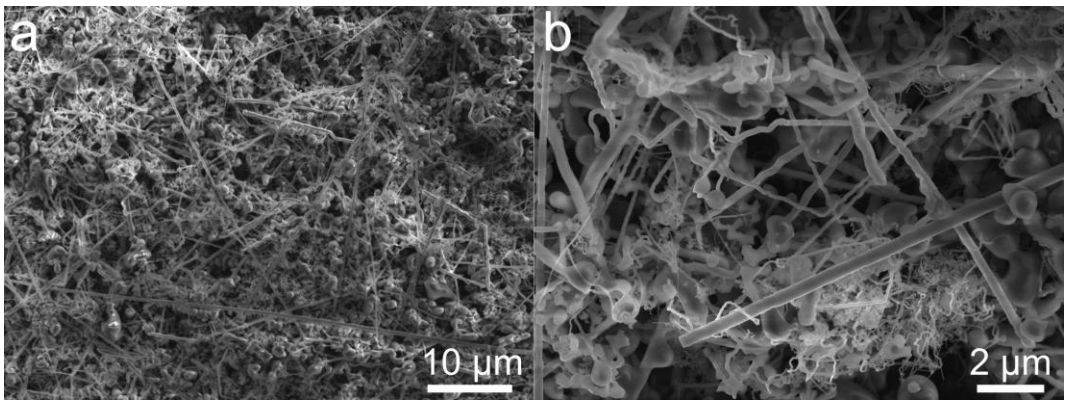

Figure 6.2. (a) Low magnification SEM of tin-seeded $Si_{1-x}Ge_x$ nanowires and (b) high magnification SEM image of tin-seeded $Si_{1-x}Ge_x$ nanowires.

Figure 6.2a and Figure 6.2b show SEM images of the tin-seeded $Si_{1-x}Ge_x$ nanowires. $Si_{1-x}Ge_x$ nanowire diameters range from 25 nm to 420 nm and $Si_{1-x}Ge_x$ nanowire lengths can reach

over 60 μm. The product of the supercritical fluid-based synthesis of $Si_{1-x}Ge_x$ nanowires contained a mix of both straight and tortuous nanowires, as well as large isotropic particles.

6.3.2 *Evidence of $Si_{1-x}Ge_x$ alloying in nanowires*

Alloying of silicon and germanium was confirmed through both Raman scattering (Figure 6.3), XRD (Figure 6.4), and SEM-EDX (Figure 6.5). Raman scattering of $Si_{1-x}Ge_x$ nanowires (Figure 6.3) shows three prominent features, representative of the Ge-Ge, Si-Ge, and Si-Si bands. A downshift is expected for both the Ge-Ge and Si-Si bands of $Si_{1-x}Ge_x$ alloys, compared to pure Ge (305 cm^{-1}) or Si (520 cm^{-1}),[455] which is reflected in the Raman data (Figure 6.3). In particular, the Si-Si band has been shown to downshift linearly with increasing Ge composition, enabling the estimation of the $Si_{1-x}Ge_x$ nanowire composition calculated from the Si-Si peak position.[455] Based on the peak position (~488 cm^{-1}) of the Si-Si feature in Figure 6.3, the nanowire composition was estimated to be $Si_{0.5}Ge_{0.5}$.

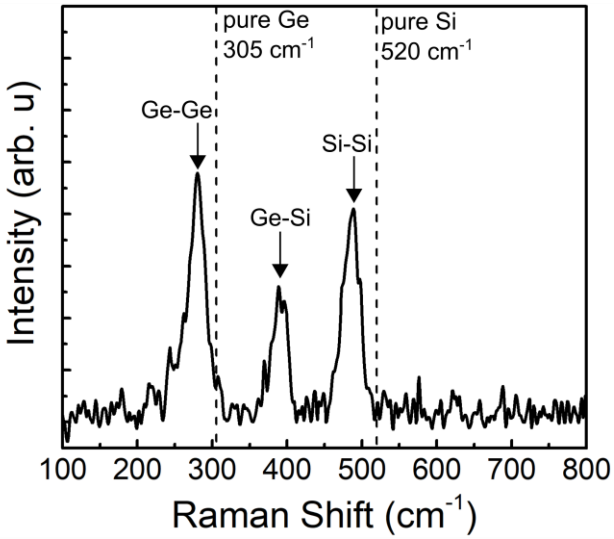

Figure 6.3. Raman scattering of tin-seeded $Si_{1-x}Ge_x$ ($Si_{0.5}Ge_{0.5}$) nanowires synthesized through a supercritical fluid-based synthesis. Dashed lines are representative of band positions for pure germanium (305 cm^{-1}) and pure silicon (520 cm^{-1}).

The (111) reflection in the XRD data (Figure 6.4) also indicates successful growth of alloyed $Si_{1-x}Ge_x$. Based on the powder diffraction files (Ge: 00-004-0545, Si: 00-005-0565), the (111) reflections for germanium and silicon are located at 27.28° and 28.42°, respectively. It's been demonstrated that the angle of the (111) reflection of the $Si_{1-x}Ge_x$ system increases linearly with increasing silicon content.[456] The XRD peak position of $Si_{1-x}Ge_x$ nanowires in Figure 6.3 is located at 27.8, corresponding to a d-spacing of 3.2 Å, which is halfway between the d-spacing of silicon (3.14 Å) and germanium (3.26 Å) for the (111) reflection, validating the approximate $Si_{0.5}Ge_{0.5}$ composition estimated from the Raman downshift of the Si-Si peak.

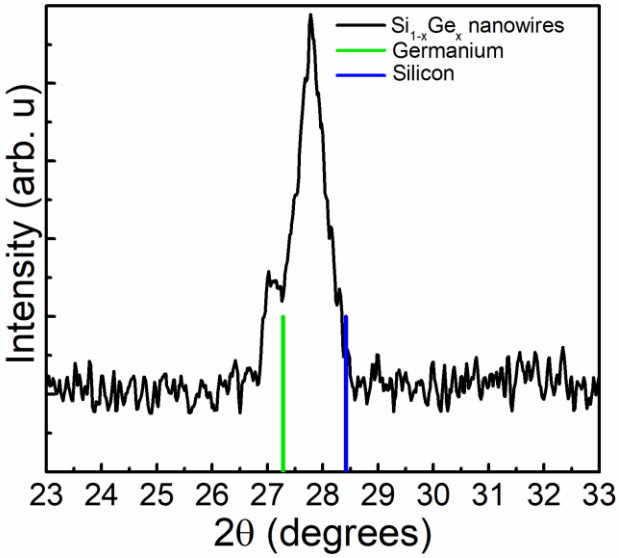

Figure 6.4. X-Ray diffraction data of $Si_{1-x}Ge_x$ nanowires is represented by the black curve, highlighting the (111) reflection. The (111) reflection of germanium and silicon from the powder diffraction files are represented as green and blue lines, respectively. Germanium PDF 00-004-0545, Silicon PDF 00-005-0565.

SEM-EDX (Figure 6.5) was collected to investigate the distribution of silicon and germanium throughout the sample. SEM-EDX mapping displays a fairly homogeneous distribution of both germanium and silicon throughout the supercritical fluid-grown $Si_{1-x}Ge_x$ nanowires. Interestingly, the Si:Ge ratio extracted from SEM-EDX is 2:1 (Figure 6.5h), which

differs from the calculated 1:1 Si:Ge ratio from Raman and XRD peak shifts. In previous work, when phenylsilane was used as a precursor for supercritical fluid-based silicon nanowire synthesis, the resulting nanowires typically had an amorphous poly(phenylsilane) coating on the nanowire surface as a byproduct of the phenylsilane disproportionation reaction.[21,67] In addition, the reaction temperature has been shown to influence the thickness of the amorphous coating, with increased reaction temperatures resulting in thicker coatings.[67] The discrepancy between the high Si:Ge ratio measured from SEM-EDX, compared to the calculated ratio from XRD and Raman, could be due to the presence of an amorphous poly(phenylsilane) coating, which could contribute to the higher silicon signal in SEM-EDX; however, because the amorphous poly(phenylsilane) coating is not incorporated into the crystalline nanowire, it does not contribute to alloying and therefore does not contribute to shifts in the XRD peaks or Raman bands.

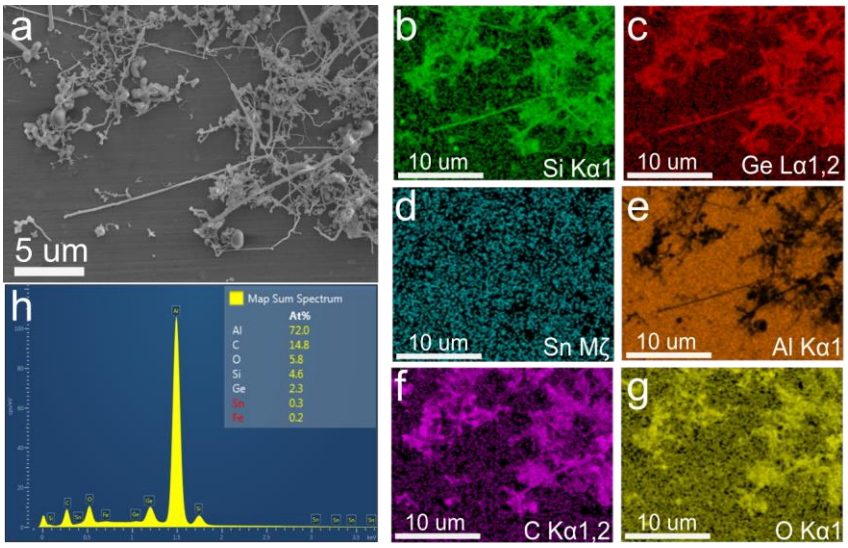

Figure 6.5. (a) SEM image of the $Si_{1-x}Ge_x$ nanowires. (b-g) Layered EDX maps corresponding to (b) the $Si_{1-x}Ge_x$ nanowires (h) EDX quantitative map and atomic ratio of elements.

6.3.3 *The role of precursor decomposition kinetics*

Alloyed $Si_{1-x}Ge_x$ nanowires were synthesized by balancing precursor decomposition kinetics and selecting a metal nanocrystal that forms a ternary alloy with silicon and germanium. Although both triphenylgermane and monophenylsilane undergo disproportionation reactions, the reactivity of aryl-germane precursors is much higher than aryl-silanes.[108] Notably, the degree of phenyl substitutions was used to balance disproportionation reaction rates. Here, the decomposition kinetics of triphenylgermane and monophenylsilane match more closely than if both precursors had the same degree of phenyl substitutions, resulting in improved balanced kinetics and transport to the tin seed.[108]

Similar to Stokes, *et al*,[70] we attribute the synthesis of $Si_{1-x}Ge_x$ nanowires to the high molar ratio of monophenylsilane to triphenylgermane. Previously, the high temperatures required for aryl-silane decomposition have been capitalized on by using monophenylsilane as a phenyl sink during the disproportionation of diphenylgermane, improving the yield and morphology of nickel-seeded germanium nanowires, while limiting silicon incorporation to less than 0.6 atomic percent.[457] In this work, under conditions with an increased ratio of monophenylsilane to triphenylgermane (52:6) and an increased reaction temperature, the monophenylsilane is able provides a sufficient supply of silicon semiconductor atoms for incorporation of silicon into $Si_{1-x}Ge_x$ nanowires.

The presence of $Si_{1-x}Ge_x$ nanowires is also accompanied by large, isotropic particles that are interspersed with nanowires in Figure 6.2. Homogeneous nucleation is responsible for the formation of such isotropic particles and occurs when the decomposition rate of the semiconductor precursor is faster than the rate of semiconductor atoms diffusing into the metal nanocrystal seed to facilitate anisotropic growth. Due to the sensitivity of the supercritical fluid-based nanowire

growth process to precursor decomposition kinetics,[108] careful tuning of precursor concentrations, precursor to seed ratios, and reaction temperature are required to minimize homogeneous nucleation of isotropic particles.

6.4 CONCLUSIONS

In summary, we have demonstrated the first example of alloyed group IV nanowires grown through a supercritical fluid-based process. Growth of alloyed $Si_{1-x}Ge_x$ nanowires was achieved by balancing reaction conditions such as the phenyl substitution of aryl-germanes and aryl-silanes, precursor ratios, metal seed to precursor ratios, and reaction temperature. Silicon-germanium alloying was validated through Raman spectroscopy and XRD; SEM-EDX confirmed nanowires were comprised of both silicon and germanium and also suggests that the $Si_{1-x}Ge_x$ nanowires are coated with an amorphous poly(phenylsilane) shell. While this work demonstrates significant strides towards increased compositional control through supercritical fluid-based syntheses, specifically for alloyed group IV nanowires, additional work will be required to achieve a product that consists of entirely $Si_{1-x}Ge_x$ nanowires without the presence of isotropic particles. This work is ongoing in the Holmberg lab and is focused on exploring the reaction parameter space to develop a high-yield supercritical fluid-based synthesis of primarily $Si_{1-x}Ge_x$ nanowires, with plans to eventually investigate the tunability of the silicon:germanium ratio of $Si_{1-x}Ge_x$ nanowires. After identifying reaction parameters to facilitate a tunable, supercritical fluid-based synthesis, $Si_{1-x}Ge_x$ nanowires will be tested as an electrode material for lithium ion batteries. Eventually, we intend to use galvanostatic intermittent titration technique (GITT) to evaluate how the lithium diffusion coefficients in $Si_{1-x}Ge_x$ nanowire-based electrodes changes as a function of $Si_{1-x}Ge_x$ composition.

Chapter 7. CONCLUSIONS AND FUTURE DIRECTIONS

7.1 CONCLUSIONS

7.1.1 *Laser-driven solution-liquid-solid growth of semiconductor nanowires*

Colloidal bismuth and indium nanocrystals were shown to reach very high temperatures (~190°C) under continuous-wave near-infrared irradiation through both experimental thermographic images as well as through numerical models. The overall temperature increases rapidly from a combination of photothermal heating and collective heating effects. Because the metal nanocrystals are dispersed freely in solution, rather than pinned to a substrate, the immediate volume surrounding the nanocrystal likely reaches very high temperatures due to Young-Laplace interfacial surface pressures, which prevents bubble nucleation. We leverage the high temperatures generated by irradiation of metal nanocrystal dispersions to drive decomposition of molecular semiconductor precursors and to subsequently drive diffusion of semiconductor atoms into the metal seed, thereby facilitating semiconductor nanowire growth through the SLS growth mechanism. In addition to using typical molecular semiconductor precursors for nanowire growth, we have shown that magic-sized indium phosphides clusters can also be used as precursors for semiconductor nanowire growth. Using doped magic-sized clusters as precursors for nanowire growth could represent a new strategy to homogeneously dope semiconductor nanowires, furthering our compositional control over semiconductor nanowires and their electronic and optical properties.

Importantly, we also show that this contact-free, laser-driven nanowire growth process can be performed on the benchtop in any optically accessible, chemically resistant reactor, without the need for high-temperature or extreme-pressure equipment. Moreover, solution-based photothermal

nanowire growth can be translated from a batch reaction to a continuous-flow reaction, which could enable rapid combinatorial synthesis and characterization in the future. Further optimization of this optically driven nanowire growth process could facilitate a suite of opportunities, including solution-based growth of systems at bulk atmospheric conditions that currently require alternative growth methods due to solvent boiling point limitations.

7.1.2 *Growth dynamics of colloidal, solution-liquid-solid semiconductor nanowires*

The ability to perform laser-driven SLS semiconductor nanowire growth in an optically interrogable container was leveraged to investigate *in situ* growth dynamics of semiconductor nanowires. In particular, ultra-small-angle X-ray scattering was used to monitor colloidal, solution-based bismuth-seeded cadmium selenide nanowire growth dynamics over time. The increased invariant during irradiation indicated that a reaction was occurred to produce solid cadmium selenide. The change in the USAXS profiles at low q indicated the formation of large networks, or fractals, of cadmium selenide nanowires. Although the initial and final time points were fit using models, tracking nanowire growth dynamics via model fits proved to be extremely difficult due to the complexity of the system. Instead, the invariant, which is related to the total volume fraction, was used to track nanowire growth dynamics.

We observed that laser-driven nanowire growth is dependent on the bismuth nanocrystal number density as well as irradiance. From the invariant, we calculated a change in volume fraction over time, enabling extraction of physical parameters, such as nanowire lengths over time. This represents one of the first *in situ* characterizations of colloidal SLS-grown semiconductor nanowires. The combination of laser-driven growth and USAXS characterization could be applied to other metal-semiconductor nanowire systems, furthering our understanding of photothermally-

driven solution-based nanowire growth dynamics. In addition, we demonstrated on-demand, step-wise nanowire growth simply by turning the incident irradiation on and off. This type of on-demand synthesis demonstrates a new handle to control colloidal, solution-based semiconductor nanowire growth. Improving control over solution-based semiconductor nanowire growth rates could open possibilities for the production of colloidal, complex heterostructured nanowires.

7.1.3 *Assembly of semiconductor nanowires into hierarchical structures*

Optical traps have proven to be a useful tool for manipulating nanomaterials. Although optical trapping has conventionally been performed in water, the trapping medium has now been extended to high boiling point organic solvents such as squalane. Operating an optical trap in an organic solvent facilitates the generation of higher local temperatures upon trapping compared to aqueous systems due to the decreased thermal conductivity of the solvent. In addition, many inorganic colloidal nanomaterials are capped with polar ligands due to the chemistries required for their production. Optical trapping in organic solvents therefore broadens the scope of accessible temperature ranges and chemistries for optical trapping experiments.

In this work, an optical trap was used to manipulate bismuth-seeded semiconductor nanowires in squalane. The radiation pressure from the optical trap exerted in an optical torque that preferentially oriented the bismuth nanocrystal away from the laser and accelerated the nanowire to align with the previously trapped and aligned nanowire. Both DDA and experimental data show radiation pressure-induced nanowire alignment with the bismuth seed away from the laser source. When the accelerating nanowire approached the optical trap, the bismuth nanocrystal tip was photothermally-heated and melted to form a liquid droplet. Eventually, the gradient forces slowed the acceleration of the incoming nanowire and allowed for the molten bismuth tip to contact

the end of the previously trapped nanowire, resulting in a fused periodic heterostructure. This was repeated iteratively to manufacture a periodic bismuth nanocrystal-germanium nanowire heterostructure.

7.1.4 *Germanium nanowire battery electrodes with engineered surface binder interactions for improved cycle life and high energy density without fluorinated additives*

Semiconductor nanowires, especially silicon and germanium, have shown great promise as negative electrode materials for lithium ion batteries. Electrolyte additives are often necessary to improve the cycling stability of nanostructured silicon and germanium electrodes; however, composite alloying electrodes formulated with unoxidized, 1-octene hydrogermylated germanium nanowires do not require commonly used fluorinated additives, such as FEC, in order to maintain robust capacity retention. Devices with controlled surface chemistry tested in the complete absence of fluorinated compounds consistently demonstrated good capacity retention and overall performance, whereas the inclusion of FEC resulted in decreased capacity retention. In contrast, a nonfluorinated electrolyte additive, VC, resulted in consistently superior device performance with surface functionalized germanium nanowire composite electrodes. Total differential capacity analysis showed that delithiation from a-Li_xGe_y can act as an additional source of capacity for some cell architectures rather than as exclusively a sign of capacity fade, especially if delithiation from c-$Li_{15}Ge_4$ is maintained.

Moreover, unoxidized, surface functionalized germanium nanowires reveal that the beneficial characteristics of PAA as a binder are attributed to its intrinsic mechanical properties, rather than its ability to form hydrogen bonds with native surface oxides. Although both PAA and PVDF can both be used as binders for semiconductor nanowire-based composite electrodes, the resultant device characteristics are highly dependent on the electrode processing technique that is

chosen, particularly for devices that use PVDF as a binder. The selection of composite electrode processing conditions can play an equally significant role as the selection of electrolyte additives, especially for highly anisotropic nanomaterials.

Controlling chemical functionalization of the active material surface in nanostructured composite electrode may be a beneficial tool to control the active material/binding interactions that influence cycle life in next-generation high capacity alloying electrodes. Additionally, our results suggest that standardizing composite preparation methods will be critical for directly comparing the merits of new nanostructured composite formulations.

7.1.5 *Supercritical fluid-based synthesis of alloyed group IV nanowires*

Alloyed group IV nanowires were grown through supercritical fluid-based processes, demonstrating enhanced compositional control over supercritical fluid-based semiconductor nanowire growth. Growth of alloyed $Si_{1-x}Ge_x$ nanowires was achieved by balancing reaction conditions such as the phenyl substitution of aryl-germanes and aryl-silanes, precursor ratios, metal seed to precursor ratios, and reaction temperature. The presence of a silicon-germanium alloy was validated through Raman spectroscopy and XRD; SEM-EDX confirmed that nanowires were comprised of both silicon and germanium. While this work demonstrates significant strides towards the supercritical fluid-based synthesis of alloyed group IV nanowires, additional work will be required to achieve a product that consists of primarily $Si_{1-x}Ge_x$ nanowires, without isotropic particles. This work is ongoing and is focused on developing a high-yield supercritical fluid-based synthesis of $Si_{1-x}Ge_x$ nanowires, eventually investigating the ability to tune the silicon:germanium ratio of $Si_{1-x}Ge_x$ nanowires via supercritical fluid-based processes. The development of a highly scalable $Si_{1-x}Ge_x$ synthesis with tunable composition could produce materials for a range of

applications that may require different performance characteristics, such as high rate capability. Moreover, because supercritical fluid-based nanowire growth is particularly sensitive to precursor kinetics, it will be critical to balance precursor decomposition rates in order to develop additional complex nanowire compositions through the supercritical fluid-based process.

7.2 FUTURE DIRECTIONS

In the future, nanowires are well-positioned to address technological issues for a range of applications. Solution-based processes, such as SLS and SFLS nanowire growth, offer strategies to circumvent cost-limitations because solution processes are generally more readily scalable and can produce a high yield of nanowires, compared to vapor-based processes. However, it will be important to continue developing a deeper understanding of solution-based nanowire growth dynamics; improve compositional control and complexity of solution-grown nanowires; innovate methods to assemble solution-grown nanowires over both small and large length scales; and understand how different aspects of nanowires, such as surface chemistry, lithium ion transport, and adhesion to the current collector, can affect the performance of semiconductor nanowires as alloying electrodes for lithium ion batteries. The work in this dissertation has addressed aspects of these challenges, and in some cases, has developed platforms to enable further studies. However, there remain important challenges associated with each of these areas of research which will require additional research.

7.2.1 *Laser-driven solution-liquid-solid growth of semiconductor nanowires*

The development of laser-driven, colloidal, SLS nanowire growth presented in this thesis will provide a unique opportunity to address some of the challenges highlighted above. However, there

are many ways in which this particular paradigm of semiconductor nanowire growth could be further optimized, expanded, and studied. For example, matching the peak nanocrystal absorption with the laser wavelength would likely result in much more efficient photothermal transduction, thereby making the overall process much more cost-effective as well as more accessible to labs that do not have access to high-power near infrared lasers.

In addition, by lifting the conventional equipment requirements for semiconductor nanowire growth and enabling the reaction to occur in any chemically resistant, optically interrogable reactor, the opportunities to monitor solution-based semiconductor nanowire growth have been expanded. While ultra-small-X-ray scattering was uniquely beneficial to monitor changes in nanowire length dimensions, additional characterization methods such as Raman spectroscopy, photoluminescence spectroscopy, or absorption spectroscopy, could be used *in situ* to monitor laser-driven solution-based nanowire growth, potentially revealing additional insights of this new paradigm of SLS semiconductor nanowire growth. Notably, the ability to controllably start and stop nanowire growth simply by tuning the incident power provides the opportunity to study solution-phase chemistry at different stages of growth.

While it is evident that both the number density and the incident power influence laser-driven solution-liquid-solid nanowire growth, investigating the effect of nanocrystal size and composition on semiconductor nanowire growth rates could be a particularly interesting parameter to explore. The photothermal transduction efficiencies of metal nanocrystals could be tuned by adjusting the optical properties of metal nanocrystals, which can be modified through nanocrystal size and composition. In addition, because semiconductor nanowire growth rates are influenced by the nanowire diameter,[83,458,459] adjusting the nanocrystal seed size could potentially be leveraged to regulate nanowire growth rates.

Laser-driven, colloidal solution-liquid-solid nanowire growth has also been demonstrated in a continuous-flow reaction configuration, potentially enabling high-throughput material screening and rapid iteration to identify optimal experimental parameters. A high-throughput, continuous-flow setup for solution-based nanowire growth, paired with *in situ* spectroscopies offers the potential to rapidly scan a range of material systems, chemistries, concentrations, and other reaction parameters while simultaneously collecting material characterization information within a single experiment. Notably, this extends the opportunities to monitor *in situ* colloidal, solution-based nanowire growth of an ensemble of nanowires. However, the ability to optically trap metal-seeded semiconductor nanowires in high boiling point solvents could potentially be used to study single-particle dynamics of solution-based metal-seeded semiconductor nanowire growth. For example, *in situ* Raman spectroscopy of single nanowire growth dynamics could be used to identify melting characteristics of the nanocrystal seed as it transitions to an alloy droplet, as well as to study nucleation kinetics as the semiconductor atoms precipitate from the alloy droplet. By combining information from single-particle dynamics with information from the ensemble-nanowire dynamics, we may develop a deeper understanding of the laser-driven solution-liquid solid growth mechanism. These studies may also inform solution-based semiconductor nanowire growth more generally.

7.2.2 *Improving compositional complexity of solution-grown semiconductor nanowires*

Understanding the effects that various reaction conditions can have on solution-based nanowire growth will be important to improve our ability to produce compositionally complex, desirable materials. For example, laser-driven solution-liquid-solid nanowire growth may be able to facilitate the growth of axial heterostructures in solution if combined with carefully chosen precursors with sufficiently distinct decomposition kinetics. The laser power could potentially be

used as a handle to control the temperature of the reaction volume and rapidly alternate between the growth of two semiconductors, thereby producing axially heterostructured semiconductor nanowires.

In addition, because solution-based methods are highly sensitive to precursor decomposition kinetics, investigation of precursors with a range of decomposition rates will be important for producing compositionally complex semiconductor nanowires with uniform composition, such as alloyed, or doped semiconductor nanowires. Similarly, precursor kinetics will play an important role in the solution-based production of nanowires with nonuniform compositions, such as heterostructured nanowires. If uniform, complex nanowire composition is desired yet separate precursor kinetics cannot be matched, the development and use of single-source precursors will be critical for the production of certain alloyed or doped semiconductor nanowires. In particular, doped magic-sized clusters may be particularly useful for the production of doped-semiconductor nanowire systems, for which separate precursors may have mismatched precursor kinetics.

7.2.3 *Assembling and aligning nanomaterials for device integration*

Solution-based, readily scalable production of semiconductor nanowires will be important in order to produce nanowires for their intended applications in a cost-effective manner. However, directing the location, orientation, and hierarchical structures of solution-grown semiconductor nanowires remains a critical obstacle in order for the full potential of these intriguing nanomaterials to be realized. Optical traps have proven to be a useful tool for nanomaterial manipulation into complex structures and orientations. By expanding the trapping medium for optical trapping to nonaqueous solvents, we have omitted the need to perform ligand exchanges to

enable dispersion in water. Moreover, using an optical trap to align and solder semiconductor nanowires in high boiling point solvents represents a strategy for producing deterministic junctions between nanomaterials. In the future, expanding the trapping media to low boiling point solvents such as hexane or toluene would reduce washing and purification steps, thereby enabling easy characterization of the nanosoldered heterojunctions through high resolution methods, such as TEM. More broadly, the assembly of metal seeded nanowires could be extended to creating complex heterostructures of periodic metal-semiconductor heterostructures with alternating semiconductor materials or alternating metal seeds. In the future, this alignment and soldering strategy should be explored for relevant quantum computing materials such as indium antimonide nanowires.

7.2.4 *Future directions of group IV nanowires for battery applications*

The supercritical fluid-based growth of semiconductor nanowires offers a particularly attractive route for the high-throughput, inexpensive synthesis of semiconductor nanowires such as silicon, germanium, or alloys like $Si_{1-x}Ge_x$, especially for battery applications. Given the impact of surface chemistry of group IV materials on battery performance, the nanowire surface chemistry should be considered when integrating semiconductor nanowires into devices. Capacity retention of semiconductor nanowire-based devices can be improved to a certain degree by incorporating electrolyte additives, which influences the solid-electrolyte interphase layer composition and the resulting SEI layer properties. While *ex situ* characterization of electrode materials has been widely used to characterize the SEI layer composition, electrode morphology after extended cycling, and lithiated state of silicon/germanium anodes, *ex situ* characterization techniques fail to provide information about materials of interest while under operating conditions. Over recent years, the

development and accessibility of *in operando* characterization techniques, such as XRD, XAS, SEM, TEM, AFM, Raman, and FTIR, have greatly improved our understanding of the highly dynamic processes that occur during battery operation.[460] Moving forward, it will be especially important to rely on *in operando* characterization techniques, rather than exclusively *ex situ* characterization techniques, to understand and address challenges associated with integrating group IV nanomaterials into electrodes for improved energy density of lithium ion batteries. In particular, surface-sensitive *in operando* spectroscopies will be particularly beneficial for monitoring electrochemical reactions at the interface of the electrode and the electrolyte, which would help elucidate the role of surface chemistry on device performance. In addition, as semiconductor nanomaterial-based electrodes are integrated into full cell devices, rather than simply half cells, it will be important to consider how certain surface chemistries and electrolyte additives function within a full cell configuration.

While both silicon and germanium are materials of interest for lithium ion batteries, silicon is likely to be of greater interest for electric vehicles due to its low cost and weight in comparison to germanium. For this reason, alloyed $Si_{1-x}Ge_x$ nanomaterials are a particularly attractive material. By introducing a small amount of germanium into silicon, the higher lithium diffusivity and electron conductivity of germanium may improve the rate capability, which could decrease charging time. Importantly, a tunable $Si_{1-x}Ge_x$ nanowire synthesis could serve as a platform to study how the lithium ion diffusion coefficient changes as a function of the silicon:germanium compositional ratio through galvanostatic intermittent titration technique (GITT). In addition, while previous *in operando* studies of germanium-based electrodes have demonstrated rate-dependent lithiation mechanisms, *in operando* XRD of $Si_{1-x}Ge_x$ alloys has yet to be explored

extensively and could provide information about the phase changes during electrochemical lithiation, especially for different rates.

Also, the surface chemistry of $Si_{1-x}Ge_x$ nanowires synthesized through supercritical fluid-based methods remains unexplored; given the observed importance of interfacial surface chemistry, studies of the $Si_{1-x}Ge_x$ nanowire surface will be vital to effectively integrate $Si_{1-x}Ge_x$ nanowires into electrodes for lithium ion batteries. Preliminary results suggest the presence of an amorphous poly(phenylsilane) coating on $Si_{1-x}Ge_x$ nanowires, which could be leveraged to improve device performance by annealing under a reducing environment to create a conductive carbon coating.

More broadly, while the formation of a stable solid-electrolyte interphase layer will be crucial for the advancement of silicon- and germanium- based electrodes for battery applications, there exist additional challenges to improve the overall capacity and rate capability of colloidally-synthesized nanomaterial-based electrodes. In particular, identifying methods to improve direct contact of solution-grown nanomaterials, including semiconductor nanowires, with the current collector will be important to improve charge transport and rate capability. As silicon and germanium nanomaterial-based electrodes are cycled, the repeated volume expansion and contraction associated with lithiation and delithiation can result in delamination from the current collector, compromising the conductive pathways of the nanomaterial to the current collector. Nanowire-based electrodes fabricated through slurry-casting likely have fewer initial points of contact with the current collector compared to vapor-grown semiconductor nanowire electrodes, which are grown directly from the current collector. In order to improve stability and charge transport, it will be important to develop strategies to maintain and improve contact between colloidally-synthesized semiconductor nanowires and the current collector.

BIBLIOGRAPHY

1. Xiao, X. *et al.* Quantum confinement effects in strained silicon-germanium alloy quantum wells. *Appl. Phys. Lett.* **60**, 2135–2137 (1992).
2. Duan, X., Huang, Y., Cui, Y., Wang, J. & Lieber, C. M. Indium phosphide nanowires as building blocks for nanoscale electronic and optoelectronic devices. *Nature* **409**, 66–69 (2001).
3. Huang, Y. *et al.* Logic Gates and Computation from Assembled Nanowire Building Blocks. *Science* **294**, 1313–1317 (2001).
4. Duan, X., Wang, J. & Lieber, C. M. Synthesis and optical properties of gallium arsenide nanowires. *Appl. Phys. Lett.* **76**, 1116–1118 (2000).
5. Asgar, M. A., Hasan, M., Huq, M. F. & Mahmood, Z. H. Broadband optical absorption measurement of silicon nanowires for photovoltaic solar cell applications. *Int Nano Lett* **4**, 1–5 (2014).
6. Paniagua-Domínguez, R., Grzela, G., Gómez Rivas, J. & A. Sánchez-Gil, J. Enhanced and directional emission of semiconductor nanowires tailored through leaky/guided modes. *Nanoscale* **5**, 10582–10590 (2013).
7. Zhu, Y., Xu, F., Qin, Q., Fung, W. Y. & Lu, W. Mechanical Properties of Vapor−Liquid−Solid Synthesized Silicon Nanowires. *Nano Lett.* **9**, 3934–3939 (2009).
8. Smith, D. A., Holmberg, V. C. & Korgel, B. A. Flexible Germanium Nanowires: Ideal Strength, Room Temperature Plasticity, and Bendable Semiconductor Fabric. *ACS Nano* **4**, 2356–2362 (2010).

9. Chen, J. *et al.* Probing Strain in Bent Semiconductor Nanowires with Raman Spectroscopy. *Nano Lett.* **10**, 1280–1286 (2010).

10. Delley, B. & Steigmeier, E. F. Size dependence of band gaps in silicon nanostructures. *Applied Physics Letters* **67**, 2370–2372 (1995).

11. Ma, D. D. D., Lee, C. S., Au, F. C. K., Tong, S. Y. & Lee, S. T. Small-Diameter Silicon Nanowire Surfaces. *Science* **299**, 1874–1877 (2003).

12. Cui, Y., Wei, Q., Park, H. & Lieber, C. M. Nanowire Nanosensors for Highly Sensitive and Selective Detection of Biological and Chemical Species. *Science* **293**, 1289–1292 (2001).

13. Chua, J. H., Chee, R.-E., Agarwal, A., Wong, S. M. & Zhang, G.-J. Label-Free Electrical Detection of Cardiac Biomarker with Complementary Metal-Oxide Semiconductor-Compatible Silicon Nanowire Sensor Arrays. *Anal. Chem.* **81**, 6266–6271 (2009).

14. McAlpine, M. C., Ahmad, H., Wang, D. & Heath, J. R. Highly ordered nanowire arrays on plastic substrates for ultrasensitive flexible chemical sensors. *Nature Materials* **6**, 379–384 (2007).

15. Garnett, E. C. & Yang, P. Silicon Nanowire Radial p−n Junction Solar Cells. *J. Am. Chem. Soc.* **130**, 9224–9225 (2008).

16. Kelzenberg, M. D. *et al.* Photovoltaic Measurements in Single-Nanowire Silicon Solar Cells. *Nano Lett.* **8**, 710–714 (2008).

17. Tang, J., Huo, Z., Brittman, S., Gao, H. & Yang, P. Solution-processed core-shell nanowires for efficient photovoltaic cells. *Nat Nano* **6**, 568–572 (2011).

18. Martinez, J. A., Provencio, P. P., Picraux, S. T., Sullivan, J. P. & Swartzentruber, B. S. Enhanced thermoelectric figure of merit in SiGe alloy nanowires by boundary and hole-phonon scattering. *Journal of Applied Physics* **110**, 074317 (2011).

19. Lee, E. K. *et al.* Large Thermoelectric Figure-of-Merits from SiGe Nanowires by Simultaneously Measuring Electrical and Thermal Transport Properties. *Nano Lett.* **12**, 2918–2923 (2012).

20. Chan, C. K. *et al.* High-performance lithium battery anodes using silicon nanowires. *Nat Nano* **3**, 31–35 (2008).

21. Chockla, A. M. *et al.* Silicon Nanowire Fabric as a Lithium Ion Battery Electrode Material. *J. Am. Chem. Soc.* **133**, 20914–20921 (2011).

22. Chockla, A. M., Klavetter, K. C., Mullins, C. B. & Korgel, B. A. Solution-Grown Germanium Nanowire Anodes for Lithium-Ion Batteries. *ACS Appl. Mater. Interfaces* **4**, 4658–4664 (2012).

23. Yuan, F.-W., Yang, H.-J. & Tuan, H.-Y. Alkanethiol-Passivated Ge Nanowires as High-Performance Anode Materials for Lithium-Ion Batteries: The Role of Chemical Surface Functionalization. *ACS Nano* **6**, 9932–9942 (2012).

24. Chockla, A. M. *et al.* Influences of Gold, Binder and Electrolyte on Silicon Nanowire Performance in Li-Ion Batteries. *J. Phys. Chem. C* **116**, 18079–18086 (2012).

25. Chockla, A. M., Klavetter, K. C., Mullins, C. B. & Korgel, B. A. Tin-Seeded Silicon Nanowires for High Capacity Li-Ion Batteries. *Chem. Mater.* **24**, 3738–3745 (2012).

26. Hobbs, R. G., Petkov, N. & Holmes, J. D. Semiconductor Nanowire Fabrication by Bottom-Up and Top-Down Paradigms. *Chem. Mater.* **24**, 1975–1991 (2012).

27. Moreau, W. M. *Semiconductor Lithography: Principles, Practices, and Materials*. (Springer Science & Business Media, 2012).

28. Pennelli, G. Top-down fabrication of silicon nanowire devices for thermoelectric applications: properties and perspectives. *Eur. Phys. J. B* **88**, 121 (2015).

29. Wagner, R. S., Ellis, W. C., Jackson, K. A. & Arnold, S. M. Study of the Filamentary Growth of Silicon Crystals from the Vapor. *Journal of Applied Physics* **35**, 2993–3000 (1964).

30. Dujardin, R. *et al.* Growth mechanism of Si nanowhiskers and SiGe heterostructures in Si nanowhiskers: X-ray scattering and electron microscopy investigations. *Appl. Phys. Lett.* **89**, 153129 (2006).

31. Morales, A. M. & Lieber, C. M. A Laser Ablation Method for the Synthesis of Crystalline Semiconductor Nanowires. *Science* **279**, 208–211 (1998).

32. Kodambaka, S., Tersoff, J., Reuter, M. C. & Ross, F. M. Germanium Nanowire Growth Below the Eutectic Temperature. *Science* **316**, 729–732 (2007).

33. Trentler, T. J. *et al.* Solution-Liquid-Solid Growth of Crystalline III-V Semiconductors: An Analogy to Vapor-Liquid-Solid Growth. *Science* **270**, 1791–1794 (1995).

34. Hanrath, T. & Korgel, B. a. Supercritical Fluid–Liquid–Solid (SFLS) Synthesis of Si and Ge Nanowires Seeded by Colloidal Metal Nanocrystals. *Adv. Mater.* **15**, 437–440 (2003).

35. Tuan, H.-Y., Lee, D. C., Hanrath, T. & Korgel, B. A. Catalytic Solid-Phase Seeding of Silicon Nanowires by Nickel Nanocrystals in Organic Solvents. *Nano Lett.* **5**, 681–684 (2005).

36. Seifner, M. S. *et al.* Lead-supported germanium nanowire growth. *Materials Letters* **173**, 248–251 (2016).

37. Geaney, H. *et al.* High Density Growth of Indium seeded Silicon Nanowires in the Vapor phase of a High Boiling Point Solvent. *Chem. Mater.* **24**, 2204–2210 (2012).

38. Dasgupta, N. P. *et al.* 25th Anniversary Article: Semiconductor Nanowires – Synthesis, Characterization, and Applications. *Advanced Materials* **26**, 2137–2184 (2014).

39. Hanrath, T. & Korgel, B. A. Nucleation and Growth of Germanium Nanowires Seeded by Organic Monolayer-Coated Gold Nanocrystals. *J. Am. Chem. Soc.* **124**, 1424–1429 (2002).

40. Wagner, R. S. & Ellis, W. C. Vapor-liquid-solid mechanism of single crystal growth. *Appl. Phys. Lett.* **4**, 89–90 (1964).

41. Yazawa, M., Koguchi, M. & Hiruma, K. Heteroepitaxial ultrafine wire-like growth of InAs on GaAs substrates. *Appl. Phys. Lett.* **58**, 1080–1082 (1991).

42. Au (Gold) Binary Alloy Phase Diagrams. in *Alloy Phase Diagrams* (eds. Okamoto, H., Schlesinger, M. E. & Mueller, E. M.) 152–174 (ASM International, 2016). doi:10.31399/asm.hb.v03.a0006146.

43. Yang, P., Yan, R. & Fardy, M. Semiconductor Nanowire: What's Next? *Nano Lett.* **10**, 1529–1536 (2010).

44. Schmidt, V., Wittemann, J. V., Senz, S. & Gösele, U. Silicon Nanowires: A Review on Aspects of their Growth and their Electrical Properties. *Advanced Materials* **21**, 2681–2702 (2009).

45. Sutter, E. A. & Sutter, P. W. Size-Dependent Phase Diagram of Nanoscale Alloy Drops Used in Vapor−Liquid−Solid Growth of Semiconductor Nanowires. *ACS Nano* **4**, 4943–4947 (2010).

46. Sutter, E. & Sutter, P. Phase Diagram of Nanoscale Alloy Particles Used for Vapor−Liquid−Solid Growth of Semiconductor Nanowires. *Nano Lett.* **8**, 411–414 (2008).

47. Park, H. D., Gaillot, A.-C., Prokes, S. M. & Cammarata, R. C. Observation of size dependent liquidus depression in the growth of InAs nanowires. *Journal of Crystal Growth* **296**, 159–164 (2006).

48. Chen, L., Lu, W. & Lieber, C. M. Chapter 1 Semiconductor Nanowire Growth and Integration. in 1–53 (RSC Publishing, 2014).

49. Patolsky, F. & Lieber, C. M. Nanowire nanosensors. *Materials Today* **8**, 20–28 (2005).

50. Gudiksen, M. S., Lauhon, L. J., Wang, J., Smith, D. C. & Lieber, C. M. Growth of nanowire superlattice structures for nanoscale photonics and electronics. *Nature* **415**, 617–620 (2002).

51. Wu, Y., Fan, R. & Yang, P. Block-by-Block Growth of Single-Crystalline Si/SiGe Superlattice Nanowires. *Nano Lett.* **2**, 83–86 (2002).

52. Lauhon, L. J., Gudiksen, M. S., Wang, D. & Lieber, C. M. Epitaxial core–shell and core–multishell nanowire heterostructures. *Nature* **420**, 57–61 (2002).

53. Qian, F., Gradečak, S., Li, Y., Wen, C.-Y. & Lieber, C. M. Core/Multishell Nanowire Heterostructures as Multicolor, High-Efficiency Light-Emitting Diodes. *Nano Lett.* **5**, 2287–2291 (2005).

54. Clark, T. E. *et al.* Diameter Dependent Growth Rate and Interfacial Abruptness in Vapor–Liquid–Solid Si/Si1−xGex Heterostructure Nanowires. *Nano Lett.* **8**, 1246–1252 (2008).

55. Hochbaum, A. I., Fan, R., He, R. & Yang, P. Controlled Growth of Si Nanowire Arrays for Device Integration. *Nano Lett.* **5**, 457–460 (2005).

56. Boettcher, S. W. *et al.* Energy-Conversion Properties of Vapor-Liquid-Solid–Grown Silicon Wire-Array Photocathodes. *Science* **327**, 185–187 (2010).

57. Garnett, E. & Yang, P. Light Trapping in Silicon Nanowire Solar Cells. *Nano Lett.* **10**, 1082–1087 (2010).

58. Chockla, A. M., Harris, J. T. & Korgel, B. A. Colloidal Synthesis of Germanium Nanorods. *Chem. Mater.* **23**, 1964–1970 (2011).

59. Heitsch, A. T., Fanfair, D. D., Tuan, H.-Y. & Korgel, B. A. Solution−Liquid−Solid (SLS) Growth of Silicon Nanowires. *J. Am. Chem. Soc.* **130**, 5436–5437 (2008).

60. Dong, A., Wang, F., Daulton, T. L. & Buhro, W. E. Solution−Liquid−Solid (SLS) Growth of ZnSe−ZnTe Quantum Wires having Axial Heterojunctions. *Nano Lett.* **7**, 1308–1313 (2007).

61. Wang Fudong & Buhro William E. An Easy Shortcut Synthesis of Size-Controlled Bismuth Nanoparticles and Their Use in the SLS Growth of High-Quality Colloidal Cadmium Selenide Quantum Wires. *Small* **6**, 573–581 (2010).

62. Li, Z. *et al.* Diluted Magnetic Semiconductor Nanowires Prepared by the Solution–Liquid–Solid Method. *Angewandte Chemie* **122**, 2837–2841 (2010).

63. Bodnarchuk, M. I., Kravchyk, K. V., Krumeich, F., Wang, S. & Kovalenko, M. V. Colloidal Tin–Germanium Nanorods and Their Li-Ion Storage Properties. *ACS Nano* **8**, 2360–2368 (2014).

64. Shah, P. S., Hanrath, T., Johnston, K. P. & Korgel, B. A. Nanocrystal and Nanowire Synthesis and Dispersibility in Supercritical Fluids. *J. Phys. Chem. B* **108**, 9574–9587 (2004).

65. Davidson, F. M., Wiacek, R. & Korgel, B. A. Supercritical Fluid−Liquid−Solid Synthesis of Gallium Phosphide Nanowires. *Chem. Mater.* **17**, 230–233 (2005).

66. Lu, X., Fanfair, D. D., Johnston, K. P. & Korgel, B. A. High Yield Solution−Liquid−Solid Synthesis of Germanium Nanowires. *J. Am. Chem. Soc.* **127**, 15718–15719 (2005).

67. Tuan, H.-Y. & Korgel, B. A. Importance of Solvent-Mediated Phenylsilane Decompositon Kinetics for High-Yield Solution-Phase Silicon Nanowire Synthesis. *Chem. Mater.* **20**, 1239–1241 (2008).

68. Kuno, M. An overview of solution-based semiconductor nanowires: synthesis and optical studies. *Phys. Chem. Chem. Phys.* **10**, 620–639 (2008).

69. Heitsch, A. T., Akhavan, V. A. & Korgel, B. A. Rapid SFLS Synthesis of Si Nanowires Using Trisilane with In situ Alkyl-Amine Passivation. *Chem. Mater.* **23**, 2697–2699 (2011).

70. Stokes, K. *et al.* Direct Synthesis of Alloyed Si1–xGex Nanowires for Performance-Tunable Lithium Ion Battery Anodes. *ACS Nano* **11**, 10088–10096 (2017).

71. Wang, D. *et al.* Surface Chemistry and Electrical Properties of Germanium Nanowires. *J. Am. Chem. Soc.* **126**, 11602–11611 (2004).

72. Paska, Y. & Haick, H. Interactive Effect of Hysteresis and Surface Chemistry on Gated Silicon Nanowire Gas Sensors. *ACS Appl. Mater. Interfaces* **4**, 2604–2617 (2012).

73. Holmberg, V. C., Rasch, M. R. & Korgel, B. A. PEGylation of Carboxylic Acid-Functionalized Germanium Nanowires. *Langmuir* **26**, 14241–14246 (2010).

74. Buriak, J. M. Organometallic Chemistry on Silicon and Germanium Surfaces. *Chem. Rev.* **102**, 1271–1308 (2002).

75. Loscutoff, P. W. & Bent, S. F. REACTIVITY OF THE GERMANIUM SURFACE: Chemical Passivation and Functionalization. *Annual Review of Physical Chemistry* **57**, 467–495 (2006).

76. Bent, S. F. Organic functionalization of group IV semiconductor surfaces: principles, examples, applications, and prospects. *Surface Science* **500**, 879–903 (2002).

77. Hanrath, T. & Korgel, B. A. Chemical Surface Passivation of Ge Nanowires. *J. Am. Chem. Soc.* **126**, 15466–15472 (2004).

78. Holmberg, V. C. & Korgel, B. A. Corrosion Resistance of Thiol- and Alkene-Passivated Germanium Nanowires. *Chem. Mater.* **22**, 3698–3703 (2010).

79. Cai, Y. *et al.* The Size-Dependent Growth Direction of ZnSe Nanowires. *Advanced Materials* **18**, 109–114 (2006).

80. Wang, J. *et al.* Reversible Switching of InP Nanowire Growth Direction by Catalyst Engineering. *Nano Lett.* **13**, 3802–3806 (2013).

81. Shin, N. & Filler, M. A. Controlling Silicon Nanowire Growth Direction via Surface Chemistry. *Nano Lett.* **12**, 2865–2870 (2012).

82. Dubrovskii, V. G. & Sibirev, N. V. General form of the dependences of nanowire growth rate on the nanowire radius. *Journal of Crystal Growth* **304**, 504–513 (2007).

83. Dubrovskii, V. G. *et al.* Gibbs-Thomson and diffusion-induced contributions to the growth rate of Si, InP, and GaAs nanowires. *Phys. Rev. B* **79**, 205316 (2009).

84. Crane, M. J. & Pauzauskie, P. J. Mass Transport in Nanowire Synthesis: An Overview of Scalable Nanomanufacturing. *Journal of Materials Science & Technology* **31**, 523–532 (2015).

85. Dick, K. A., Bolinsson, J., Borg, B. M. & Johansson, J. Controlling the Abruptness of Axial Heterojunctions in III–V Nanowires: Beyond the Reservoir Effect. *Nano Lett.* **12**, 3200–3206 (2012).

86. Perea, D. E., Li, N., Dickerson, R. M., Misra, A. & Picraux, S. T. Controlling Heterojunction Abruptness in VLS-Grown Semiconductor Nanowires via in situ Catalyst Alloying. *Nano Lett.* **11**, 3117–3122 (2011).

87. Koren, E. *et al.* Obtaining Uniform Dopant Distributions in VLS-Grown Si Nanowires. *Nano Lett.* **11**, 183–187 (2011).

88. Wang, F. & Buhro, W. E. Crystal-Phase Control by Solution–Solid–Solid Growth of II–VI Quantum Wires. *Nano Lett.* **16**, 889–894 (2016).

89. Jacobsson, D. *et al.* Interface dynamics and crystal phase switching in GaAs nanowires. *Nature* **531**, 317–322 (2016).

90. Dick, K. A., Thelander, C., Samuelson, L. & Caroff, P. Crystal Phase Engineering in Single InAs Nanowires. *Nano Lett.* **10**, 3494–3499 (2010).

91. Assali, S. *et al.* Direct Band Gap Wurtzite Gallium Phosphide Nanowires. *Nano Lett.* **13**, 1559–1563 (2013).

92. Wang, F. & Buhro, W. E. Role of Precursor-Conversion Chemistry in the Crystal-Phase Control of Catalytically Grown Colloidal Semiconductor Quantum Wires. *ACS Nano* **11**, 12526–12535 (2017).

93. Davidson, F. M., Lee, D. C., Fanfair, D. D. & Korgel, B. A. Lamellar Twinning in Semiconductor Nanowires. *J. Phys. Chem. C* **111**, 2929–2935 (2007).

94. Schmidt, V., Senz, S. & Gösele, U. Diameter-Dependent Growth Direction of Epitaxial Silicon Nanowires. *Nano Lett.* **5**, 931–935 (2005).

95. Biswas, S., O'Regan, C., Petkov, N., Morris, M. A. & Holmes, J. D. Manipulating the Growth Kinetics of Vapor–Liquid–Solid Propagated Ge Nanowires. *Nano Lett.* **13**, 4044–4052 (2013).

96. Algra, R. E. *et al.* Twinning superlattices in indium phosphide nanowires. *Nature* **456**, 369–372 (2008).

97. Shtrikman, H. *et al.* Method for Suppression of Stacking Faults in Wurtzite III−V Nanowires. *Nano Lett.* **9**, 1506–1510 (2009).

98. Pan, D. *et al.* Controlled Synthesis of Phase-Pure InAs Nanowires on Si(111) by Diminishing the Diameter to 10 nm. *Nano Lett.* **14**, 1214–1220 (2014).

99. Schmidt, V., Wittemann, J. V. & Gösele, U. Growth, Thermodynamics, and Electrical Properties of Silicon Nanowires. *Chem. Rev.* **110**, 361–388 (2010).

100. Caroff, P. *et al.* Controlled polytypic and twin-plane superlattices in iii–v nanowires. *Nature Nanotechnology* **4**, 50–55 (2009).

101. Panciera, F. *et al.* Controlling nanowire growth through electric field-induced deformation of the catalyst droplet. *Nature Communications* **7**, 1–8 (2016).

102. Biswas, S., Singha, A., Morris, M. A. & Holmes, J. D. Inherent Control of Growth, Morphology, and Defect Formation in Germanium Nanowires. *Nano Lett.* **12**, 5654–5663 (2012).

103. Biswas, S., O'Regan, C., Morris, M. A. & Holmes, J. D. In-situ Observations of Nanoscale Effects in Germanium Nanowire Growth with Ternary Eutectic Alloys. *Small* **11**, 103–111 (2015).

104. Tuan, H.-Y., Lee, D. C., Hanrath, T. & Korgel, B. A. Germanium Nanowire Synthesis: An Example of Solid-Phase Seeded Growth with Nickel Nanocrystals. *Chem. Mater.* **17**, 5705–5711 (2005).

105. Han, N. *et al.* Facile synthesis and growth mechanism of Ni-catalyzed GaAs nanowires on non-crystalline substrates. *Nanotechnology* **22**, 285607 (2011).

106. Barth, S., Koleśnik, M. M., Donegan, K., Krstić, V. & Holmes, J. D. Diameter-Controlled Solid-Phase Seeding of Germanium Nanowires: Structural Characterization and Electrical Transport Properties. *Chem. Mater.* **23**, 3335–3340 (2011).

107. Tuan, H.-Y., Lee, D. C. & Korgel, B. A. Nanocrystal-Mediated Crystallization of Silicon and Germanium Nanowires in Organic Solvents: The Role of Catalysis and Solid-Phase Seeding. *Angewandte Chemie International Edition* **45**, 5184–5187 (2006).

108. Lee, D. C., Hanrath, T. & Korgel, B. A. The Role of Precursor-Decomposition Kinetics in Silicon-Nanowire Synthesis in Organic Solvents. *Angewandte Chemie International Edition* **44**, 3573–3577 (2005).

109. Davidson, F. M., Schricker, A. D., Wiacek, R. J. & Korgel, B. A. Supercritical Fluid–Liquid–Solid Synthesis of Gallium Arsenide Nanowires Seeded by Alkanethiol-Stabilized Gold Nanocrystals. *Advanced Materials* **16**, 646–649 (2004).

110. Tian, B. *et al.* Macroporous nanowire nanoelectronic scaffolds for synthetic tissues. *Nature Mater* **11**, 986–994 (2012).

111. Dai, X., Zhou, W., Gao, T., Liu, J. & Lieber, C. M. Three-dimensional mapping and regulation of action potential propagation in nanoelectronics-innervated tissues. *Nature Nanotech* **11**, 776–782 (2016).

112. Zhou, W., Dai, X. & Lieber, C. M. Advances in nanowire bioelectronics. *Rep. Prog. Phys.* **80**, 016701 (2016).

113. Dai, X., Hong, G., Gao, T. & Lieber, C. M. Mesh Nanoelectronics: Seamless Integration of Electronics with Tissues. *Acc. Chem. Res.* **51**, 309–318 (2018).

114. Thong, L. V., Loan, L. T. N. & Van Hieu, N. Comparative study of gas sensor performance of SnO2 nanowires and their hierarchical nanostructures. *Sensors and Actuators B: Chemical* **150**, 112–119 (2010).

115. Samà, J. *et al.* Low temperature humidity sensor based on Ge nanowires selectively grown on suspended microhotplates. *Sensors and Actuators B: Chemical* **243**, 669–677 (2017).

116. Gao, N. *et al.* Specific detection of biomolecules in physiological solutions using graphene transistor biosensors. *PNAS* **113**, 14633–14638 (2016).

117. Kim, S.-K. *et al.* Nanowire Photonics and Their Applications. *Computational Nanophotonics* https://www.taylorfrancis.com/ (2018) doi:10.1201/b15272-8.

118. Pauzauskie, P. J. & Yang, P. Nanowire photonics. *Materials Today* **9**, 36–45 (2006).

119. Fan, P. *et al.* An invisible metal–semiconductor photodetector. *Nature Photonics* **6**, 380–385 (2012).

120. Yan, R., Gargas, D. & Yang, P. Nanowire photonics. *Nature Photon* **3**, 569–576 (2009).

121. Eaton, S. W., Fu, A., Wong, A. B., Ning, C.-Z. & Yang, P. Semiconductor nanowire lasers. *Nature Reviews Materials* **1**, 1–11 (2016).

122. Zhu, H. *et al.* Lead halide perovskite nanowire lasers with low lasing thresholds and high quality factors. *Nature Materials* **14**, 636–642 (2015).

123. Yang, G., Zhong, H., Bai, Z., Liu, R. & Zou, B. Ultralong Homogeneously Alloyed CdSexS1-x Nanowires with Highly Polarized and Color-Tunable Emissions. *Advanced Optical Materials* **2**, 885–891 (2014).

124. Lee, B.-H. *et al.* Vertically Integrated Multiple Nanowire Field Effect Transistor. *Nano Lett.* **15**, 8056–8061 (2015).

125. Cui, Y., Zhong, Z., Wang, D., Wang, W. U. & Lieber, C. M. High Performance Silicon Nanowire Field Effect Transistors. *Nano Lett.* **3**, 149–152 (2003).

126. Fan, Z. *et al.* Toward the Development of Printable Nanowire Electronics and Sensors. *Advanced Materials* **21**, 3730–3743 (2009).

127. Greytak, A. B., Lauhon, L. J., Gudiksen, M. S. & Lieber, C. M. Growth and transport properties of complementary germanium nanowire field-effect transistors. *Appl. Phys. Lett.* **84**, 4176–4178 (2004).

128. Yan, H. *et al.* Programmable nanowire circuits for nanoprocessors. *Nature* **470**, 240–244 (2011).

129. Heinzig, A., Slesazeck, S., Kreupl, F., Mikolajick, T. & Weber, W. M. Reconfigurable Silicon Nanowire Transistors. *Nano Lett.* **12**, 119–124 (2012).

130. Mourik, V. *et al.* Signatures of Majorana Fermions in Hybrid Superconductor-Semiconductor Nanowire Devices. *Science* **336**, 1003–1007 (2012).

131. Gazibegovic, S. *et al.* Epitaxy of advanced nanowire quantum devices. *Nature* **548**, 434–438 (2017).

132. Baugh, J., Fung, J. S., Mracek, J. & LaPierre, R. R. Building a spin quantum bit register using semiconductor nanowires. *Nanotechnology* **21**, 134018 (2010).

133. Sau, J. D., Tewari, S. & Das Sarma, S. Experimental and materials considerations for the topological superconducting state in electron- and hole-doped semiconductors: Searching for non-Abelian Majorana modes in 1D nanowires and 2D heterostructures. *Phys. Rev. B* **85**, 064512 (2012).

134. Albrecht, S. M. *et al.* Exponential protection of zero modes in Majorana islands. *Nature* **531**, 206–209 (2016).

135. Deng, M. T. *et al.* Majorana bound state in a coupled quantum-dot hybrid-nanowire system. *Science* **354**, 1557–1562 (2016).

136. Zhang, H., Liu, D. E., Wimmer, M. & Kouwenhoven, L. P. Next steps of quantum transport in Majorana nanowire devices. *Nature Communications* **10**, 1–7 (2019).

137. Dasgupta, N. P. & Yang, P. Semiconductor nanowires for photovoltaic and photoelectrochemical energy conversion. *Front. Phys.* **9**, 289–302 (2013).

138. Lee, S.-Y. *et al.* Progress in flexible energy storage and conversion systems, with a focus on cable-type lithium-ion batteries. *Energy Environ. Sci.* **6**, 2414–2423 (2013).

139. Gadea, G., Pacios, M., Morata, Á. & Tarancón, A. Silicon-based nanostructures for integrated thermoelectric generators. *J. Phys. D: Appl. Phys.* **51**, 423001 (2018).

140. Son, J. S. *et al.* Large-Scale Synthesis and Characterization of the Size-Dependent Thermoelectric Properties of Uniformly Sized Bismuth Nanocrystals. *Angewandte Chemie International Edition* **50**, 1363–1366.

141. Liu, B., Wu, C.-H., Miao, J. & Yang, P. All Inorganic Semiconductor Nanowire Mesh for Direct Solar Water Splitting. *ACS Nano* **8**, 11739–11744 (2014).

142. Su, Y. *et al.* Single-nanowire photoelectrochemistry. *Nature Nanotechnology* **11**, 609–612 (2016).

143. Tian, B., J. Kempa, T. & M. Lieber, C. Single nanowire photovoltaics. *Chemical Society Reviews* **38**, 16–24 (2009).

144. Haverkort, J. E. M., Garnett, E. C. & Bakkers, E. P. A. M. Fundamentals of the nanowire solar cell: Optimization of the open circuit voltage. *Applied Physics Reviews* **5**, 031106 (2018).

145. Steinhagen, C. *et al.* Solution−Liquid−Solid Synthesis of CuInSe2 Nanowires and Their Implementation in Photovoltaic Devices. *ACS Appl. Mater. Interfaces* **3**, 1781–1785 (2011).

146. Kennedy, T. *et al.* High-Performance Germanium Nanowire-Based Lithium-Ion Battery Anodes Extending over 1000 Cycles Through in Situ Formation of a Continuous Porous Network. *Nano Lett.* **14**, 716–723 (2014).

147. Karki, K. *et al.* Lithium-Assisted Electrochemical Welding in Silicon Nanowire Battery Electrodes. *Nano Lett.* **12**, 1392–1397 (2012).

148. Buriak, J. M. Illuminating Silicon Surface Hydrosilylation: An Unexpected Plurality of Mechanisms. *Chem. Mater.* **26**, 763–772 (2014).

149. Ardalan, P., Musgrave, C. B. & Bent, S. F. Formation of Alkanethiolate Self-Assembled Monolayers at Halide-Terminated Ge Surfaces. *Langmuir* **25**, 2013–2025 (2009).

150. Wu, Y. & Yang, P. Direct Observation of Vapor−Liquid−Solid Nanowire Growth. *J. Am. Chem. Soc.* **123**, 3165–3166 (2001).

151. Kallesøe, C., Wen, C.-Y., Mølhave, K., Bøggild, P. & Ross, F. M. Measurement of Local Si-Nanowire Growth Kinetics Using In situ Transmission Electron Microscopy of Heated Cantilevers. *Small* **6**, 2058–2064 (2010).

152. Sivaram, S. V., Shin, N., Chou, L.-W. & Filler, M. A. Direct Observation of Transient Surface Species during Ge Nanowire Growth and Their Influence on Growth Stability. *J. Am. Chem. Soc.* **137**, 9861–9869 (2015).

153. Di Martino, G., Michaelis, F. B., Salmon, A. R., Hofmann, S. & Baumberg, J. J. Controlling Nanowire Growth by Light. *Nano Lett.* **15**, 7452–7457 (2015).

154. Kim, B. J. *et al.* Kinetics of Individual Nucleation Events Observed in Nanoscale Vapor-Liquid-Solid Growth. *Science* **322**, 1070–1073 (2008).

155. Kodambaka, S., Tersoff, J., Reuter, M. C. & Ross, F. M. Diameter-Independent Kinetics in the Vapor-Liquid-Solid Growth of Si Nanowires. *Phys. Rev. Lett.* **96**, 096105 (2006).

156. Madras, P., Dailey, E. & Drucker, J. Kinetically Induced Kinking of Vapor−Liquid−Solid Grown Epitaxial Si Nanowires. *Nano Lett.* **9**, 3826–3830 (2009).

157. Hillerich, K. *et al.* Strategies To Control Morphology in Hybrid Group III–V/Group IV Heterostructure Nanowires. *Nano Lett.* **13**, 903–908 (2013).

158. Kodambaka, S., Hannon, J. B., Tromp, R. M. & Ross, F. M. Control of Si Nanowire Growth by Oxygen. *Nano Lett.* **6**, 1292–1296 (2006).

159. Gamalski, A. D. *et al.* The Role of Surface Passivation in Controlling Ge Nanowire Faceting. *Nano Lett.* **15**, 8211–8216 (2015).

160. Dubrovskii, V. G. Development of Growth Theory for Vapor–Liquid–Solid Nanowires: Contact Angle, Truncated Facets, and Crystal Phase. *Crystal Growth & Design* **17**, 2544–2548 (2017).

161. Sun, Z., Seidman, D. N. & Lauhon, L. J. Nanowire Kinking Modulates Doping Profiles by Reshaping the Liquid–Solid Growth Interface. *Nano Lett.* **17**, 4518–4525 (2017).

162. Connell, J. G. *et al.* Identification of an Intrinsic Source of Doping Inhomogeneity in Vapor–Liquid–Solid-Grown Nanowires. *Nano Lett.* **13**, 199–206 (2013).

163. Jeon, N., Dayeh, S. A. & Lauhon, L. J. Origin of Polytype Formation in VLS-Grown Ge Nanowires through Defect Generation and Nanowire Kinking. *Nano Lett.* **13**, 3947–3952 (2013).

164. Dorn, A., Allen, P. M. & Bawendi, M. G. Electrically Controlling and Monitoring InP Nanowire Growth from Solution. *ACS Nano* **3**, 3260–3265 (2009).

165. Li, Z., Sun, Q., Dong Yao, X., Hua Zhu, Z. & Qing (Max) Lu, G. Semiconductor nanowires for thermoelectrics. *Journal of Materials Chemistry* **22**, 22821–22831 (2012).

166. Mao, L., Gong, M., Dumitrescu, E., Tewari, S. & Zhang, C. Hole-Doped Semiconductor Nanowire on Top of an s-Wave Superconductor: A New and Experimentally Accessible System for Majorana Fermions. *Phys. Rev. Lett.* **108**, 177001 (2012).

167. Bulgarini, G. *et al.* Avalanche amplification of a single exciton in a semiconductor nanowire. *Nature Photon* **6**, 455–458 (2012).

168. Li, Y., Qian, F., Xiang, J. & Lieber, C. M. Nanowire electronic and optoelectronic devices. *Materials Today* **9**, 18–27 (2006).

169. Alanis, J. A. *et al.* Optical Study of p-Doping in GaAs Nanowires for Low-Threshold and High-Yield Lasing. *Nano Lett.* **19**, 362–368 (2019).

170. Arab, S., Yao, M., Zhou, C., Daniel Dapkus, P. & Cronin, S. B. Doping concentration dependence of the photoluminescence spectra of n-type GaAs nanowires. *Appl. Phys. Lett.* **108**, 182106 (2016).

171. Röder, R. & Ronning, C. Review on the dynamics of semiconductor nanowire lasers. *Semicond. Sci. Technol.* **33**, 033001 (2018).

172. Nah, J., Varahramyan, K., Liu, E.-S., Banerjee, S. K. & Tutuc, E. Doping of Ge–SixGe1−x core-shell nanowires using low energy ion implantation. *Appl. Phys. Lett.* **93**, 203108 (2008).

173. Ronning, C., Borschel, C., Geburt, S. & Niepelt, R. Ion beam doping of semiconductor nanowires. *Materials Science and Engineering: R: Reports* **70**, 30–43 (2010).

174. Ho, J. C. *et al.* Controlled nanoscale doping of semiconductors via molecular monolayers. *Nature Mater* **7**, 62–67 (2008).

175. Radovanovic, P. V., Barrelet, C. J., Gradečak, S., Qian, F. & Lieber, C. M. General Synthesis of Manganese-Doped II−VI and III−V Semiconductor Nanowires. *Nano Lett.* **5**, 1407–1411 (2005).

176. Martelli, F. *et al.* Manganese-Induced Growth of GaAs Nanowires. *Nano Lett.* **6**, 2130–2134 (2006).

177. Ke, Y. *et al.* Fabrication and Electrical Properties of Si Nanowires Synthesized by Al Catalyzed Vapor−Liquid−Solid Growth. *Nano Lett.* **9**, 4494–4499 (2009).

178. Seifner, M. S. *et al.* Direct Synthesis of Hyperdoped Germanium Nanowires. *ACS Nano* **12**, 1236–1241 (2018).

179. R. Zamani, R., Ghalamestani, S. G., Niu, J., Sköld, N. & A. Dick, K. Polarity and growth directions in Sn-seeded GaSb nanowires. *Nanoscale* **9**, 3159–3168 (2017).

180. Moutanabbir, O. *et al.* Colossal injection of catalyst atoms into silicon nanowires. *Nature* **496**, 78–82 (2013).

181. Sutter, E. & Sutter, P. Vapor–liquid–solid growth and Sb doping of Ge nanowires from a liquid Au-Sb-Ge ternary alloy. *Appl. Phys. A* **99**, 217–221 (2010).

182. Amit, I. *et al.* Spatially Resolved Correlation of Active and Total Doping Concentrations in VLS Grown Nanowires. *Nano Lett.* **13**, 2598–2604 (2013).

183. Wallentin, J. & Borgström, M. T. Doping of semiconductor nanowires. *Journal of Materials Research* **26**, 2142–2156 (2011).

184. Perea, D. E. *et al.* Direct measurement of dopant distribution in an individual vapour–liquid–solid nanowire. *Nature Nanotechnology* **4**, 315–319 (2009).

185. Chen, W. *et al.* Boron distribution in the core of Si nanowire grown by chemical vapor deposition. *Journal of Applied Physics* **111**, 094909 (2012).

186. Le, S. T., Jannaty, P., Zaslavsky, A., Dayeh, S. A. & Picraux, S. T. Growth, electrical rectification, and gate control in axial in situ doped p-n junction germanium nanowires. *Appl. Phys. Lett.* **96**, 262102 (2010).

187. Whang, S.-J. *et al.* B-doping of vapour–liquid–solid grown Au-catalysed and Al-catalysed Si nanowires: effects of B2H6gas during Si nanowire growth and B-doping by a post-synthesisin situplasma process. *Nanotechnology* **18**, 275302 (2007).

188. Gu, L. *et al.* In situ doping control and electrical transport investigation of single and arrayed CdS nanopillars. *Nanoscale* **5**, 7213–7218 (2013).

189. Borgström, M. T. *et al.* Precursor evaluation forin situInP nanowire doping. *Nanotechnology* **19**, 445602 (2008).

190. Gutsche, C. *et al.* Controllable p-type doping of GaAs nanowires during vapor-liquid-solid growth. *Journal of Applied Physics* **105**, 024305 (2009).

191. Goktas, N. I., Fiordaliso, E. M. & LaPierre, R. R. Doping assessment in GaAs nanowires. *Nanotechnology* **29**, 234001 (2018).

192. Yang, G. *et al.* General Synthesis and White Light Emission of Diluted Magnetic Semiconductor Nanowires Using Single-Source Precursors. *Chem. Mater.* **25**, 3260–3266 (2013).

193. Kovalenko, M. V. *et al.* Prospects of Nanoscience with Nanocrystals. *ACS Nano* **9**, 1012–1057 (2015).

194. Grzelczak, M., Pérez-Juste, J., Mulvaney, P. & M. Liz-Marzán, L. Shape control in gold nanoparticle synthesis. *Chemical Society Reviews* **37**, 1783–1791 (2008).

195. Manna, L., Scher, E. C. & Alivisatos, A. P. Synthesis of Soluble and Processable Rod-, Arrow-, Teardrop-, and Tetrapod-Shaped CdSe Nanocrystals. *J. Am. Chem. Soc.* **122**, 12700–12706 (2000).

196. Grebinski, J. W., Hull, K. L., Zhang, J., Kosel, T. H. & Kuno, M. Solution-Based Straight and Branched CdSe Nanowires. *Chem. Mater.* **16**, 5260–5272 (2004).

197. Talapin, D. V. *et al.* Seeded Growth of Highly Luminescent CdSe/CdS Nanoheterostructures with Rod and Tetrapod Morphologies. *Nano Lett.* **7**, 2951–2959 (2007).

198. Stein, J. L., Mader, E. A. & Cossairt, B. M. Luminescent InP Quantum Dots with Tunable Emission by Post-Synthetic Modification with Lewis Acids. *J. Phys. Chem. Lett.* **7**, 1315–1320 (2016).

199. Yu, Y. *et al.* Room Temperature Hydrosilylation of Silicon Nanocrystals with Bifunctional Terminal Alkenes. *Langmuir* **29**, 1533–1540 (2013).

200. Boles, M. A., Ling, D., Hyeon, T. & Talapin, D. V. The surface science of nanocrystals. *Nature Materials* **15**, 141–153 (2016).

201. Jia, C., Lin, Z., Huang, Y. & Duan, X. Nanowire Electronics: From Nanoscale to Macroscale. *Chem. Rev.* **119**, 9074–9135 (2019).

202. Tomioka, K., Motohisa, J., Hara, S., Hiruma, K. & Fukui, T. GaAs/AlGaAs Core Multishell Nanowire-Based Light-Emitting Diodes on Si. *Nano Lett.* **10**, 1639–1644 (2010).

203. Lai, E., Kim, W. & Yang, P. Vertical nanowire array-based light emitting diodes. *Nano Res.* **1**, 123–128 (2008).

204. Åberg, I. *et al.* A GaAs Nanowire Array Solar Cell With 15.3% Efficiency at 1 Sun. *IEEE Journal of Photovoltaics* **6**, 185–190 (2016).

205. Anttu, N. & Xu, H. Q. Efficient light management in vertical nanowire arrays for photovoltaics. *Opt. Express, OE* **21**, A558–A575 (2013).

206. Frolov, S. M., Plissard, S. R., Nadj-Perge, S., Kouwenhoven, L. P. & Bakkers, E. P. A. M. Quantum computing based on semiconductor nanowires. *MRS Bulletin* **38**, 809–815 (2013).

207. Plissard, S. R. *et al.* Formation and electronic properties of InSb nanocrosses. *Nature Nanotechnology* **8**, 859–864 (2013).

208. Car, D. *et al.* InSb Nanowires with Built-In GaxIn1–xSb Tunnel Barriers for Majorana Devices. *Nano Lett.* **17**, 721–727 (2017).

209. Mullane, E., Kennedy, T., Geaney, H., Dickinson, C. & Ryan, K. M. Synthesis of Tin Catalyzed Silicon and Germanium Nanowires in a Solvent–Vapor System and Optimization of the Seed/Nanowire Interface for Dual Lithium Cycling. *Chem. Mater.* **25**, 1816–1822 (2013).

210. Holmberg, V. C., Bogart, T. D., Chockla, A. M., Hessel, C. M. & Korgel, B. A. Optical Properties of Silicon and Germanium Nanowire Fabric. *J. Phys. Chem. C* **116**, 22486–22491 (2012).

211. Petchsang, N., McDonald, M. P., Sinks, L. E. & Kuno, M. Light Induced Nanowire Assembly: The Electrostatic Alignment of Semiconductor Nanowires into Functional Macroscopic Yarns. *Adv. Mater.* **25**, 601–605 (2013).

212. Constantinou, M. *et al.* Simultaneous Tunable Selection and Self-Assembly of Si Nanowires from Heterogeneous Feedstock. *ACS Nano* (2016) doi:10.1021/acsnano.6b00005.

213. Yerushalmi, R., Jacobson, Z. A., Ho, J. C., Fan, Z. & Javey, A. Large scale, highly ordered assembly of nanowire parallel arrays by differential roll printing. *Appl. Phys. Lett.* **91**, 203104 (2007).

214. Liu, X., Long, Y.-Z., Liao, L., Duan, X. & Fan, Z. Large-Scale Integration of Semiconductor Nanowires for High-Performance Flexible Electronics. *ACS Nano* **6**, 1888–1900 (2012).

215. Javey, A., Nam, Friedman, R. S., Yan, H. & Lieber, C. M. Layer-by-Layer Assembly of Nanowires for Three-Dimensional, Multifunctional Electronics. *Nano Lett.* **7**, 773–777 (2007).

216. Huang, J., Fan, R., Connor, S. & Yang, P. One-Step Patterning of Aligned Nanowire Arrays by Programmed Dip Coating. *Angewandte Chemie International Edition* **46**, 2414–2417 (2007).

217. Acharya, S., Panda, A. B., Belman, N., Efrima, S. & Golan, Y. A Semiconductor-Nanowire Assembly of Ultrahigh Junction Density by the Langmuir–Blodgett Technique. *Advanced Materials* **18**, 210–213 (2006).

218. Kim, F., Kwan, S., Akana, J. & Yang, P. Langmuir−Blodgett Nanorod Assembly. *J. Am. Chem. Soc.* **123**, 4360–4361 (2001).

219. Yu, G., Cao, A. & Lieber, C. M. Large-area blown bubble films of aligned nanowires and carbon nanotubes. *Nature Nanotechnology* **2**, 372–377 (2007).

220. Zhao, Y. *et al.* Shape-Controlled Deterministic Assembly of Nanowires. *Nano Lett.* **16**, 2644–2650 (2016).

221. Deng, Z., Pal, S., Samanta, A., Yan, H. & Liu, Y. DNA functionalization of colloidal II–VI semiconductor nanowires for multiplex nanoheterostructures. *Chem. Sci.* **4**, 2234–2240 (2013).

222. Black, C. T. Self-aligned self assembly of multi-nanowire silicon field effect transistors. *Appl. Phys. Lett.* **87**, 163116 (2005).

223. Freer, E. M., Grachev, O., Duan, X., Martin, S. & Stumbo, D. P. High-yield self-limiting single-nanowire assembly with dielectrophoresis. *Nature Nanotechnology* **5**, 525–530 (2010).

224. Oh, K., Chung, J.-H., Riley, J. J., Liu, Y. & Liu, W. K. Fluid Flow-Assisted Dielectrophoretic Assembly of Nanowires. *Langmuir* **23**, 11932–11940 (2007).

225. Raychaudhuri, S., Dayeh, S. A., Wang, D. & Yu, E. T. Precise Semiconductor Nanowire Placement Through Dielectrophoresis. *Nano Lett.* **9**, 2260–2266 (2009).

226. Chapin, S. C., Germain, V. & Dufresne, E. R. Automated trapping, assembly, and sorting with holographic optical tweezers. *Opt. Express, OE* **14**, 13095–13100 (2006).

227. Chu, S., Cui, Y. & Liu, N. The path towards sustainable energy. *Nature Materials* **16**, 16–22 (2017).

228. Ma, Z., Pesaran, A., Gevorgian, V., Gwinner, D. & Kramer, W. Energy Storage, Renewable Power Generation, and the Grid: NREL Capabilities Help to Develop and Test Energy-Storage Technologies. *IEEE Electrification Magazine* **3**, 30–40 (2015).

229. Whittingham, M. S. History, Evolution, and Future Status of Energy Storage. *Proceedings of the IEEE* **100**, 1518–1534 (2012).

230. U.S. energy use rises to highest level ever | Lawrence Livermore National Laboratory. https://www.llnl.gov/news/us-energy-use-rises-highest-level-ever.

231. Hannula, I. & Reiner, D. M. Near-Term Potential of Biofuels, Electrofuels, and Battery Electric Vehicles in Decarbonizing Road Transport. *Joule* **3**, 2390–2402 (2019).

232. Hardman, S. *et al.* A review of consumer preferences of and interactions with electric vehicle charging infrastructure. *Transportation Research Part D: Transport and Environment* **62**, 508–523 (2018).

233. Noel, L., Zarazua de Rubens, G., Sovacool, B. K. & Kester, J. Fear and loathing of electric vehicles: The reactionary rhetoric of range anxiety. *Energy Research & Social Science* **48**, 96–107 (2019).

234. Graetz, J., Ahn, C. C., Yazami, R. & Fultz, B. Nanocrystalline and Thin Film Germanium Electrodes with High Lithium Capacity and High Rate Capabilities. *J. Electrochem. Soc.* **151**, A698–A702 (2004).

235. Graetz, J., Ahn, C. C., Yazami, R. & Fultz, B. Highly Reversible Lithium Storage in Nanostructured Silicon. *Electrochem. Solid-State Lett.* **6**, A194–A197 (2003).

236. Liu, N. *et al.* A pomegranate-inspired nanoscale design for large-volume-change lithium battery anodes. *Nature Nanotechnology* **9**, 187–192 (2014).

237. Bogart, T. D., Chockla, A. M. & Korgel, B. A. High capacity lithium ion battery anodes of silicon and germanium. *Current Opinion in Chemical Engineering* **2**, 286–293 (2013).

238. Oszajca, M. F., Bodnarchuk, M. I. & Kovalenko, M. V. Precisely Engineered Colloidal Nanoparticles and Nanocrystals for Li-Ion and Na-Ion Batteries: Model Systems or Practical Solutions? *Chem. Mater.* **26**, 5422–5432 (2014).

239. Liu, X. H. *et al.* Ultrafast Electrochemical Lithiation of Individual Si Nanowire Anodes. *Nano Lett.* **11**, 2251–2258 (2011).

240. Pharr, M., Choi, Y. S., Lee, D., Oh, K. H. & Vlassak, J. J. Measurements of stress and fracture in germanium electrodes of lithium-ion batteries during electrochemical lithiation and delithiation. *Journal of Power Sources* **304**, 164–169 (2016).

241. Yang, L. *et al.* Failure mechanisms of 2D silicon film anodes: in situ observations and simulations on crack evolution. *Chem. Commun.* **54**, 3997–4000 (2018).

242. Pharr, M., Suo, Z. & Vlassak, J. J. Measurements of the Fracture Energy of Lithiated Silicon Electrodes of Li-Ion Batteries. *Nano Lett.* **13**, 5570–5577 (2013).

243. McDowell, M. T. *et al.* Studying the Kinetics of Crystalline Silicon Nanoparticle Lithiation with In Situ Transmission Electron Microscopy. *Advanced Materials* **24**, 6034–6041 (2012).

244. Tariq, F. *et al.* In-Operando X-ray Tomography Study of Lithiation Induced Delamination of Si Based Anodes for Lithium-Ion Batteries. *ECS Electrochem. Lett.* **3**, A76–A78 (2014).

245. Shi, F. *et al.* Failure mechanisms of single-crystal silicon electrodes in lithium-ion batteries. *Nature Communications* **7**, 1–8 (2016).

246. Zhang, S., He, M., Su, C.-C. & Zhang, Z. Advanced electrolyte/additive for lithium-ion batteries with silicon anode. *Current Opinion in Chemical Engineering* **13**, 24–35 (2016).

247. Hassoun, J. & Scrosati, B. Review—Advances in Anode and Electrolyte Materials for the Progress of Lithium-Ion and beyond Lithium-Ion Batteries. *J. Electrochem. Soc.* **162**, A2582 (2015).

248. Rudawski, N. G. *et al.* Nanostructured ion beam-modified Ge films for high capacity Li ion battery anodes. *Appl. Phys. Lett.* **100**, 083111 (2012).

249. Seng, K. H., Park, M.-H., Guo, Z. P., Liu, H. K. & Cho, J. Self-Assembled Germanium/Carbon Nanostructures as High-Power Anode Material for the Lithium-Ion Battery. *Angew. Chem.* **124**, 5755–5759 (2012).

250. Li, W. *et al.* Germanium nanoparticles encapsulated in flexible carbon nanofibers as self-supported electrodes for high performance lithium-ion batteries. *Nanoscale* **6**, 4532–4537 (2014).

251. Liu, X. H. *et al.* In Situ TEM Experiments of Electrochemical Lithiation and Delithiation of Individual Nanostructures. *Advanced Energy Materials* **2**, 722–741 (2012).

252. Klavetter, K. C. *et al.* A high-rate germanium-particle slurry cast Li-ion anode with high Coulombic efficiency and long cycle life. *Journal of Power Sources* **238**, 123–136 (2013).

253. Park Mi-Hee *et al.* Germanium Nanotubes Prepared by Using the Kirkendall Effect as Anodes for High-Rate Lithium Batteries. *Angewandte Chemie International Edition* **50**, 9647–9650 (2011).

254. Williamson, G., Pandres, E. & Holmberg, V. Supercritical fluid-based synthesis and electrochemical performance of nanostructured antimony conversion electrodes with controlled anisotropy. *In Preparation* (2018).

255. Zhang, X., Kostecki, R., Richardson, T. J., Pugh, J. K. & Ross, P. N. Electrochemical and Infrared Studies of the Reduction of Organic Carbonates. *J. Electrochem. Soc.* **148**, A1341–A1345 (2001).

256. Chan, C. K., Ruffo, R., Hong, S. S. & Cui, Y. Surface chemistry and morphology of the solid electrolyte interphase on silicon nanowire lithium-ion battery anodes. *Journal of Power Sources* **189**, 1132–1140 (2009).

257. Fairbanks, B. D., Schwartz, M. P., Bowman, C. N. & Anseth, K. S. Photoinitiated polymerization of PEG-diacrylate with lithium phenyl-2,4,6-trimethylbenzoylphosphinate: polymerization rate and cytocompatibility. *Biomaterials* **30**, 6702–6707 (2009).

258. Hern, D. L. & Hubbell, J. A. Incorporation of adhesion peptides into nonadhesive hydrogels useful for tissue resurfacing. *Journal of Biomedical Materials Research* **39**, 266–276 (1998).

259. DeForest, C. A. & Anseth, K. S. Cytocompatible click-based hydrogels with dynamically tunable properties through orthogonal photoconjugation and photocleavage reactions. *Nature Chem* **3**, 925–931 (2011).

260. Arakawa, C. K., Badeau, B. A., Zheng, Y. & DeForest, C. A. Multicellular Vascularized Engineered Tissues through User-Programmable Biomaterial Photodegradation. *Advanced Materials* **29**, 1703156 (2017).

261. Kloxin, A. M., Kasko, A. M., Salinas, C. N. & Anseth, K. S. Photodegradable Hydrogels for Dynamic Tuning of Physical and Chemical Properties. *Science* **324**, 59–63 (2009).

262. Sawhney, A. S., Pathak, C. P. & Hubbell, J. A. Bioerodible hydrogels based on photopolymerized poly(ethylene glycol)-co-poly(alpha-hydroxy acid) diacrylate macromers. *Macromolecules* **26**, 581–587 (1993).

263. Badeau, B. A., Comerford, M. P., Arakawa, C. K., Shadish, J. A. & DeForest, C. A. Engineered modular biomaterial logic gates for environmentally triggered therapeutic delivery. *Nature Chemistry* **10**, 251–258 (2018).

264. Kelly, J. A. & Veinot, J. G. C. An Investigation into Near-UV Hydrosilylation of Freestanding Silicon Nanocrystals. *ACS Nano* **4**, 4645–4656 (2010).

265. Zhou, L. *et al.* Aluminum Nanocrystals as a Plasmonic Photocatalyst for Hydrogen Dissociation. *Nano Lett.* **16**, 1478–1484 (2016).

266. Mukherjee, S. *et al.* Hot-Electron-Induced Dissociation of H2 on Gold Nanoparticles Supported on SiO2. *J. Am. Chem. Soc.* **136**, 64–67 (2014).

267. Jensen, S. C., Bettis Homan, S. & Weiss, E. A. Photocatalytic Conversion of Nitrobenzene to Aniline through Sequential Proton-Coupled One-Electron Transfers from a Cadmium Sulfide Quantum Dot. *J. Am. Chem. Soc.* **138**, 1591–1600 (2016).

268. Enright, M. J., Gilbert-Bass, K., Sarsito, H. & Cossairt, B. M. Photolytic C–O Bond Cleavage with Quantum Dots. *Chem. Mater.* **31**, 2677–2682 (2019).

269. Robatjazi, H. *et al.* Plasmon-induced selective carbon dioxide conversion on earth-abundant aluminum-cuprous oxide antenna-reactor nanoparticles. *Nat Commun* **8**, 1–10 (2017).

270. Erickson, D., Sinton, D. & Psaltis, D. Optofluidics for energy applications. *Nature Photon* **5**, 583–590 (2011).

271. Adleman, J. R., Boyd, D. A., Goodwin, D. G. & Psaltis, D. Heterogenous Catalysis Mediated by Plasmon Heating. *Nano Lett.* **9**, 4417–4423 (2009).

272. Boyd, D. A., Greengard, L., Brongersma, M., El-Naggar, M. Y. & Goodwin, D. G. Plasmon-Assisted Chemical Vapor Deposition. *Nano Lett.* **6**, 2592–2597 (2006).

273. Cao, L., Barsic, D. N., Guichard, A. R. & Brongersma, M. L. Plasmon-Assisted Local Temperature Control to Pattern Individual Semiconductor Nanowires and Carbon Nanotubes. *Nano Lett.* **7**, 3523–3527 (2007).

274. Neumann, O. *et al.* Solar Vapor Generation Enabled by Nanoparticles. *ACS Nano* **7**, 42–49 (2013).

275. Fang, Z. *et al.* Evolution of Light-Induced Vapor Generation at a Liquid-Immersed Metallic Nanoparticle. *Nano Lett.* **13**, 1736–1742 (2013).

276. Lukianova-Hleb, E. *et al.* Plasmonic Nanobubbles as Transient Vapor Nanobubbles Generated around Plasmonic Nanoparticles. *ACS Nano* **4**, 2109–2123 (2010).

277. Baral, S., Green, A. J., Livshits, M. Y., Govorov, A. O. & Richardson, H. H. Comparison of Vapor Formation of Water at the Solid/Water Interface to Colloidal Solutions Using Optically Excited Gold Nanostructures. *ACS Nano* **8**, 1439–1448 (2014).

278. Richardson, H. H. *et al.* Thermooptical Properties of Gold Nanoparticles Embedded in Ice: Characterization of Heat Generation and Melting. *Nano Lett.* **6**, 783–788 (2006).

279. Jin, R. *et al.* Photoinduced Conversion of Silver Nanospheres to Nanoprisms. *Science* **294**, 1901–1903 (2001).

280. Hogan, N. J. *et al.* Nanoparticles Heat through Light Localization. *Nano Lett.* **14**, 4640–4645 (2014).

281. Neumann, O. *et al.* Compact solar autoclave based on steam generation using broadband light-harvesting nanoparticles. *PNAS* **110**, 11677–11681 (2013).

282. Nanophotonics-enabled solar membrane distillation for off-grid water purification | PNAS. https://www.pnas.org/content/114/27/6936.short.

283. Petrova, H. *et al.* On the temperature stability of gold nanorods: comparison between thermal and ultrafast laser-induced heating. *Phys. Chem. Chem. Phys.* **8**, 814–821 (2006).

284. Ni, W., Ba, H., Lutich, A. A., Jäckel, F. & Feldmann, J. Enhancing Single-Nanoparticle Surface-Chemistry by Plasmonic Overheating in an Optical Trap. *Nano Lett.* **12**, 4647–4650 (2012).

285. Kyrsting, A., Bendix, P. M., Stamou, D. G. & Oddershede, L. B. Heat Profiling of Three-Dimensionally Optically Trapped Gold Nanoparticles using Vesicle Cargo Release. *Nano Lett.* **11**, 888–892 (2011).

286. Carlson, M. T., Green, A. J. & Richardson, H. H. Superheating Water by CW Excitation of Gold Nanodots. *Nano Lett.* **12**, 1534–1537 (2012).

287. Robert, H. M. L. *et al.* Light-Assisted Solvothermal Chemistry Using Plasmonic Nanoparticles. *ACS Omega* **1**, 2–8 (2016).

288. Christopher, P., Xin, H. & Linic, S. Visible-light-enhanced catalytic oxidation reactions on plasmonic silver nanostructures. *Nature Chemistry* **3**, 467–472 (2011).

289. Qiu, J. & Wei, W. D. Surface Plasmon-Mediated Photothermal Chemistry. *J. Phys. Chem. C* **118**, 20735–20749 (2014).

290. Hiruma, K. *et al.* Growth and optical properties of nanometer-scale GaAs and InAs whiskers. *Journal of Applied Physics* **77**, 447–462 (1995).

291. Yu, H., Li, J., Loomis, R. A., Wang, L.-W. & Buhro, W. E. Two- versus three-dimensional quantum confinement in indium phosphide wires and dots. *Nature Mater* **2**, 517–520 (2003).

292. Hanrath, T. & Korgel, B. A. Nucleation and Growth of Germanium Nanowires Seeded by Organic Monolayer-Coated Gold Nanocrystals. *J. Am. Chem. Soc.* **124**, 1424–1429 (2002).

293. Chen, X., Liu, R., Qiao, S., Mao, J. & Du, X. Synthesis of cadmium chalcogenides nanowires via laser-activated gold catalysts in solution. *Materials Chemistry and Physics* **212**, 408–414 (2018).

294. Huang, C., Mao, J., Chen, X. M., Yang, J. & Du, X. W. Laser-activated gold catalysts for liquid-phase growth of cadmium selenide nanowires. *Chem. Commun.* **51**, 2145–2148 (2015).

295. Chen, X.-M. *et al.* Laser-driven absorption/desorption of catalysts for producing nanowire arrays in solution. *Journal of Materials Chemistry A* **4**, 379–383 (2016).

296. Yu, H. *et al.* Cadmium Selenide Quantum Wires and the Transition from 3D to 2D Confinement. *J. Am. Chem. Soc.* **125**, 16168–16169 (2003).

297. Hanrath, T. & Korgel, B. A. Supercritical Fluid–Liquid–Solid (SFLS) Synthesis of Si and Ge Nanowires Seeded by Colloidal Metal Nanocrystals. *Advanced Materials* **15**, 437–440 (2003).

298. Chockla, A. M., Harris, J. T. & Korgel, B. A. Colloidal Synthesis of Germanium Nanorods. *Chem. Mater.* **23**, 1964–1970 (2011).

299. Hanrath, T. & Korgel, B. A. Crystallography and Surface Faceting of Germanium Nanowires. *Small* **1**, 717–721 (2005).

300. Sun, X., Calebotta, G., Yu, B., Selvaduray, G. & Meyyappan, M. Synthesis of germanium nanowires on insulator catalyzed by indium or antimony. *Journal of Vacuum Science & Technology B: Microelectronics and Nanometer Structures Processing, Measurement, and Phenomena* **25**, 415–420 (2007).

301. Sun, J. & Buhro, W. E. The Use of Single-Source Precursors for the Solution–Liquid–Solid Growth of Metal Sulfide Semiconductor Nanowires. *Angewandte Chemie International Edition* **47**, 3215–3218 (2008).

302. Barrelet, C. J., Wu, Y., Bell, D. C. & Lieber, C. M. Synthesis of CdS and ZnS Nanowires Using Single-Source Molecular Precursors. *J. Am. Chem. Soc.* **125**, 11498–11499 (2003).

303. Malik, M. A., Afzaal, M. & O'Brien, P. Precursor Chemistry for Main Group Elements in Semiconducting Materials. *Chem. Rev.* **110**, 4417–4446 (2010).

304. Kandel, K. P., Pietsch, U., Li, Z. & Öztürk, Ö. K. Doping induced structural changes in colloidal semiconductor nanowires. *Phys. Chem. Chem. Phys.* **15**, 4444–4450 (2013).

305. Wang, Z. *et al.* Solution–Liquid–Solid Synthesis of Semiconductor Nanowires Using Clusters as Single-Source Precursors. *Small* **7**, 2464–2468 (2011).

306. Wooten, A. J., Werder, D. J., Williams, D. J., Casson, J. L. & Hollingsworth, J. A. Solution−Liquid−Solid Growth of Ternary Cu−In−Se Semiconductor Nanowires from Multiple- and Single-Source Precursors. *J. Am. Chem. Soc.* **131**, 16177–16188 (2009).

307. Brust, M., Walker, M. & Bethell, D. Synthesis of alkanethiol passivated Au nanocrystals. doi:10.1039/C39940000801.

308. He, M., Protesescu, L., Caputo, R., Krumeich, F. & Kovalenko, M. V. A General Synthesis Strategy for Monodisperse Metallic and Metalloid Nanoparticles (In, Ga, Bi, Sb, Zn, Cu, Sn, and Their Alloys) via in Situ Formed Metal Long-Chain Amides. *Chem. Mater.* **27**, 635–647 (2015).

309. Hendricks, M. P., Campos, M. P., Cleveland, G. T., Plante, I. J.-L. & Owen, J. S. A tunable library of substituted thiourea precursors to metal sulfide nanocrystals. *Science* **348**, 1226–1230 (2015).

310. Peng, X., Wickham, J. & Alivisatos, A. P. Kinetics of II-VI and III-V Colloidal Semiconductor Nanocrystal Growth: "Focusing" of Size Distributions. *J. Am. Chem. Soc.* **120**, 5343–5344 (1998).

311. Burda, C., Chen, X., Narayanan, R. & El-Sayed, M. A. Chemistry and Properties of Nanocrystals of Different Shapes. *Chem. Rev.* **105**, 1025–1102 (2005).

312. Tedstone, A. A., Lewis, D. J. & O'Brien, P. Synthesis, Properties, and Applications of Transition Metal-Doped Layered Transition Metal Dichalcogenides. *Chem. Mater.* **28**, 1965–1974 (2016).

313. S. Hamachi, L. *et al.* Precursor reaction kinetics control compositional grading and size of CdSe 1−x S x nanocrystal heterostructures. *Chemical Science* **10**, 6539–6552 (2019).

314. Regulacio, M. D. & Han, M.-Y. Composition-Tunable Alloyed Semiconductor Nanocrystals. *Acc. Chem. Res.* **43**, 621–630 (2010).

315. Liang, Y., Zhai, L., Zhao, X. & Xu, D. Band-Gap Engineering of Semiconductor Nanowires through Composition Modulation. *J. Phys. Chem. B* **109**, 7120–7123 (2005).

316. Dayeh, S. A., Chen, R., Ro, Y. G. & Sim, J. Progress in doping semiconductor nanowires during growth. *Materials Science in Semiconductor Processing* **62**, 135–155 (2017).

317. Cossairt, B. M., Juhas, P., Billinge, S. J. L. & Owen, J. S. Tuning the Surface Structure and Optical Properties of CdSe Clusters Using Coordination Chemistry. *J. Phys. Chem. Lett.* **2**, 3075–3080 (2011).

318. Hessel, C. M. *et al.* Synthesis of Ligand-Stabilized Silicon Nanocrystals with Size-Dependent Photoluminescence Spanning Visible to Near-Infrared Wavelengths. *Chem. Mater.* **24**, 393–401 (2012).

319. Pradhan, N., Reifsnyder, D., Xie, R., Aldana, J. & Peng, X. Surface Ligand Dynamics in Growth of Nanocrystals. *J. Am. Chem. Soc.* **129**, 9500–9509 (2007).

320. Norris, D. J. & Bawendi, M. G. Measurement and assignment of the size-dependent optical spectrum in CdSe quantum dots. *Phys. Rev. B* **53**, 16338–16346 (1996).

321. Sahu, A. *et al.* Bottom-up design of de novo thermoelectric hybrid materials using chalcogenide resurfacing. *Journal of Materials Chemistry A* **5**, 3346–3357 (2017).

322. Schwarz, K. W., Tersoff, J., Kodambaka, S. & Ross, F. M. Jumping-Catalyst Dynamics in Nanowire Growth. *Phys. Rev. Lett.* **113**, 055501 (2014).

323. Wen, C.-Y. *et al.* Formation of Compositionally Abrupt Axial Heterojunctions in Silicon-Germanium Nanowires. *Science* **326**, 1247–1250 (2009).

324. Ross, F. M., Tersoff, J. & Reuter, M. C. Sawtooth Faceting in Silicon Nanowires. *Phys. Rev. Lett.* **95**, 146104 (2005).

325. Chou, Y.-C. *et al.* Atomic-Scale Variability and Control of III-V Nanowire Growth Kinetics. *Science* **343**, 281–284 (2014).

326. Lenrick, F., Ek, M., Deppert, K., Samuelson, L. & Reine Wallenberg, L. Straight and kinked InAs nanowire growth observed in situ by transmission electron microscopy. *Nano Res.* **7**, 1188–1194 (2014).

327. Gamalski, A. D., Ducati, C. & Hofmann, S. Cyclic Supersaturation and Triple Phase Boundary Dynamics in Germanium Nanowire Growth. *J. Phys. Chem. C* **115**, 4413–4417 (2011).

328. Biswas, S. *et al.* Non-equilibrium induction of tin in germanium: towards direct bandgap Ge 1−x Sn x nanowires. *Nature Communications* **7**, 1–12 (2016).

329. Orsini, A. & Falconi, C. Real-time monitoring of the solution growth of ZnO nanorods arrays by quartz microbalances and in-situ temperature sensors. *Scientific Reports* **4**, 1–7 (2014).

330. Laocharoensuk, R. *et al.* Flow-based solution–liquid–solid nanowire synthesis. *Nature Nanotechnology* **8**, 660–666 (2013).

331. Ilavsky, J. *et al.* Development of combined microstructure and structure characterization facility for in situ and operando studies at the Advanced Photon Source. *J Appl Cryst* **51**, 867–882 (2018).

332. Ilavsky, J. & Jemian, P. R. Irena: tool suite for modeling and analysis of small-angle scattering. *J Appl Cryst* **42**, 347–353 (2009).

333. Zhang, F. *et al.* Glassy Carbon as an Absolute Intensity Calibration Standard for Small-Angle Scattering. *Metall and Mat Trans A* **41**, 1151–1158 (2010).

334. Guinier, A., Fournet, G. & Yudowitch, K. L. Small-angle scattering of X-rays. (1955).

335. Teixeira, J. Small-angle scattering by fractal systems. *J Appl Cryst* **21**, 781–785 (1988).

336. Glatter, O. & Kratky, O. *Small angle x-ray scattering*. (Academic Press, 1982).

337. Lotty, O. *et al.* Containing the catalyst: diameter controlled Ge nanowire growth. *J. Mater. Chem. C* **1**, 4450–4456 (2013).

338. Koto, M., Marshall, A. F., Goldthorpe, I. A. & McIntyre, P. C. Gold-Catalyzed Vapor–Liquid–Solid Germanium-Nanowire Nucleation on Porous Silicon. *Small* **6**, 1032–1037 (2010).

339. Hannon, J. B., Kodambaka, S., Ross, F. M. & Tromp, R. M. The influence of the surface migration of gold on the growth of silicon nanowires. *Nature* **440**, 69–71 (2006).

340. Pandres, E., Crane, M. & Pauzauskie, P. Laser-driven solution-liquid-solid growth of semiconductor nanowires. *In Preparation* (2020).

341. Maragò, O. M., Jones, P. H., Gucciardi, P. G., Volpe, G. & Ferrari, A. C. Optical trapping and manipulation of nanostructures. *Nature Nanotechnology* **8**, 807–819 (2013).

342. Ashkin, A. Acceleration and Trapping of Particles by Radiation Pressure. *Phys. Rev. Lett.* **24**, 156–159 (1970).

343. Pauzauskie, P. J. *et al.* Optical trapping and integration of semiconductor nanowire assemblies in water. *Nature Materials* **5**, 97–101 (2006).

344. Paladugu, S. *et al.* Nonadditivity of critical Casimir forces. *Nature Communications* **7**, 11403 (2016).

345. Schmidt, F. *et al.* Microscopic Engine Powered by Critical Demixing. *Phys. Rev. Lett.* **120**, 068004 (2018).

346. Black, J. W., Kamenetska, M. & Ganim, Z. An Optical Tweezers Platform for Single Molecule Force Spectroscopy in Organic Solvents. *Nano Lett.* **17**, 6598–6605 (2017).

347. Agarwal, R. *et al.* Manipulation and assembly of nanowires with holographic optical traps. *Opt. Express, OE* **13**, 8906–8912 (2005).

348. Kudo, T., Wang, S.-F., Yuyama, K. & Masuhara, H. Optical Trapping-Formed Colloidal Assembly with Horns Extended to the Outside of a Focus through Light Propagation. *Nano Lett.* **16**, 3058–3062 (2016).

349. Sangiao, S., Casado, L., Morellón, L., Ibarra, M. R. & Teresa, J. M. D. Proximity-induced superconductivity in bismuth nanostripes. *J. Phys. D: Appl. Phys.* **50**, 12LT02 (2017).

350. Kelzenberg, M. D. *et al.* Photovoltaic Measurements in Single-Nanowire Silicon Solar Cells. *Nano Lett.* **8**, 710–714 (2008).

351. Kelzenberg, M. D. *et al.* Enhanced absorption and carrier collection in Si wire arrays for photovoltaic applications. *Nature Materials* **9**, 239–244 (2010).

352. Lupan, O., Pauporté, T. & Viana, B. Low-Voltage UV-Electroluminescence from ZnO-Nanowire Array/p-GaN Light-Emitting Diodes. *Advanced Materials* **22**, 3298–3302 (2010).

353. Pal, B. N. *et al.* 'Giant' CdSe/CdS Core/Shell Nanocrystal Quantum Dots As Efficient Electroluminescent Materials: Strong Influence of Shell Thickness on Light-Emitting Diode Performance. *Nano Lett.* **12**, 331–336 (2012).

354. Kolmakov, A., Zhang, Y., Cheng, G. & Moskovits, M. Detection of CO and O2 Using Tin Oxide Nanowire Sensors. *Adv. Mater.* **15**, 997–1000 (2003).

355. Kuang, Q., Lao, C., Wang, Z. L., Xie, Z. & Zheng, L. High-Sensitivity Humidity Sensor Based on a Single SnO2 Nanowire. *J. Am. Chem. Soc.* **129**, 6070–6071 (2007).

356. Zheng, G., Patolsky, F., Cui, Y., Wang, W. U. & Lieber, C. M. Multiplexed electrical detection of cancer markers with nanowire sensor arrays. *Nature Biotechnology* **23**, 1294–1301 (2005).

357. Min, Y., Akbulut, M., Kristiansen, K., Golan, Y. & Israelachvili, J. The role of interparticle and external forces in nanoparticle assembly. *Nature Materials* **7**, 527–538 (2008).

358. Larson-Smith, K. & Pozzo, D. C. Scalable synthesis of self-assembling nanoparticle clusters based on controlled steric interactions. *Soft Matter* **7**, 5339–5347 (2011).

359. Malaquin, L., Kraus, T., Schmid, H., Delamarche, E. & Wolf, H. Controlled Particle Placement through Convective and Capillary Assembly. *Langmuir* **23**, 11513–11521 (2007).

360. Baranov, D. *et al.* Assembly of Colloidal Semiconductor Nanorods in Solution by Depletion Attraction. *Nano Lett.* **10**, 743–749 (2010).

361. Cabezas, C. A. S. *et al.* Gelation of plasmonic metal oxide nanocrystals by polymer-induced depletion attractions. *PNAS* **115**, 8925–8930 (2018).

362. Wu, Y., Fan, R. & Yang, P. Block-by-Block Growth of Single-Crystalline Si/SiGe Superlattice Nanowires. *Nano Lett.* **2**, 83–86 (2002).

363. Gudiksen, M. S., Lauhon, L. J., Wang, J., Smith, D. C. & Lieber, C. M. Growth of nanowire superlattice structures for nanoscale photonics and electronics. *Nature* **415**, 617–620 (2002).

364. Lin, L. *et al.* Opto-thermophoretic assembly of colloidal matter. *Science Advances* **3**, e1700458 (2017).

365. Gargiulo, J., Cerrota, S., Cortés, E., Violi, I. L. & Stefani, F. D. Connecting Metallic Nanoparticles by Optical Printing. *Nano Lett.* **16**, 1224–1229 (2016).

366. Gargiulo, J. *et al.* Accuracy and Mechanistic Details of Optical Printing of Single Au and Ag Nanoparticles. *ACS Nano* **11**, 9678–9688 (2017).

367. Lee, S.-W., Jo, G., Lee, T. & Lee, Y.-G. Controlled assembly of In_2O_3 nanowires on electronic circuits using scanning optical tweezers. *Opt. Express, OE* **17**, 17491–17501 (2009).

368. Kyrsting, A., Bendix, P. M., Stamou, D. G. & Oddershede, L. B. Heat Profiling of Three-Dimensionally Optically Trapped Gold Nanoparticles using Vesicle Cargo Release. *Nano Lett.* **11**, 888–892 (2011).

369. Roder, P. B., Smith, B. E., Zhou, X., Crane, M. J. & Pauzauskie, P. J. Laser refrigeration of hydrothermal nanocrystals in physiological media. *PNAS* **112**, 15024–15029 (2015).

370. Spadaro, D. *et al.* Optical Trapping of Plasmonic Mesocapsules: Enhanced Optical Forces and SERS. *J. Phys. Chem. C* **121**, 691–700 (2017).

371. Sainis, S. K., Germain, V., Mejean, C. O. & Dufresne, E. R. Electrostatic Interactions of Colloidal Particles in Nonpolar Solvents: Role of Surface Chemistry and Charge Control Agents. *Langmuir* **24**, 1160–1164 (2008).

372. Draine, B. T. & Flatau, P. J. Discrete-Dipole Approximation For Scattering Calculations. *Journal of the Optical Society of America A* **11**, 1491 (1994).

373. Chockla, A. M., Holmberg, V. C. & Korgel, B. A. Germanium Nanorod Extinction Spectra: Discrete Dipole Approximation Calculations and Experiment. *J. Phys. Chem. C* **116**, 22625–22630 (2012).

374. Roder, P. B. *et al.* Photothermal Superheating of Water with Ion-Implanted Silicon Nanowires. *Advanced Optical Materials* **3**, 1362–1367 (2015).

375. Chockla, A. M., Harris, J. T. & Korgel, B. A. Colloidal Synthesis of Germanium Nanorods. *Chem. Mater.* **23**, 1964–1970 (2011).

376. Smith, B. E., Roder, P. B., Zhou, X. & Pauzauskie, P. J. Hot Brownian thermometry and cavity-enhanced harmonic generation with nonlinear optical nanowires. *Chemical Physics Letters* **639**, 310–314 (2015).

377. Roder, P. B., Smith, B. E., Davis, E. J. & Pauzauskie, P. J. Photothermal Heating of Nanowires. *J. Phys. Chem. C* **118**, 1407–1416 (2014).

378. Comuñas, M. J. P. *et al.* Reference Correlation of the Viscosity of Squalane from 273 to 373 K at 0.1 MPa. *Journal of Physical and Chemical Reference Data* **42**, 033101 (2013).

379. Berg-Sørensen, K. & Flyvbjerg, H. Power spectrum analysis for optical tweezers. *Review of Scientific Instruments* **75**, 594–612 (2004).

380. Reece, P. J. *et al.* Characterization of Semiconductor Nanowires Using Optical Tweezers. *Nano Lett.* **11**, 2375–2381 (2011).

381. Simpson, S. H. & Hanna, S. Stability analysis and thermal motion of optically trapped nanowires. *Nanotechnology* **23**, 205502 (2012).

382. Borghese, F., Denti, P., Saija, R., Iatì, M. A. & Maragò, O. M. Radiation Torque and Force on Optically Trapped Linear Nanostructures. *Phys. Rev. Lett.* **100**, 163903 (2008).

383. Hagemann, H.-J., Gudat, W. & Kunz, C. Optical constants from the far infrared to the x-ray region: Mg, Al, Cu, Ag, Au, Bi, C, and Al_2O_3. *J. Opt. Soc. Am., JOSA* **65**, 742–744 (1975).

384. Aspnes, D. E. & Studna, A. A. Dielectric functions and optical parameters of Si, Ge, GaP, GaAs, GaSb, InP, InAs, and InSb from 1.5 to 6.0 eV. *Phys. Rev. B* **27**, 985–1009 (1983).

385. Ashkin, A., Dziedzic, J. M., Bjorkholm, J. E. & Chu, S. Observation of a single-beam gradient force optical trap for dielectric particles. *Optics Letters* **11**, 288 (1986).

386. Irrera, A. *et al.* Photonic Torque Microscopy of the Nonconservative Force Field for Optically Trapped Silicon Nanowires. *Nano Lett.* **16**, 4181–4188 (2016).

387. Schermer, R. T., Olson, C. C., Coleman, J. P. & Bucholtz, F. Laser-induced thermophoresis of individual particles in a viscous liquid. *Optics Express* **19**, 10571 (2011).

388. Peng, X. *et al.* Optothermophoretic Manipulation of Colloidal Particles in Nonionic Liquids. *J. Phys. Chem. C* (2018) doi:10.1021/acs.jpcc.8b03828.

389. Dai, H. *et al.* Ordering Ag nanowire arrays by spontaneous spreading of volatile droplet on solid surface. *Scientific Reports* **4**, 6742 (2014).

390. Irrera, A. *et al.* Size-Scaling in Optical Trapping of Silicon Nanowires. *Nano Lett.* **11**, 4879–4884 (2011).

391. Peterman, E. J. G., Gittes, F. & Schmidt, C. F. Laser-Induced Heating in Optical Traps. *Biophysical Journal* **84**, 1308–1316 (2003).

392. Kedenburg, S., Vieweg, M., Gissibl, T. & Giessen, H. Linear refractive index and absorption measurements of nonlinear optical liquids in the visible and near-infrared spectral region. *Opt. Mater. Express, OME* **2**, 1588–1611 (2012).

393. Tolić-Nørrelykke, S. F. *et al.* Calibration of optical tweezers with positional detection in the back focal plane. *Review of Scientific Instruments* **77**, 103101 (2006).

394. Rings, D., Schachoff, R., Selmke, M., Cichos, F. & Kroy, K. Hot Brownian Motion. *Phys. Rev. Lett.* **105**, 090604 (2010).

395. Crane, M. J., Zhou, X., Davis, E. J. & Pauzauskie, P. J. Photothermal Heating and Cooling of Nanostructures. *Chemistry – An Asian Journal* **13**, 2575–2586 (2018).

396. Galajda, P. & Ormos, P. Rotors produced and driven in laser tweezers with reversed direction of rotation. *Appl. Phys. Lett.* **80**, 4653–4655 (2002).

397. Grollman, R. R., Busche, J. & Ostroverkhova, O. Optical tweezers-based probe of charge transfer in organic semiconductors at microscopic scales. in vol. 9360 936016-936016–8 (2015).

398. Hertlein, C., Helden, L., Gambassi, A., Dietrich, S. & Bechinger, C. Direct measurement of critical Casimir forces. *Nature* **451**, 172–175 (2008).

399. Franosch, T. *et al.* Resonances arising from hydrodynamic memory in Brownian motion. *Nature* **478**, 85–88 (2011).

400. Tian, H., Xin, F., Wang, X., He, W. & Han, W. High capacity group-IV elements (Si, Ge, Sn) based anodes for lithium-ion batteries. *Journal of Materiomics* **1**, 153–169 (2015).

401. Liu, X. H. *et al.* Reversible Nanopore Formation in Ge Nanowires during Lithiation–Delithiation Cycling: An In Situ Transmission Electron Microscopy Study. *Nano Lett.* **11**, 3991–3997 (2011).

402. Schroder, K. *et al.* The Effect of Fluoroethylene Carbonate as an Additive on the Solid Electrolyte Interphase on Silicon Lithium-Ion Electrodes. *Chem. Mater.* **27**, 5531–5542 (2015).

403. Schroder, K. W., Dylla, A. G., Harris, S. J., Webb, L. J. & Stevenson, K. J. Role of Surface Oxides in the Formation of Solid–Electrolyte Interphases at Silicon Electrodes for Lithium-Ion Batteries. *ACS Appl. Mater. Interfaces* **6**, 21510–21524 (2014).

404. Verma, P., Maire, P. & Novák, P. A review of the features and analyses of the solid electrolyte interphase in Li-ion batteries. *Electrochimica Acta* **55**, 6332–6341 (2010).

405. Sloop, S. E., Kerr, J. B. & Kinoshita, K. The role of Li-ion battery electrolyte reactivity in performance decline and self-discharge. *Journal of Power Sources* **119**, 330–337 (2003).

406. Shi, F. *et al.* A Catalytic Path for Electrolyte Reduction in Lithium-Ion Cells Revealed by in Situ Attenuated Total Reflection-Fourier Transform Infrared Spectroscopy. *Journal of the American Chemical Society* **137**, 3181–3184 (2015).

407. Shi, F. *et al.* Identification of Diethyl 2,5-Dioxahexane Dicarboxylate and Polyethylene Carbonate as Decomposition Products of Ethylene Carbonate Based Electrolytes by Fourier Transform Infrared Spectroscopy. *The Journal of Physical Chemistry C* **118**, 14732–14738 (2014).

408. Olson, J. Z., Johansson, P. K., Castner, D. G. & Schlenker, C. W. Operando Sum-Frequency Generation Detection of Electrolyte Redox Products at Active Si Nanoparticle Li-Ion Battery Interfaces. *Chem. Mater.* **30**, 1239–1248 (2018).

409. Etacheri, V. *et al.* Effect of Fluoroethylene Carbonate (FEC) on the Performance and Surface Chemistry of Si-Nanowire Li-Ion Battery Anodes. *Langmuir* **28**, 965–976 (2012).

410. Lin, Y.-M. *et al.* High performance silicon nanoparticle anode in fluoroethylene carbonate-based electrolyte for Li-ion batteries. *Chem. Commun.* **48**, 7268–7270 (2012).

411. Liu, G. *et al.* Polymers with Tailored Electronic Structure for High Capacity Lithium Battery Electrodes. *Advanced Materials* **23**, 4679–4683 (2011).

412. Wu, H. *et al.* Stable Li-ion battery anodes by *in-situ* polymerization of conducting hydrogel to conformally coat silicon nanoparticles. *Nature Communications* **4**, 1943 (2013).

413. Erk, C., Brezesinski, T., Sommer, H., Schneider, R. & Janek, J. Toward Silicon Anodes for Next-Generation Lithium Ion Batteries: A Comparative Performance Study of Various Polymer Binders and Silicon Nanopowders. *ACS Appl. Mater. Interfaces* **5**, 7299–7307 (2013).

414. Koo, B. *et al.* A Highly Cross-Linked Polymeric Binder for High-Performance Silicon Negative Electrodes in Lithium Ion Batteries. *Angewandte Chemie International Edition* **51**, 8762–8767 (2012).

415. Komaba, S. *et al.* Comparative Study of Sodium Polyacrylate and Poly(vinylidene fluoride) as Binders for High Capacity Si–Graphite Composite Negative Electrodes in Li-Ion Batteries. *J. Phys. Chem. C* **116**, 1380–1389 (2012).

416. Favors, Z. *et al.* Towards Scalable Binderless Electrodes: Carbon Coated Silicon Nanofiber Paper via Mg Reduction of Electrospun SiO_2 Nanofibers. *Scientific Reports* **5**, 8246 (2015).

417. Kovalenko, I. *et al.* A Major Constituent of Brown Algae for Use in High-Capacity Li-Ion Batteries. *Science* **334**, 75–79 (2011).

418. Rustomji, C. S. *et al.* Liquefied gas electrolytes for electrochemical energy storage devices. *Science* **356**, eaal4263 (2017).

419. Mishra, K. *The Effect of Solvent on the Capacity Retention in a Germanium Anode for Lithium Ion Batteries*. vol. 15 (2018).

420. Michan, A. L. *et al.* Solid Electrolyte Interphase Growth and Capacity Loss in Silicon Electrodes. *Journal of the American Chemical Society* **138**, 7918–7931 (2016).

421. Nadimpalli, S. *et al. Quantifying Capacity Loss due to Solid-Electrolyte-Interphase Layer Formation on Silicon Negative Electrodes in Lithium-ion Batteries*. vol. 215 (2012).

422. Dalavi, S., Guduru, P. & Lucht, B. L. Performance Enhancing Electrolyte Additives for Lithium Ion Batteries with Silicon Anodes. *J. Electrochem. Soc.* **159**, A642–A646 (2012).

423. Ji, L. *et al.* Controlling SEI Formation on SnSb-Porous Carbon Nanofibers for Improved Na Ion Storage. *Advanced Materials* **26**, 2901–2908 (2014).

424. Xun, S. *et al.* The Effects of Native Oxide Surface Layer on the Electrochemical Performance of Si Nanoparticle-Based Electrodes. *J. Electrochem. Soc.* **158**, A1260–A1266 (2011).

425. He, Y. *et al.* In Situ Transmission Electron Microscopy Probing of Native Oxide and Artificial Layers on Silicon Nanoparticles for Lithium Ion Batteries. *ACS Nano* **8**, 11816–11823 (2014).

426. Schroder, K. W., Celio, H., Webb, L. J. & Stevenson, K. J. Examining Solid Electrolyte Interphase Formation on Crystalline Silicon Electrodes: Influence of Electrochemical Preparation and Ambient Exposure Conditions. *J. Phys. Chem. C* **116**, 19737–19747 (2012).

427. Xu, W., Vegunta, S. S. S. & Flake, J. C. Surface-modified silicon nanowire anodes for lithium-ion batteries. *Journal of Power Sources* **196**, 8583–8589 (2011).

428. Michan, A. L., Leskes, M. & Grey, C. P. Voltage Dependent Solid Electrolyte Interphase Formation in Silicon Electrodes: Monitoring the Formation of Organic Decomposition Products. *Chemistry of Materials* **28**, 385–398 (2016).

429. Michan, A. L. *et al.* Fluoroethylene Carbonate and Vinylene Carbonate Reduction: Understanding Lithium-Ion Battery Electrolyte Additives and Solid Electrolyte Interphase Formation. *Chem. Mater.* **28**, 8149–8159 (2016).

430. Jin, Y. *et al.* Understanding Fluoroethylene Carbonate and Vinylene Carbonate Based Electrolytes for Si Anodes in Lithium Ion Batteries with NMR Spectroscopy. *Journal of the American Chemical Society* **140**, 9854–9867 (2018).

431. Jin, Y. *et al.* Identifying the Structural Basis for the Increased Stability of the Solid Electrolyte Interphase Formed on Silicon with the Additive Fluoroethylene Carbonate. *Journal of the American Chemical Society* **139**, 14992–15004 (2017).

432. Jaumann, T. *et al.* Lifetime vs. rate capability: Understanding the role of FEC and VC in high-energy Li-ion batteries with nano-silicon anodes. *Energy Storage Materials* **6**, 26–35 (2017).

433. Nie, M. *et al.* Effect of Vinylene Carbonate and Fluoroethylene Carbonate on SEI Formation on Graphitic Anodes in Li-Ion Batteries. *J. Electrochem. Soc.* **162**, A7008–A7014 (2015).

434. Nguyen, C. C. & Lucht, B. L. Comparative Study of Fluoroethylene Carbonate and Vinylene Carbonate for Silicon Anodes in Lithium Ion Batteries. *Journal of The Electrochemical Society* **161**, A1933–A1938 (2014).

435. Veith, G. M. *et al.* Determination of the Solid Electrolyte Interphase Structure Grown on a Silicon Electrode Using a Fluoroethylene Carbonate Additive. *Scientific Reports* **7**, 6326 (2017).

436. Wang, A., Kadam, S., Li, H., Shi, S. & Qi, Y. Review on modeling of the anode solid electrolyte interphase (SEI) for lithium-ion batteries. *npj Computational Materials* **4**, 15 (2018).

437. Sina, M. *et al.* Direct Visualization of the Solid Electrolyte Interphase and Its Effects on Silicon Electrochemical Performance. *Adv. Mater. Interfaces* **3**, n/a-n/a (2016).

438. Philippe, B. *et al.* Nanosilicon Electrodes for Lithium-Ion Batteries: Interfacial Mechanisms Studied by Hard and Soft X-ray Photoelectron Spectroscopy. *Chemistry of Materials* **24**, 1107–1115 (2012).

439. Radvanyi, E., De Vito, E., Porcher, W. & Jouanneau Si Larbi, S. An XPS/AES comparative study of the surface behaviour of nano-silicon anodes for Li-ion batteries. *Journal of Analytical Atomic Spectrometry* **29**, 1120–1131 (2014).

440. Aghazadeh Meshgi, M. *et al.* Rapid, Low-Temperature Synthesis of Germanium Nanowires from Oligosilylgermane Precursors. *Chem. Mater.* **29**, 4351–4360 (2017).

441. Lim, L. Y., Liu, N., Cui, Y. & Toney, M. F. Understanding Phase Transformation in Crystalline Ge Anodes for Li-Ion Batteries. *Chemistry of Materials* **26**, 3739–3746 (2014).

442. Lim, L. Y., Fan, S., Hng, H. H. & Toney, M. F. Storage Capacity and Cycling Stability in Ge Anodes: Relationship of Anode Structure and Cycling Rate. *Adv. Energy Mater.* **5**, n/a-n/a (2015).

443. Misra, S. *et al.* In Situ X-ray Diffraction Studies of (De)lithiation Mechanism in Silicon Nanowire Anodes. *ACS Nano* **6**, 5465–5473 (2012).

444. Hu, B. *et al.* The existence of optimal molecular weight for poly(acrylic acid) binders in silicon/graphite composite anode for lithium-ion batteries. *Journal of Power Sources* **378**, 671–676 (2018).

445. Huang, H. *The Effect of Commercialized Binders on Silicon Oxide Anode Material for High Capacity Lithium ion Batteries*. vol. 11 (2016).

446. Magasinski, A. *et al.* Toward Efficient Binders for Li-Ion Battery Si-Based Anodes: Polyacrylic Acid. *ACS Appl. Mater. Interfaces* **2**, 3004–3010 (2010).

447. Porcher, W. *et al.* Understanding Polyacrylic Acid and Lithium Polyacrylate Binder Behavior in Silicon Based Electrodes for Li-Ion Batteries. *Journal of The Electrochemical Society* **164**, A3633–A3640 (2017).

448. Urbanski, A. *et al.* An Efficient Two-Polymer Binder for High-Performance Silicon Nanoparticle-Based Lithium-Ion Batteries: A Systematic Case Study with Commercial Polyacrylic Acid and Polyvinyl Butyral Polymers. *Journal of The Electrochemical Society* **166**, A5275–A5286 (2019).

449. Lee, J.-H., Paik, U., Hackley, V. A. & Choi, Y.-M. Effect of poly(acrylic acid) on adhesion strength and electrochemical performance of natural graphite negative electrode for lithium-ion batteries. *Journal of Power Sources* **161**, 612–616 (2006).

450. Liu, T.-J., Tiu, C., Chen, L.-C. & Liu, D. The Influence of Slurry Rheology on Lithium-ion Electrode Processing. in *Printed Batteries* 63–79 (Wiley-Blackwell, 2018). doi:10.1002/9781119287902.ch3.

451. Assresahegn, B. D. & Bélanger, D. Synthesis of binder-like molecules covalently linked to silicon nanoparticles and application as anode material for lithium-ion batteries without the use of electrolyte additives. *Journal of Power Sources* **345**, 190–201 (2017).

452. Philippe, B. *et al.* Role of the LiPF6 Salt for the Long-Term Stability of Silicon Electrodes in Li-Ion Batteries – A Photoelectron Spectroscopy Study. *Chem. Mater.* **25**, 394–404 (2013).

453. Kennedy, T. *et al.* Nanowire Heterostructures Comprising Germanium Stems and Silicon Branches as High-Capacity Li-Ion Anodes with Tunable Rate Capability. *ACS Nano* **9**, 7456–7465 (2015).

454. Abel, P. R. *et al.* Nanostructured Si(1-x)Gex for Tunable Thin Film Lithium-Ion Battery Anodes. *ACS Nano* **7**, 2249–2257 (2013).

455. Lu, Q. *et al.* Raman Scattering from Si1-xGex Alloy Nanowires. *J. Phys. Chem. C* **112**, 3209–3215 (2008).

456. Koschinski, W., Dettmer, K. & Kessler, F. R. Investigation of Si1−xGex films and SimGen superlattices by x-ray diffraction. *Journal of Applied Physics* **72**, 471–477 (1992).

457. Lu, X., Harris, J. T., Villarreal, J. E., Chockla, A. M. & Korgel, B. A. Enhanced Nickel-Seeded Synthesis of Germanium Nanowires. *Chem. Mater.* **25**, 2172–2177 (2013).

458. Givargizov, E. I. & Givargizov, E. I. *Highly anisotropic crystals*. vol. 3 (D Reidel Pub Co, 1987).

459. Dayeh, S. A. & Picraux, S. T. Direct Observation of Nanoscale Size Effects in Ge Semiconductor Nanowire Growth. *Nano Lett.* **10**, 4032–4039 (2010).

460. Liu, D. *et al.* Review of Recent Development of In Situ/Operando Characterization Techniques for Lithium Battery Research. *Advanced Materials* **31**, 1806620 (2019).

461. Crane, M. J. *et al.* Photothermal effects during nanodiamond synthesis from a carbon aerogel in a laser-heated diamond anvil cell. *Diamond and Related Materials* **87**, 134–142 (2018).

462. Crane, M. J., Pandres, E. P., Davis, E. J., Holmberg, V. C. & Pauzauskie, P. J. Optically oriented attachment of nanoscale metal-semiconductor heterostructures in organic solvents via photonic nanosoldering. *Nat Commun* **10**, 1–7 (2019).

463. Graetz, L. Ueber die Wärmeleitungsfähigkeit von Flüssigkeiten. *Annalen der Physik* **254**, 79–94 (1882).

464. Davis, E. J. Exact solutions for a class of heat and mass transfer problems. *The Canadian Journal of Chemical Engineering* **51**, 562–572 (1973).

465. Papoutsakis, E. & Ramkrishna, D. Heat Transfer in a Capillary Flow Emerging from a Reservoir. *J. Heat Transfer* **103**, 429–435 (1981).

466. Jerri, A. J. & Davis, E. J. Application of the sampling theorem to boundary value problems. *J Eng Math* **8**, 1–8 (1974).

467. Bird, R. B., Stewart, W. E., Lightfoot, E. N. & Klingenberg, D. J. *Introductory Transport Phenomena*. (Wiley, 2014).

468. Mylona, S. K. *et al.* Reference Correlations for the Density and Viscosity of Squalane from 273 to 473 K at Pressures to 200 MPa. *Journal of Physical and Chemical Reference Data* **43**, 013104 (2014).

469. Mingo, N., Yang, L., Li, D. & Majumdar, A. Predicting the Thermal Conductivity of Si and Ge Nanowires. *Nano Lett.* **3**, 1713–1716 (2003).

470. Draine, B. T. & Flatau, P. J. User Guide for the Discrete Dipole Approximation Code DDSCAT 7.3. *arXiv:1305.6497 [astro-ph, physics:cond-mat, physics:physics]* (2013).

471. Yan, C. & Lee, P. S. Bismuth-Catalyzed Growth of Germanium Nanowires in Vapor Phase. *J. Phys. Chem. C* **113**, 2208–2211 (2009).

472. Niklasson, G. A., Granqvist, C. G. & Hunderi, O. Effective medium models for the optical properties of inhomogeneous materials. *Appl. Opt., AO* **20**, 26–30 (1981).

APPENDIX A

Table A.1. Synthetic parameters of laser-driven nanowire nanowire growth for Bi-seeded CdSe, Bi-seeded Ge, and In-seeded Ge, including concentrations, irradiation power, and irradiation time.

Material system	[Bi] (mol/L)	[In] (mol/L)	[Cd-oleate] (mol/L)	[TOP:Se] (mol/L)	[DPG] (mol/L)	Laser Power (W)	Time (min)
Bi-seeded CdSe	1.07E-03	---	4.83E-02	5.49E-01	---	15	20
Bi-seeded Ge	1.07E-03	---	---	---	8.91E-01	40	15
In-seeded Ge	---	2.03E-3	---	---	8.91E-01	20	5

Isolated nanocrystal and nanowire heating

To analyze heating of an isolated nanocrystal and metal-tipped nanowire under irradiation, we employed the analytical solutions outlined in previous publications.[461,462] In the first step, we calculated the internal electric field amplitude in a spherical nanocrystal and in a metal-tipped nanowire, using Mie theory and the discrete dipole approximation implemented in Discrete Dipole Scattering (DDSCAT) software, respectively[372]. We then converted these internal electric fields to volumetric source terms for heat transfer analysis. For the nanocrystal sphere, the heat transfer coefficient, h, is defined by the Nusselt number, $Nu = hL/k$, where L is a characteristic length of the particle and k_s is the solution thermal conductivity. For a sphere[461] suspended in an infinite bath, $Nu = 2.0$; for a vertical nanowire[377] suspended in an infinite bath, $Nu = 0.32$. In calculations of both nanocrystal and nanowire temperatures, we used the highest irradiance and widest diameters. Because these length scales are far below the wavelength of light in any medium, there are no morphology-dependent resonances, and the predicted temperatures are maximized. Similarly, for the nanowire, we calculated the absorption for the largest project surface area of nanowire to achieve largest volumetric source and averaged two orthogonal linear polarizations to refect the unpolarized near-infrared heating laser.

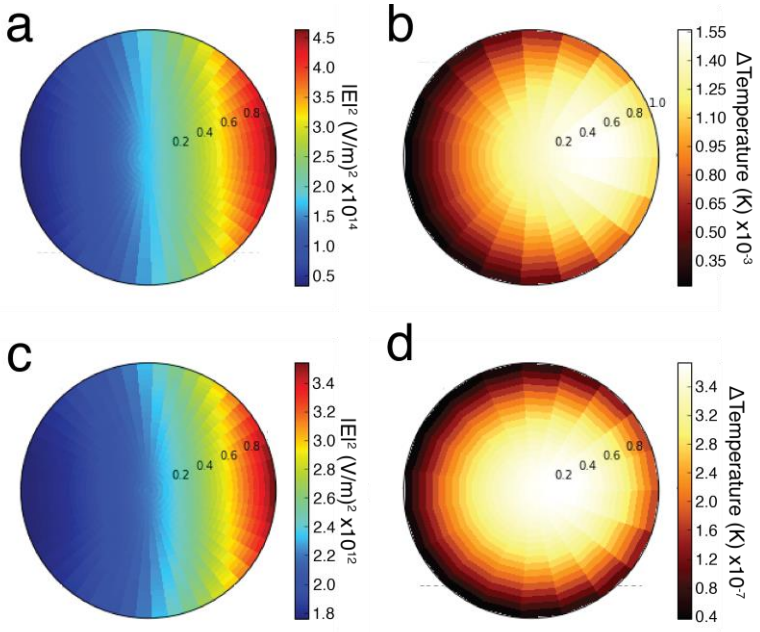

Figure A.1. (a, c) Internal electric fields and (b, d) the resulting predicted temperature distributions within (a, b) a 50 nm diameter bismuth nanocrystal and (c, d) a 90 nm diameter indium nanocrystal. The irradiances for the bismuth and indium nanocrystal calculations were $3.2 \cdot 10^{-6}$ and $1.6 \cdot 10^{-6}$ W m^{-2}, respectively.

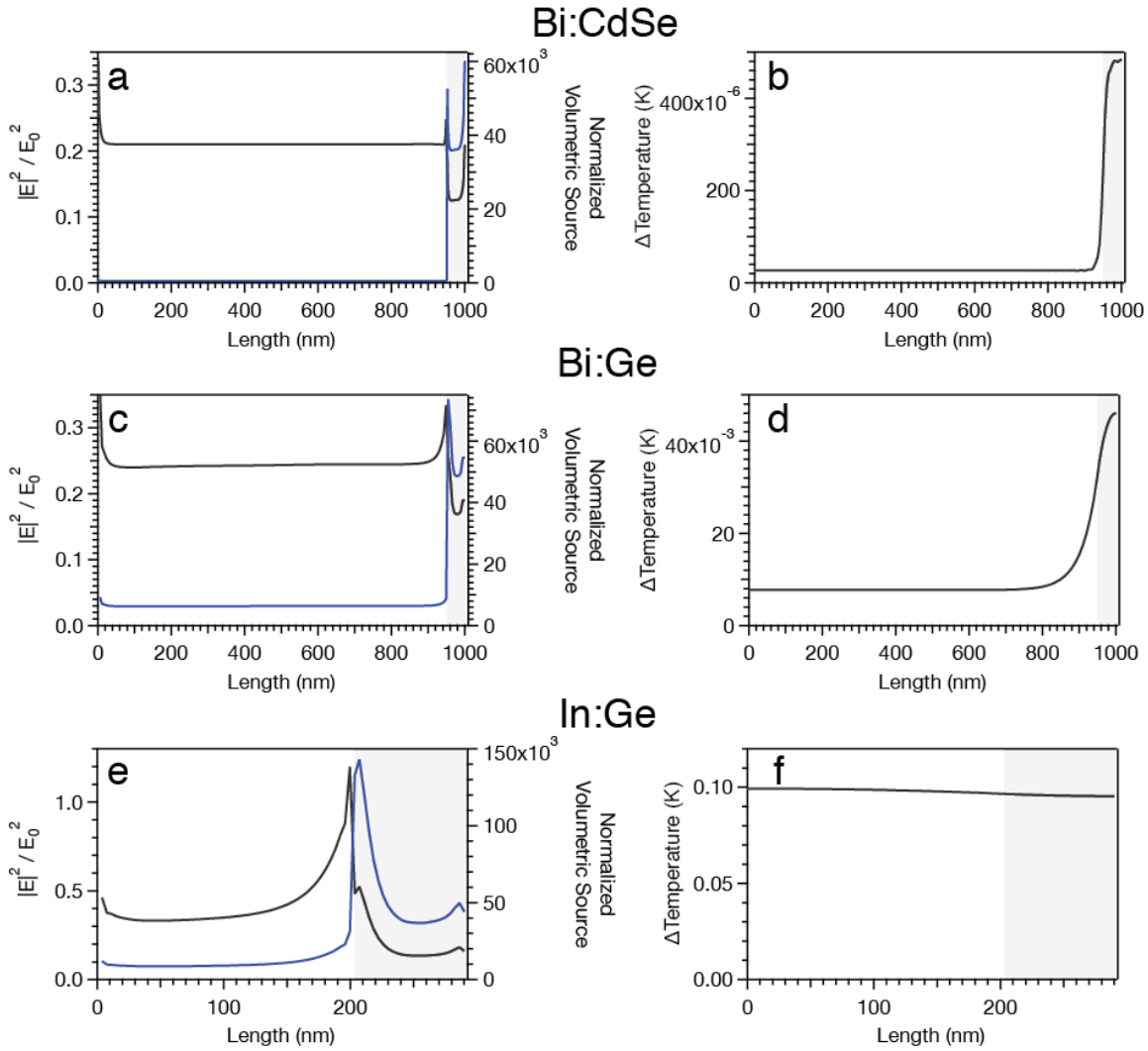

Figure A.2. (a, c, e) DDSCAT calculated normalized electric field and normalized volumetric source upon illumination of a (a) bismuth-seeded cadmium selenide nanowire with a 12 nm diameter and 1000 nm length, (b) a bismuth-seeded germanium nanowire with a 40 nm diameter and 1000 nm length, and (c) an indium-seeded germanium nanowire with an 80 nm diameter and 290 nm length. The light grey areas illustrate the seed portion of each respective nanowire. (b, d, f) Calculated temperature changes along the length of the nanowire and seed for (b) bismuth-seeded cadmium selenide, (d) bismuth-seeded germanium, and (f) indium-seeded germanium nanowires

Due to the larger complex refractive index of bismuth and indium compared to germanium and cadmium selenide, the magnitude of absorbed light and the resulting volumetric source terms are

significantly larger in these regions. The increased magnitude of absorbed light correlates with higher increases in temperatures for (b) bismuth-seeded cadmium selenide and (d) bismuth-seeded germanium nanowires. Conversely, this effect is not observed in (e) indium-seeded germanium due to the high thermal conductivity of indium (f). The plotted volumetric sources were normalized to the volumetric source produced with E_0 = 1 V m^{-1}. The irradiances for the bismuth and indium nanocrystal-seeded nanowire calculations were $3.2 \cdot 10^{-6}$ and $1.6 \cdot 10^{-6}$ W m^{-2}, respectively.

Heat Transfer Analysis Flow Reactor

Figure 2.14 shows the unsteady state development of the temperature distribution in the heated tube. To elucidate the effects of the numerous parameters on the heating process it is useful to analyze a quasi-steady state model of the system. The energy equation that describes the temperature distribution is given by

$$2\rho_s C_s v_z \frac{\partial T}{\partial z} = k_s \left[\frac{1}{r}\frac{\partial}{\partial r}\left(r\frac{\partial T}{\partial r}\right) + \frac{\partial^2 T}{\partial r^2}\right] + S, \qquad \text{(A.1)}$$

in which ρ_s, C_s, and k_s are the density, specific heat, and the thermal conductivity of the fluid, respectively, v_z is the velocity of the fluid, r is the radial position, and R_1 is the inner radius of the tube (R_1 = 1.615 mm). The heat source function, S, is the rate of heat generation per unit volume due to the laser illumination over the region $z_1 \leq z \leq z_2$. The dominant resistance to heat transfer to the surroundings is that between the outer surface (at r = R_2 = 2 mm) and the surrounding air at temperature T_∞, so the boundary condition at the surface is given by

$$-k_s \frac{\partial T}{\partial z}(R_2, z) = h[T(R_1, z) - T_\infty], \qquad \text{(A.2)}$$

where the heat transfer coefficient is given by[377],

$$2\frac{R_2 h}{k_{air}} = 0.32. \tag{A.3}$$

There is a very extensive literature related to this type of problem since Graetz[463] analyzed heat transfer to a laminar flow in 1882. Consequently, problems of this type are called Graetz problems or extended Graetz problems depending on the boundary conditions and the inclusion of axial conduction. In the absence of axial conduction analytical solutions of Graetz-like problems, involving Kummer's function (the confluent hypergeometric function), have been developed by Davis[464]. Papoutsakis and Ramkrishna[465] analyzed heat transfer in a capillary flow (Poiseuille flow) with the wall boundary condition given by Eq. (A.2), the Robin boundary condition. They solved the problem in the semi-infinite axial domain ($0 \leq z \rightarrow \infty$) and pointed out the difficulties associated with this problem.

The velocity distribution at the inlet to the capillary tube is approximately uniform (plug flow), and far from the inlet Poiseuille flow occurs. We approximate the flow as plug flow here. It is convenient to write the energy equation in terms of dimensionless coordinates defined by

$$\xi = \frac{r}{R_1}, \zeta = \frac{(z - z_1) < v_z >}{R_1 Pe} \tag{A.4}$$

in which $< v_z >$ is the mean velocity, and the Peclet number is defined by

$$Pe = \frac{R_1 < v_z > \rho_s C_s}{k_s}. \tag{A.5}$$

Let $\theta = T - T_\infty$ and transform the energy equation to give

$$\frac{\partial \theta}{\partial \zeta} = \frac{1}{\xi}\frac{\partial}{\partial \xi}\left(\xi \frac{\partial \theta}{\partial \xi}\right) + \frac{1}{Pe^2}\frac{\partial^2 \theta}{\partial \zeta^2} + \sigma, \tag{A.6}$$

in which the dimensionless heat source function is

$$\sigma = \frac{S{R_1}^2}{k_s}. \tag{A.7}$$

The wall boundary condition becomes

$$\frac{\partial \theta}{\partial \xi}(1,\zeta) = -Bi\,\theta(1,\zeta), \tag{A.8}$$

where the Biot number is

$$Bi = \frac{hR_1}{k_s} = \frac{0.16k_{air}R_1}{R_2k_s}. \tag{A.9}$$

For the geometry and properties of our capillary system we obtain Pe = 1.81. This low Peclet number indicates that there is significant axial conduction. Jerri and Davis[466] solved Eq. (A.6) for a constant wall temperature at $T > 0$, showing that there is a very large effect on the temperature distribution for Pe < 10. That large effect was also demonstrated by Papoutsakis and Ramkrishna[465] with Poiseuille flow for small Peclet numbers.

The heated region here extended from approximately z_1 = 10.5 mm to z_2 = 14.5 mm, that is from ζ = 0 to 1.77. Because the capillary tube was substantially longer (L = 40 mm) than the heated zone we consider three zones (i) $-\infty < \zeta \leq 0$ in which $S = 0$, (ii) $0 \leq \zeta \leq 1.77$, in which S = constant, and (iii) $1.77 < \zeta < \infty$ in which $S = 0$.

At positions ζ = 0 and z_2 we must apply compatibility conditions, that is, continuity of temperature and heat flux across these boundaries. These conditions are

$$\theta^-(\xi,0) = \theta^*(\xi,0), \theta^*(\xi,0) = \theta^+(\xi,0), \frac{\partial \theta^-}{\partial \zeta}(\xi,0) = \frac{\partial \theta^*}{\partial \zeta}(\xi,0), \quad \frac{\partial \theta^*}{\partial \zeta}(\xi,0) = \frac{\partial \theta^+}{\partial \zeta}(\xi,0). \tag{A.10}$$

In addition, we have the conditions

$$\theta^-(\xi,\zeta \to -\infty) = \text{bounded, and } \theta^+(\xi,\zeta \to -\infty) = \text{bounded}. \tag{A.11}$$

We look for solutions of the form

$$\theta(\xi,\zeta) = X(\xi)e^{(r\zeta)}, \tag{A.12}$$

where $X_j(\xi)$ are eigenfunctions defined by

$$X_j(\xi) = J_0(\lambda_j\xi) \text{ with } j = l, m, \text{or } n, \tag{A.13}$$

in which the eigenvalues satisfy the transcendental equation

$$J_1(\lambda_j) - \frac{Bi}{\lambda_j}J_0(\lambda_j) = 0. \tag{A.14}$$

This yields the following solutions

$$\theta^- = \sum_{n=1}^{\infty} A_n^- e^{r_n\zeta}X_n(\lambda_n\xi) \tag{A.15}$$

With

$$r_n = \frac{Pe^2}{2}\left[1 - \sqrt{1 + 4\left({}^{\lambda_n}/_{Pe}\right)^2}\right], \tag{A.16}$$

$$\theta^* = \sum_{m=1}^{\infty}\left[A_m^* e^{r_m\zeta} + B_m^* e^{r_n\zeta} + C_m\right]X_n(\lambda_n\xi), \tag{A.17}$$

And

$$\theta^+ = \sum_{n=1}^{\infty} A_l^+ e^{r_n\zeta}X_n(\lambda_n\xi) \tag{A.18}$$

in which

$$r_m = \frac{Pe^2}{2}\left[1 + \sqrt{1 + 4\left({}^{\lambda_m}/_{Pe}\right)^2}\right], \tag{A.19}$$

I_m is the integral

$$I_m = \int_0^1 \xi \frac{X_m(\lambda_m\xi)}{\|X_m\|^2}\,d\xi, \tag{A.20}$$

and the norms squared are given by

$$\|X_m\|^2 = \int_0^1 \xi [X_m(\lambda_m \xi)]^2 d\xi \tag{A.21}$$

which is based on the orthogonality property

$$\int_0^1 \xi X_m(\lambda_m \xi) X_j(\lambda_j \xi) d\xi = \begin{cases} 0 \text{ for } j \neq m \\ \|X_m\| \text{ for } j = m \end{cases} \tag{A.22}$$

This orthogonality property can be used in the compatibility conditions to determine a set of equations relating coefficients A_n^-, A_m^*, B_m^* and A_l^+. For example, the first compatibility condition becomes

$$\theta^-(\xi, 0) = \sum_{n=1}^{\infty} A_n^- X_n(\lambda_n \xi) = \theta^*(\xi, 0) = \sum_{m=1}^{\infty} \left[\left(A_m^* + B_m^* + \frac{\sigma I_m}{\lambda_m^2} \right) \right] X_m(\lambda_m \xi). \tag{A.23}$$

Applying the orthogonality of $X_n(\xi)$ to each term of the right hand side of Eq. (A.23) one obtains

$$\begin{aligned} A_n^- \|X_n\|^2 &= \left(A_m^* + B_m^* + \frac{\sigma I_m}{\lambda_m^2} \right) \int_0^1 \xi X_n(\xi) X_m(\xi) d\xi \\ &= \left(\left(A_m^* + B_m^* + \frac{\sigma I_m}{\lambda_m^2} \right) \right) \|X_n\|^2, \end{aligned} \tag{A.24}$$

With $n = m$.

The temperature distributions for the three zones are presented in Figure 2.14 for various times and source functions based on the best-fit absorption efficiency, ε_{abs}. The source function S in Eq. (A.1) is given by the product of the laser wattage, P = 7.5 W here, and the absorption efficiency of the system divided by the volume illuminated, that is,

$$S = \frac{P \, \varepsilon_{abs}}{\pi R_1^2 (z_2 - z_1)}. \tag{A.25}$$

The thermal conductivity of solutions containing dispersions of nanoparticles varies significantly with both concentration, morphology, and thermal conductivity of the constituent nanomaterials. For example, the thermal conductivity a polymer matrix increased more than

1000% upon adding copper nanowires at volume fractions equivalent to those in these experiments. Thus, we varied the thermal conductivity of the nanowire solution from 0.10 to 1.0 W/mK to account for this variation. Both the absorption efficiency and thermal conductivity increase as the reaction proceeds, further confirming photothermally driven nanowire reaction.

Applying orthogonality to solve for the coefficients $A_n^-, A_m^*, B_m^*, and\ A_l^+$ yields

$$A_n = \frac{C_m}{2}\left(1 - e^{-r_m\zeta_2}\right)\left(\frac{r_n}{r_n - r_m}\right) \tag{A.26a}$$

$$A_m^* = -C_m e^{\left(-r_m^+\zeta_2\right)}\left(\frac{r_n}{r_n - r_m}\right) \tag{A.26b}$$

$$B_m^* = C_m\left(\frac{r_m}{r_n - r_m}\right) \tag{A.26c}$$

$$A_l^+ = C_m\left(1 - e^{\left(-r_n\zeta_2\right)}\right)\left(\frac{r_m}{r_n - r_m}\right), \tag{A.26d}$$

where $C_m = \sigma I_m/\lambda_m^2$.

Table A.2. Biot number, absorption efficiency, and thermal conductivity used for analytical heat transport fits in modeling the flow reactor.

Heating Time (min)	Biot Number (-)	ε_{abs}	k_s
1	0.035	0.248	0.100
2	0.056	0.327	0.123
5	0.005	0.494	0.860

APPENDIX B

Table B.1. Precursor concentrations of nanowire growth solutions and laser powers used to irradiate nanowire growth solutions.

Sample	[Bi] (mol/L)	Bi NC Optical Density @808nm	[Cd oleate] (mol/L)	[TOP:Se] (mol/L)	Laser Power (W)
0	3.77E-04	0.35	5.17E-02	5.87E-01	2
1	3.77E-04	0.35	5.17E-02	5.87E-01	2
2	1.88E-04	0.14	5.17E-02	5.87E-01	2
3	1.88E-05	0.05	5.17E-02	5.87E-01	2
4	3.77E-04	0.35	5.17E-02	5.87E-01	1
5	3.77E-04	0.35	5.17E-02	5.87E-01	1.5

Calculations to determine change in nanowire length during irradiation

In order to calculate change in CdSe nanowire length over time, it was important to first calculate the number density of bismuth nanocrystals in dispersion, prior to irradiation and nanowire growth. The initial bismuth nanocrystal number density serves as an upper limit of the number density of nanowires grown during the reaction. To calculate the number density of bismuth nanocrystals in dispersion, we first calculated the volume of a single bismuth nanocrystal, based on the radius extracted from model fits of the USAXS initial time point, prior to irradiation:

$$V_{Bi\,NC} = \frac{4}{3}\pi r^3 \tag{B.1}$$

In addition, the atomic number density of bismuth was calculated by:

$$N_{Bi} = \frac{\rho_{Bi}}{MW_{Bi}} N_{AV} \tag{B.2}$$

Which was used to calculate the atoms per nanocrystal through:

$$n_{atoms/NC} = V_{Bi\,NC}\ N_{Bi} \tag{B.3}$$

The molar bismuth concentration (C_{Bi}, mol Bi/L), which was measured through ICP-AES, was used to calculate the number density of bismuth nanocrystals in solution ($\rho_{Bi\,NCs}$, NC/volume):

$$\rho_{Bi\ NCs} = \frac{C_{Bi}\, N_{AV}}{n_{atoms/NC}} \tag{B.4}$$

However, in solution-liquid-solid semiconductor nanowire growth, nanocrystals often coalesce to form larger particles that have a log-normal distribution of diameters. In order to make a first approximation, we assumed that 10 nm bismuth nanocrystals coalesced to form 30 nm diameter bismuth nanocrystals. As a result, the final nanocrystal number density was scaled based on a ratio of the initial and final nanocrystal volumes:

$$n_{Bi\ NCs,final} = \frac{n_{Bi\ NCs,initial}}{(V_{initial}/V_{final})} \tag{B.5}$$

In addition, the volume of CdSe—the scattering material of interest—could be calculated from the volume fraction:

$$\phi = \frac{V_{CdSe}}{V_{CdSe}+V_{solvent}} \tag{B.6}$$

As a result, the average change in nanowire length could be calculated at each time point as:

$$\Delta l_{NW} = \frac{\Delta V_{CdSe}}{n_{Bi\ NCs,final}}\ \pi\, r^2 \tag{B.7}$$

APPENDIX C

Heat Transport Calculations

All of the below calculations included iterative temperature-dependent heat transfer boundary conditions; we also allowed the bismuth nanocrystal tip to vary in composition as a function temperature. The source term was calculated with a discrete dipole approximation by applying DDSCAT code in Matlab to a nanostructure being illuminated in the +Z direction, shown in Figure 4.6a.

To solve the heat transport equation, we nondimensionalized Equation 4.1 to

$$\frac{\partial\theta}{\partial\tau} = \frac{1}{\xi}\frac{\partial}{\partial\xi}\left(\xi\frac{\partial\theta}{\partial\xi}\right) + a^2\frac{\partial^2\theta}{\partial\zeta^2} + \sigma \qquad \text{(C.1)}$$

where the variables are defined as

$$\theta = \frac{T - T_\infty}{T_\infty}, \qquad \tau = \frac{\alpha t}{R^2}, \qquad \xi = \frac{r}{R}, \qquad \zeta = \frac{z}{L}, \qquad \sigma = \frac{SR^2}{\kappa T_\infty}, \qquad a = \frac{R}{L}. \qquad \text{(C.2a-f)}$$

Here, T_∞, S, R, L, and κ are the bulk fluid temperature, source function from DDSCAT, radius and length of the overall nanowire heterostructure, and thermal conductivity of either bismuth or germanium, respectively. The thermal diffusivity, α, is defined as $\kappa/(\rho C_p)$, where ρ and C_p are the density and heat capacity of the nanowire. The values used for these parameters and all others used in the calculation are presented in Table C.1. The DDSCAT simulations demonstrated almost no dependence of the source term on ϕ, and we neglect the ϕ-dependence of the Laplacian. In addition, there is very little variation of the source term radially and axially within the bismuth and germanium portions of the heterostructure. Thus, we employed volume-average sources for the bismuth nanocrystal (σ_{Bi}) and germanium nanowire (σ_{Ge}). Details of the DDSCAT calculation and temperature dependence are discussed below.

In addition to the modifications discussed in Chapter 4, we employed a temperature-dependent boundary condition via the heat transfer coefficient, h, to account for convective heat loss at the nanowire surface. We defined the heat transfer coefficient as follows

$$h = \frac{k}{L}\left(\frac{4}{3}\left(\frac{7RaPr}{5(20+21Pr)}\right)^{1/4} + \frac{4}{35}\left(\frac{(272+315Pr)L}{(64+63Pr)2r}\right)\right) \quad \text{(C.3)}$$

where L is nanowire length, r is the nanowire radius, h is the heat transfer coefficient, and k is the thermal conductivity of the medium.[377,467] Here, Ra, the Rayleigh number, is the product of the Grashof, Gr, and Prandtl, Pr, numbers,

$$Gr = \frac{g\beta\Delta TL^3}{\mu^2} \quad \text{and} \quad Pr = \frac{\mu\rho C_p}{k} \quad \text{(C.4)}$$

where g, β, ρ, and C_p are the acceleration due to gravity, the thermal expansion coefficient, density, and heat capacity of the medium evaluated at the film temperature, $\left(T_{surface,avg} + T_\infty\right)/2$. Here, ΔT is the temperature difference between the nanowire surface and the bulk solvent. The temperature-dependent properties of squalane are shown in Figure C.1.[468]

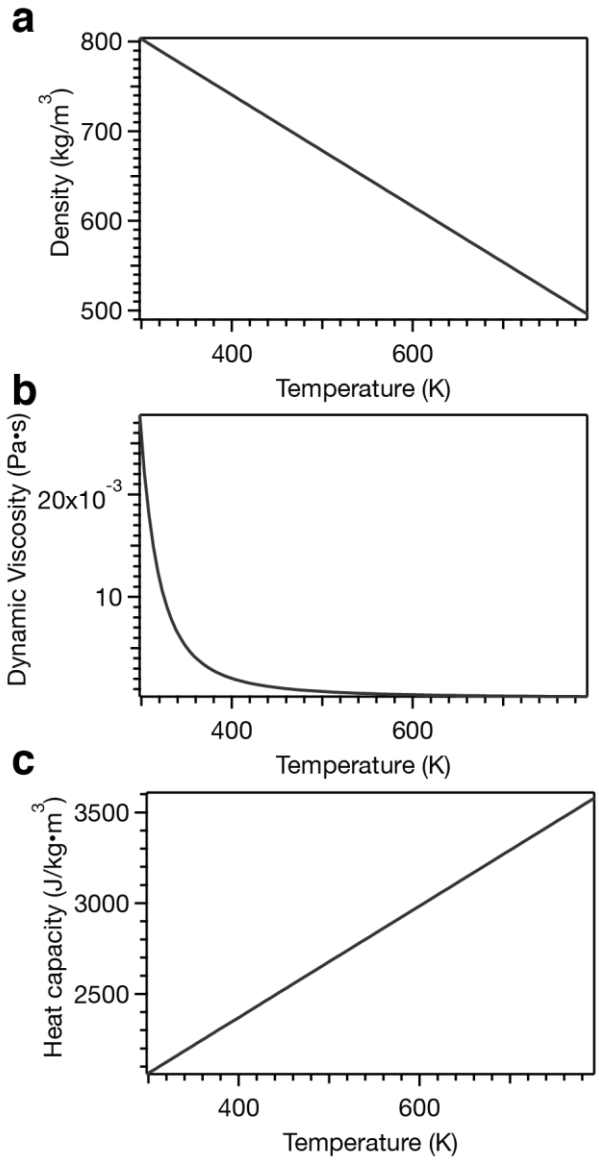

Figure C.1. Temperature-dependent properties of squalane used in the heat transfer calculation including the density (a), dynamic viscosity (b), and heat capacity (c). While none of the calculations exceeded this temperature range, the code bounded the values so that any iteration that produced temperatures above 793 K would default to the solvent properties at 793 K instead.

The radial boundary conditions were then implemented as

$$\left.\frac{\partial\theta}{\partial\xi}\right|_{\xi=0} = bounded \qquad \text{and} \qquad \left.\frac{\partial\theta}{\partial\xi}\right|_{\xi=1} = -Bi_R\theta|_{\xi=1} = -\frac{hR}{\kappa}\theta|_{\xi=1}. \tag{C.5}$$

The axial boundary conditions were then defined via Fourier's law for conduction to the bottom and top glass coverslips at T_∞ as

$$\left.\frac{\partial\theta}{\partial\xi}\right|_{\zeta=1} = -\frac{L_{chamber}\kappa_f}{\kappa_B}\theta|_{\zeta=1} \qquad \text{and} \qquad \left.\frac{\partial\theta}{\partial\xi}\right|_{\zeta=0} = \frac{L_{chamber}\kappa_f}{\kappa_G}\theta|_{\zeta=0} \tag{C.6}$$

where $L_{chamber}$ is half the height of the chamber (50 μm) and κ_f, κ_B, and κ_G are the thermal conductivities of squalane (0.15 $W{\cdot}m^{-1}K^{-1}$), the bismuth nanocrystal (3 $W{\cdot}m^{-1}K^{-1}$),[140] and the germanium nanowire (7 $W{\cdot}m^{-1}K^{-1}$), respectively.[469]

Using a classical product solution, we first solve the homogenous equation

$$\frac{\partial\theta}{\partial\tau} = \frac{1}{\xi}\frac{\partial}{\partial\xi}\left(\xi\frac{\partial\theta}{\partial\xi}\right) + a^2\frac{\partial^2\theta}{\partial\zeta^2} \tag{C.7}$$

by assuming a solution of the form

$$\theta(\tau,\xi,\zeta) = A_{m,n}(\tau)X_m(\xi)Z_n(\zeta). \tag{C.8}$$

The radial equation produces

$$X_m(\xi) = J_0(\mu_m\xi) \tag{C.9}$$

with eigenvalues satisfied by

$$\mu_m J_1(\mu_m) = Bi_R J_0(\mu_m) \tag{C.10}$$

where J_α is a Bessel function of order α. Similarly, the axial solution yields

$$Z_n(\zeta) = cos(\gamma_n\zeta) + \frac{Bi_0}{\gamma_n}sin(\gamma_n\zeta) \tag{C.11}$$

with eigenvalue equation

$$(\gamma_n^2 - Bi_0Bi_1)sin(\gamma_n) = (Bi_0 + \gamma_nBi_1)cos(\gamma_n). \tag{C.12}$$

The Biot number, Bi, is defined as the ratio of heat transport away from the nanostructure to the heat transport within an individual nanostructure. Here, the Biot numbers, are defined as

$$Bi_0 = \frac{hL}{\kappa_G} = \frac{L\kappa}{L_{chamber}\kappa_G}, \qquad Bi_1 = \frac{hL}{\kappa_B} = \frac{L\kappa}{L_{chamber}\kappa_B}, \qquad Bi_R = \frac{hR}{\kappa_R}, \tag{C.13}$$

where $L_{chamber}$ is the distance from the nanowire to the coverslip, 50 μm.

We combine these to define a product solution

$$\theta(\tau, \xi, \zeta) = \sum_m \sum_n A_{m,n}(\tau) X_m(\xi) Z_n(\zeta). \tag{C.14}$$

To solve for the coefficients $A_{m,n}(\tau)$, we substitute this solution into the full inhomogeneous equation (Eq. (C.1)) as

$$\sum_m \sum_n \left(\frac{\partial A_{m,n}(\tau)}{\partial \tau} + \gamma_n^2 A_{m,n}(\tau) \right) X_m(\xi) Z_n(\zeta) = \sigma. \tag{C.15}$$

Here, we've defined $\lambda_{m,n}^2 = \mu_m^2 + a^2\gamma_n^2$. Because Eq. (C.15) is a Sturm-Liouville equation, the solutions $X_m(\xi)$ and $Z_n(\zeta)$ are orthogonal. Thus, we can apply orthogonality as

$$\left(\frac{\partial A_{m,n}(\tau)}{\partial \tau} + \gamma_n^2 A_{m,n}(\tau) \right) \left|\left|X_m\right|\right|^2 \left|\left|Z_n\right|\right|^2 = \int_0^1 \int_0^1 \sigma \xi' X_m(\xi')\, Z_n(\zeta') d\xi' d\zeta'. \tag{C.16}$$

where ξ' and ζ' are dummy variables for integration and $\left|\left|X_m\right|\right|^2$ and $\left|\left|Z_n\right|\right|^2$ are normalization factors defined by

$$\left|\left|X_m\right|\right|^2 = \int_0^1 \xi' [J_0(\mu_m \xi')]^2 \, d\xi' \tag{C.17}$$

and

$$\left|\left|Z_n\right|\right|^2 = \int_0^1 [Z_n(\zeta')]^2 \, d\zeta'. \tag{C.18}$$

To solve for the coefficients $A_{m,n}(\tau)$, we then apply an integrating factor and take the limit as τ approaches infinity, yielding the solution

$$A_{m,n} = \frac{\left(1 - e^{-\lambda_{m,n}^2}\right)}{\lambda_{m,n}^2} \int_0^1 \int_0^1 \sigma \xi' \frac{X_m(\xi')}{\left||X_m|\right|^2} \frac{Z_n(\zeta')}{\left||Z_n|\right|^2} d\xi' d\zeta' \tag{C.19}$$

Due to its weak radial dependence, the source, σ, only varies axially. In addition, within the bismuth and germanium, it has very little axial dependence, and we can simplify the equation as

$$A_{m,n} = \frac{\left(1 - e^{-\lambda_{m,n}^2}\right)}{\lambda_{m,n}^2} \int_0^1 \xi' \frac{X_m(\xi')}{\left||X_m|\right|^2} d\xi' \left[\sigma_{Ge} \int_0^\beta \frac{Z_n(\zeta')}{\left||Z_n|\right|^2} d\zeta' + \sigma_{Bi} \int_\beta^1 \frac{Z_n(\zeta')}{\left||Z_n|\right|^2} d\zeta'\right] \tag{C.20}$$

where β is the nondimensional axial position of the bismuth-germanium interface. The temperature of the heterostructure can then be solved by Eq. (C.14).

DDSCAT Solution:

To calculate the source function, we used the discrete dipole approximation (DDA) implemented in DDSCAT. We created the cylinder-cylinder heterostructure in MATLAB, using ~87,000 dipoles. The discrete dipole approximation is valid for[470]

$$\left(\frac{3V}{4\pi}\right)^{1/3} < \frac{\lambda}{|m|}\left(\frac{N}{10^6}\right)^{1/3} \tag{C.21}$$

where V, N, and λ are the volume of the structure in μm^3, the number of dipoles, and the wavelength in μm, and m is the ratio of the refractive index of the nanomaterial to that of the solvent. For a cylinder-cylinder heterostructure with a diameter of 32 nm, an overall length of 1000 nm, and a bismuth cylinder tip with a length of 40 nm ($\beta = 0.96$). For the computationally complex case, assuming that the entire cylinder is bismuth with n_{Bi} = 4.33 – 3.88i and $n_{squalane}$ = 1.48, the use of 87,000 dipoles (19 dipoles across the diameter and 297 dipoles along the length of the wire) satisfies this inequality.

Temperature-Dependent Nanocrystal Characteristics:

Due to the high temperature of the bismuth seed and its low melting point, the bismuth nanocrystal at the end of the nanowire heats, melts, and alloys with the germanium during nanosoldering. To account for this effect, we allowed the composition of the nanocrystal to vary as a function of temperature according to the Bi-Ge binary phase diagram, as shown in Figure C.2.

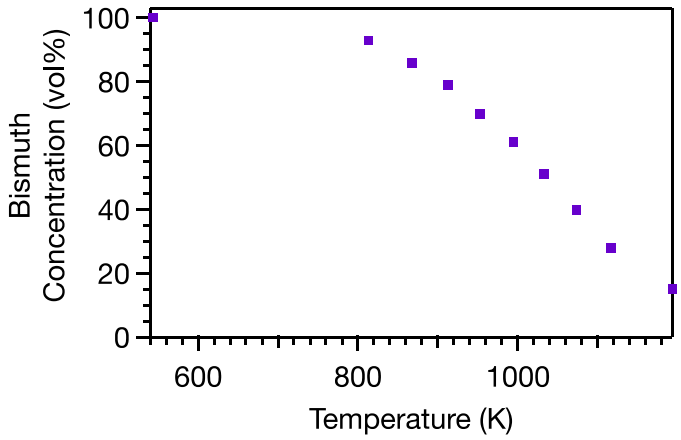

Figure C.2. Temperature-dependent bismuth concentration in the bismuth-germanium binary alloy system.[471]

This allows the composition of the molten tip to vary from 100% bismuth below 271°C to 15% bismuth at 920°C. To approximate the effect of alloying on the bismuth nanocrystal, we employed an effective medium approximation[472] using the atomic volumes of bismuth and germanium. This allows us to define a temperature-dependent complex refractive index (Figure C.3).

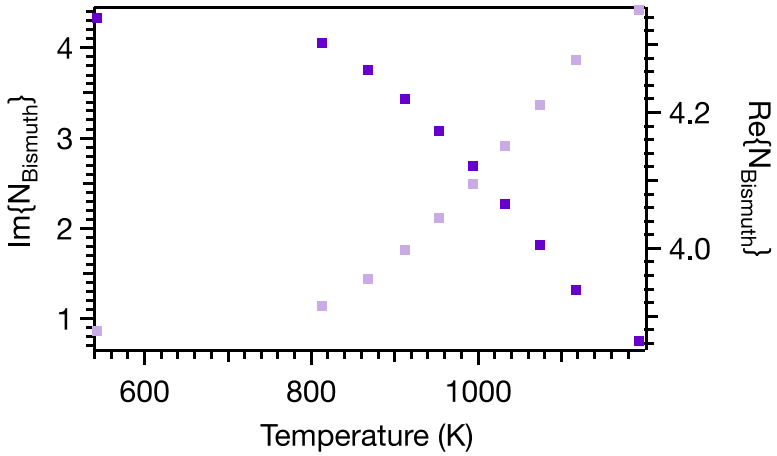

Figure C.3. Temperature dependence of the imaginary and real components of the bismuth alloy refractive index. To calculate these values, we used the volume-averaged refractive index of bismuth and germanium, weighted by the temperature-dependent concentrations in Figure C.2.

As the temperature of the bismuth tip increases, the concentration of germanium in the bismuth alloy increases, causing $\mathrm{Im}\{n_{Bi}\}$ to decrease and $\mathrm{Re}\{n_{Bi}\}$ to increase. Using DDSCAT, we calculated the internal electric field profile for the cylinder-cylinder heterostructure. To simulate the effects of melting and alloying, we used the refractive index values from Figure C.3. These normalized, volume-averaged results are presented in Figure C.4.

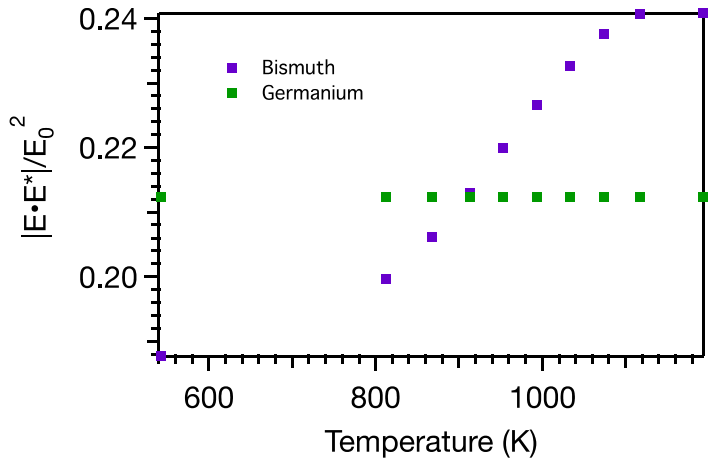

Figure C.4. The volume-averaged, normalized electric field in the germanium and bismuth portions of the nanowire heterostructure. These were calculated by using DDSCAT to evaluate the internal electric fields in the heterostructure. At each temperature, the bismuth alloy refractive index was set using Figure C.3, allowing it to vary as the composition of the metal alloy tip changes with temperature. Because the composition of the germanium section of the nanowire does not change significantly with temperature, we do not incorporate any temperature dependence.

We then convert these data into a source function, $\dot{Q}'''$, for the heat transfer equation (Equation 4.2), as shown in Figure C.5.

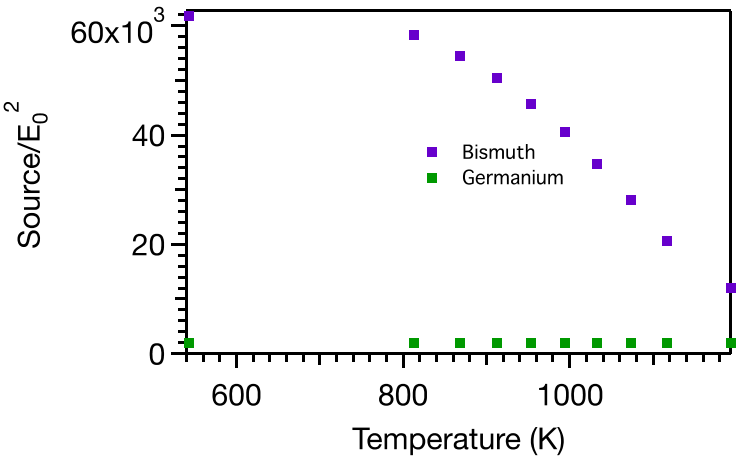

Figure C.5. The electric-field-normalized, temperature-dependent source function calculated from the volume-averaged internal fields in Figure C.4 and Equation 4.2 in Chapter 4.

As expected from Equation 4.2, the bismuth metal alloy source term decreases as its temperature rises and it incorporates additional germanium with a lower absorption coefficient. For example, the product of $Re\{n_{Bi}\}$ and $Im\{n_{Bi}\}$ decreases from 16.8 at 271°C to 3.26 at 920°C.

To incorporate these temperature-dependent effects, we calculated the average temperature of the heterostructure and then iterate until the converged to within 1% of the previous average temperature by allowing only temperature-dependent solvent properties to vary. Then, we calculated the average temperature of the bismuth nanocrystal tip, updated the new source function as described above, and then iterated with fixed solvent properties until the average temperature of the nanocrystal converged to within 1% of the average temperature of the previous iteration.

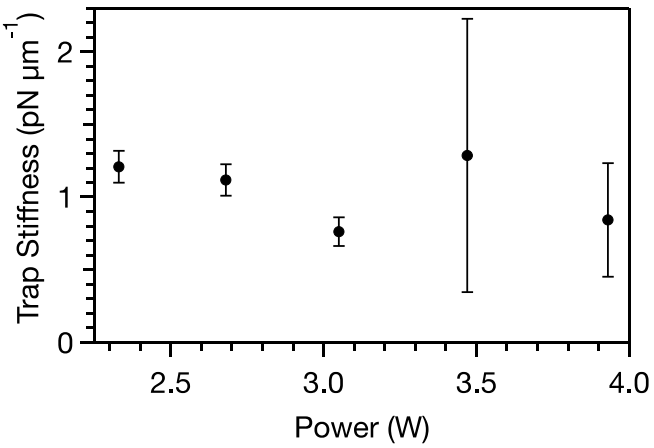

Figure C.6. The calculated trap stiffness as a function of power before beam expansion.[369,379] Note that this includes the temperature-dependent solvent properties shown in Figure C.1. The significant variation in viscosity with trapping power strongly influences the trap stiffness. Error bars indicate the standard deviation from three separate measurements.

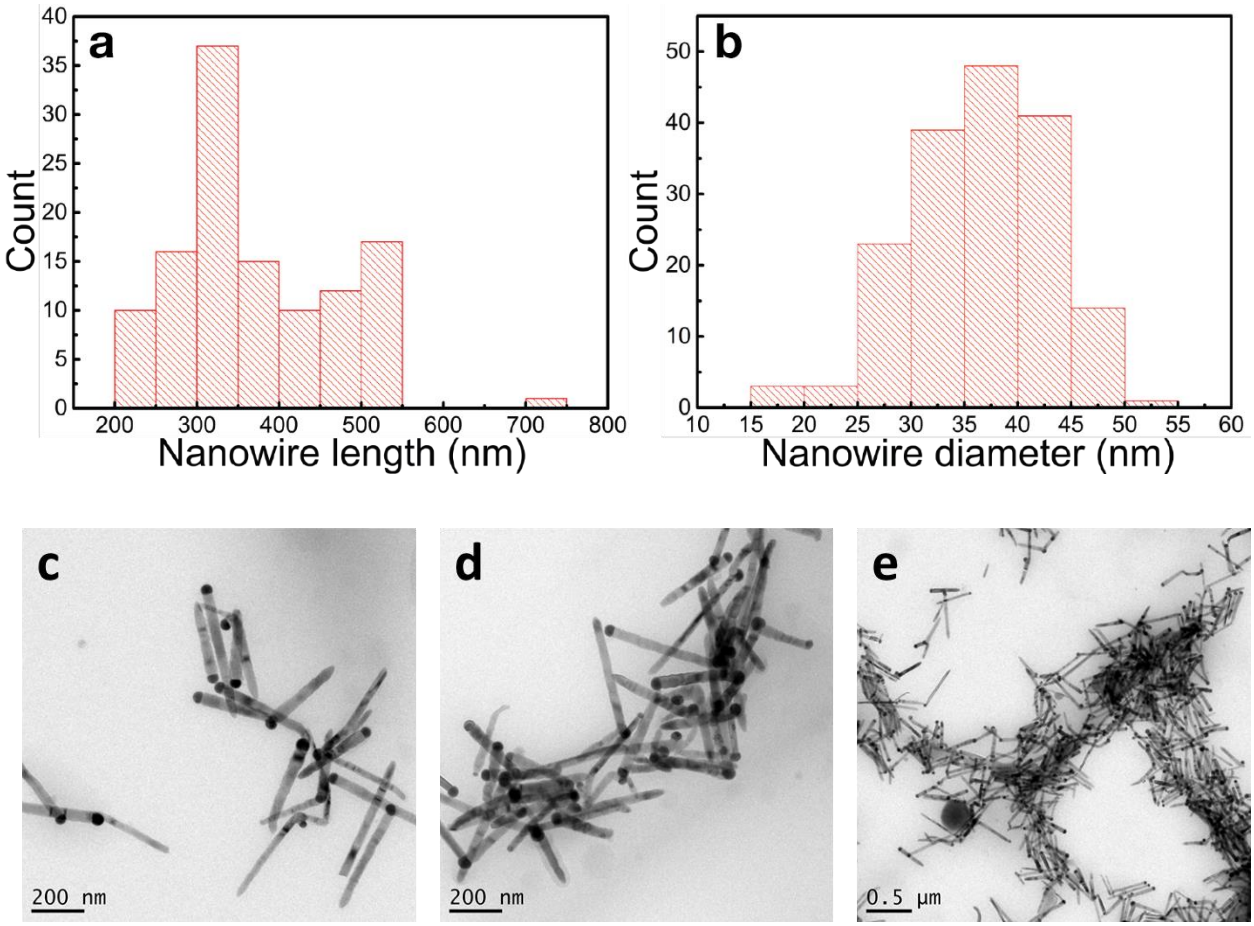

Figure C.7. Length and diameter distributions (a,b) for the bismuth-seeded germanium nanowires shown in Figure 4.1. Additional representative TEM images (c-e), illustrating the monodispersity of the nanowire building blocks. The nanowires were synthesized by a solution-liquid-solid growth that can be easily tuned to create a wide range of lengths and diameters.

Table C.1. Parameters used for heat transport calculations.[353,358,359,394]

Variable	Value	Units
T_∞	298	K
R	16	nm
L	1000	nm
β	0.96	-
κ_{Bi}	3	$W \cdot m^{-1}K^{-1}$
κ_{Ge}	7.5	$W \cdot m^{-1}K^{-1}$
α_{Bi}	$2.51 \cdot 10^{-5}$	m^2/s
α_{Ge}	$4.38 \cdot 10^{-6}$	m^2/s
$N_{Squalane}$	1.4818	
N_{Ge}	4.42 - 0.12i	-
N_{Bi}*	3.88 - 4.33i	-
μ_{perm}	$1.2566 \cdot 10^{-6}$	N/A^2
c	299790000	m/s
ε	$8.8542 \cdot 10^{-12}$	F/m
ϵ	1	-
λ	1020	nm
Bi_0	$3.73 \cdot 10^{-4}$	-
Bi_1	$9.33 \cdot 10^{-4}$	-
Bi_R *	$6.36 \cdot 10^{-3}$	-

* Initial values used for temperature-dependent parameters.

VITA

Elena Pearl Pandres was born in Roswell, Georgia, but shortly moved to Charlotte, North Carolina with her family in 1994. She graduated from South Mecklenburg High School in 2010 and went on to attend the University of Massachusetts at Amherst, where she was enrolled in the Commonwealth Honors College and graduated *cum laude* with a B.S. in Chemical Engineering in 2014. Upon graduation, she attended the University of Washington for her graduate studies in Chemical Engineering, where she became a Clean Energy Institute Fellow in 2015. Elena earned a Master of Science in Chemical Engineering in 2018 and earned her Ph.D. in Chemical Engineering while studying the synthesis, assembly, and integration of semiconductor nanowires under the supervision of Professor Vincent Holmberg.